TU Delft

Delft University of Technology

Numerical Analysis of Low-Prandtl Jets in Turbulent Forced Convection Regimes

Cascioli, E.

DOI
10.4233/uuid:a3931544-84fe-4fbd-a227-72ad21a3c402

Publication date
2024

Document Version
Final published version

Citation (APA)
Cascioli, E. (2024). *Numerical Analysis of Low-Prandtl Jets in Turbulent Forced Convection Regimes*. [Dissertation (TU Delft), Delft University of Technology]. https://doi.org/10.4233/uuid:a3931544-84fe-4fbd-a227-72ad21a3c402

Important note
To cite this publication, please use the final published version (if applicable).
Please check the document version above.

Copyright
Other than for strictly personal use, it is not permitted to download, forward or distribute the text or part of it, without the consent of the author(s) and/or copyright holder(s), unless the work is under an open content license such as Creative Commons.

Takedown policy
Please contact us and provide details if you believe this document breaches copyrights.
We will remove access to the work immediately and investigate your claim.

This work is downloaded from Delft University of Technology.
For technical reasons the number of authors shown on this cover page is limited to a maximum of 10.

Numerical analysis of low-Prandtl jets in turbulent forced convection regimes

Numerical analysis of low-Prandtl jets in turbulent forced convection regimes

Dissertation

for the purpose of obtaining the degree of doctor
at the Delft University of Technology,
by the authority of the Rector Magnificus Prof. Dr. Ir. T. H. J. J. van der Hagen,
chair of the Board of Doctorates,
to be defended publicly on
Thursday, 21st March 2024 at 10.00.

by

Edoardo CASCIOLI

Laurea Magistrale in Ingegneria Energetica,
La Sapienza University, Rome, Italy,
born in Rome, Italy.

This dissertation has been approved by the promotors.

Composition of the doctoral committee:

Rector Magnificus	chairperson
Prof. Dr. Dipl.-Ing. S. Kenjereš	Delft University of Technology, promotor
Prof. Dr. Ir. C. R. Kleijn	Delft University of Technology, promotor
Independent members:	
Prof. Dr. Ir. C. Vuik	Delft University of Technology
Prof. Dr. D. J. E. M. Roekaerts	Delft University of Technology
Prof. Dr. Ing. E. Stalio	University of Modena and Reggio Emilia (Italy)
Prof. Dr. Ing. N. Forgione	University of Pisa (Italy)
Other members:	
Ir. K. Van Tichelen	SCK CEN (Belgium)
Reserve members:	
Prof. Dr. Ir. B. J. Boersma	Delft University of Technology

This project was funded by SCK CEN and ENGIE, and supported by European Commission's H2020-EURATOM program under Grants 654935 (SESAME) and 662186 (MYRTE).

Keywords: Jets - Low-Prandtl Fluids - Forced Convection - Turbulent Heat Transfer

Printed by: Ridderprint

Front & Back: Contours of instantaneous temperature (front cover page) and velocity (back cover page) from the performed LES/DNS analysis on a non-isothermal triple-jet configuration in forced convection regime

Copyright © 2024 by E. Cascioli
ISBN 978-94-6366-829-3

An electronic version of this dissertation is available at
`https://repository.tudelft.nl`

Dedicated to Marina,
my beloved mom,
who inspired and encouraged me
in always striving for the best.

"Never say never, because limits, like fears, are often just an illusion".

cit. M. J. Jordan, 2009

Contents

Summary

The current need to ensure an effective and prompt transition of the energy sector towards zero-carbon has renewed the interest for nuclear technology. Small Modular Reactors (SMRs) seem particularly interesting for their reduced capital cost, operational flexibility and enhanced safety and security. Different SMR concepts are being developed around the world and the liquid metal-cooled technology is one of the most convincing design options. Liquid Metal Fast Reactor (LMFR) technology was identified as one of the possible Generation IV reactor options too.

In comparison with existing thermal reactors, the main advantages of LMFRs are the efficient use of nuclear fuel, possibility of partitioning and transmutation of long-lived fission products, inherent safety features and proliferation resistance, but also the enhanced heat transfer. The latter is directly linked to the high thermal conductivity of liquid metals, which, when expressed in dimensionless form, leads to these liquid metals having a very low ($\ll 1$) Prandtl number (Pr).

These low Pr numbers necessitate several adjustments in Computational Fluid Dynamics (CFD) tools and methods that are being used to predict fluid flow and thermal patterns in nuclear reactors. Most Turbulent Heat Transfer (THT) models have historically been optimized for fluids such as water and air, which have Pr numbers of the order of unity or higher. Dealing with low-Pr fluids, THT models cannot rely on commonly used approaches, such as the Reynolds analogy, since the similar behavior between the turbulent momentum and thermal fields is not observed anymore.

More advanced low-Pr THT models had already been proposed by 2015, when this doctoral research began. Among them, four-parameter models and algebraic heat flux models were often considered as the most promising options. It was clear, however, that further research was needed for their optimization towards reliable application in different flow configurations, and particularly in LMFR design.

Within this context, the present doctoral research aimed to firstly contribute to the further testing and development of low-Pr advanced THT models for industrial CFD applications. In mixing pool-type LMFR facilities, such as the Multipurpose hYbrid Research Reactor for High-tech Applications (MYRRHA) which is being designed at the Belgian Nuclear Center (SCK CEN) and which was the application focus of this doctoral thesis, wall-unconfined (free shear) forced convection (constant density) flows, particularly free jets, of liquid Lead-Bismuth Eutectic (LBE) play a fundamental role. Therefore, we selected low-Pr forced convection jet flows as the fundamental test case for our analysis.

In doing so, the very limited availability of relevant numerical and experimental databases that could be used to test and optimize the models was recognized. Therefore, our second aim was to contribute to the generation of high-fidelity databases for the low-Pr flow configurations of interest. We performed Reynolds Averaged Navier-Stokes (RANS) and Transient-RANS (T-RANS) simulations, Large-Eddy Simulations (LES) and combined LES-Direct Numerical Simulations (LES/DNS) on two different configurations.

The first studied jet flow configuration concerned the new MYRTE wind tunnel experimental campaign conducted at the von Karman Institute for Fluid Dynamics, which consisted of a single forced jet with heated co-flow with both air (Pr = 0.71) and He-Xe gas mixture (Pr = 0.2). We obtained a general good agreement between the generated numerical results and the experimental data. We also simulated lower Pr values, down to Pr = 0.025 and Pr = 0.006, corresponding to liquid LBE and sodium, respectively. The impact of a decreased Pr number was found to be increasingly important further away from the jet inlet, particularly when looking at temperature fluctuations. Reducing Pr had less impact on time-averaged temperatures, as expected due to the dominance of forced convection heat transfer.

The second studied jet flow configuration concerned the PLAJEST experiment, performed by the Japan Atomic Energy Agency in 2007. It consisted of a forced non-isothermal triple-jet of liquid sodium. Our numerical simulation results provided an overall good agreement with experiments. We were also able to identify dominant frequency peaks by using T-RANS simulations, though these simulations were not capable of capturing the thermal dissipation range.

Through our LES/DNS simulations, we contributed to the generation of high-fidelity databases that can be used to develop and optimize simpler CFD-THT models for low-Pr fluid forced jet flows. We tested simpler CFD-THT models from the four-parameter low-Pr THT model class in both RANS and T-RANS simulations. With these models, we observed some overprediction of the temperature fluctuations, particularly in the mixing region of the triple-jet test case.

It was concluded that, among the considered CFD techniques, wall-resolving dynamic LES/DNS simulations are recommended to get the most accurate prediction of temperature fluctuations, which play a crucial role in the correct estimation of fatigue effects on structural materials. For full-scale reactor simulation and design studies, wall-resolving dynamic LES/DNS is not feasible due to the high computational costs. Here, hybrid CFD techniques could be an interesting alternative to be studied as a follow-up for the present doctoral research.

The performed CFD analysis was carried out in the framework of the European Commission Horizon 2020 program within the SESAME and MYRTE projects, for which one deliverable was provided. The doctoral research was sponsored by SCK CEN and ENGIE.

Samenvatting

De noodzaak om een effectieve en snelle overgang van de energiesector naar koolstofvrije energie te verwezenlijken heeft geleid tot een hernieuwde belangstelling voor nucleaire technologie. Kleine modulaire reactoren (Small Modular Reactors, SMR's) lijken vooral interessant vanwege hun lagere kapitaalkosten, operationele flexibiliteit en verbeterde veiligheid en beveiliging. Over de hele wereld worden verschillende SMR-concepten ontwikkeld en de vloeibaar metaal gekoelde technologie is een van de meest veelbelovende opties. De Liquid Metal Fast Reactor (LMFR) technologie werd ook geïdentificeerd als één van de mogelijke Generatie IV reactoropties.

In vergelijking met bestaande thermische reactoren zijn de belangrijkste voordelen van LMFR's het efficiënte gebruik van splijtstof, de mogelijkheid van partitionering en transmutatie van langlevende splijtingsproducten, inherente veiligheidskenmerken en proliferatiebestendigheid, maar ook de verbeterde warmteoverdracht. Dit laatste is direct gekoppeld aan de hoge thermische geleidbaarheid van vloeibare metalen, die, uitgedrukt in dimensieloze vorm, ertoe leidt dat deze vloeibare metalen worden gekenmerkt door een zeer laag ($\ll 1$) Prandtl-getal (Pr).

Vanwege deze lage Pr-getallen zijn er verschillende aanpassingen nodig in Computational Fluid Dynamics (CFD) codes en -methoden die worden gebruikt om vloeistofstroming en thermische patronen in kernreactoren te voorspellen. Historisch zijn de meeste Turbulent Heat Transfer (THT) modellen geoptimaliseerd voor vloeistoffen zoals water en lucht, met Pr van de orde van 1 of hoger. Wanneer toegepast op vloeistoffen met lage Pr kunnen THT modellen niet gebaseerd worden op veelgebruikte benaderingen, zoals de Reynoldsanalogie, omdat het vergelijkbare gedrag tussen de turbulente impuls en de thermische velden niet meer wordt waargenomen. Meer geavanceerde THT-modellen voor lage Pr vloeistoffen waren al voorgesteld in 2015, toen dit promotieonderzoek begon. Hieronder werden modellen met vier parameters en algebraïsche warmtefluxmodellen vaak beschouwd als de meest veelbelovende opties. Het was echter duidelijk dat verder onderzoek nodig was voor hun optimalisatie naar betrouwbare toepassing in verschillende stromingsconfiguraties, en met name in LMFR-ontwerp.

In deze context was het huidige promotieonderzoek in de eerste plaats bedoeld om bij te dragen aan het verder testen en ontwikkelen van geavanceerde lage Pr THT-modellen voor industriële CFD-toepassingen. In mengpool-type LMFR-faciliteiten, zoals de multifunctionele hYbrid Research Reactor for High-tech Applications (MYRRHA) die wordt ontworpen in het Studiecentrum voor Kernenergie (SCK CEN) en die de toepassingsfocus was van dit promotieonderzoek, spelen niet-wandgebonden (vrije afschuiving) gedwongen convectie (constante dichtheid) stromingen, met name vrije jets, van vloeibaar loodbismut eutectisch (LBE) een fundamentele rol. Daarom hebben we low-Pr gedwongen jet stromingen geselecteerd als fundamentele testcase voor onze analyse.

Daarbij werden wij geconfronteerd met de zeer beperkte beschikbaarheid van relevante numerieke en experimentele databases die konden worden gebruikt om de model-

len te testen en te optimaliseren. Daarom was ons tweede doel om bij te dragen aan het genereren van betrouwbare databases voor turbulente stroming en warmteoverdracht in relevante lage-Pr stromingsconfiguraties. We deden Reynolds Averaged Navier-Stokes (RANS) en Transient-RANS (T-RANS) simulaties, Large-Eddy Simulaties (LES) en gecombineerde LES-Direct Numerical Simulaties (LES/DNS) voor twee verschillende configuraties.

De eerste bestudeerde stromingsconfiguratie betrof de nieuwe experimentele MYRTE-windtunnelcampagne uitgevoerd aan het von Karman Institute for Fluid Dynamics. Deze bestond uit een enkele gedwongen straal met verwarmde co-flow met zowel lucht (Pr = 0.71) als een He-Xe gasmengsel (Pr = 0.2). We verkregen een algemeen goede overeenkomst tussen de gegenereerde numerieke resultaten en de experimentele gegevens. We simuleerden ook lagere Pr-waarden, tot Pr = 0.025 en Pr = 0.006, overeenkomend met respectievelijk vloeibare LBE en natrium. De impact van een verlaagd Pr-getal bleek steeds belangrijker te worden verder weg van de straalinlaat, vooral als gekeken wordt naar temperatuurfluctuaties. Het verminderen van Pr had minder invloed op de tijdgemiddelde temperaturen, zoals verwacht vanwege de dominantie van convectieve warmteoverdracht.

De tweede bestudeerde stromingsconfiguratie betrof het PLAJEST-experiment, uitgevoerd door het Japanse Atoomenergieagentschap in 2007. Het bestond uit een geforceerde, niet-isothermische, drievoudige jet van vloeibaar natrium. Onze numerieke simulatieresultaten leverden over het algemeen een goede overeenkomst op met experimenten. We waren ook in staat om dominante frequentiepieken te identificeren met behulp van T-RANS-simulaties, hoewel deze simulaties niet in staat waren om de range van thermische dissipatie te bepalen.

Via onze LES/DNS-simulaties hebben we bijgedragen aan het genereren van betrouwbare databases die kunnen worden gebruikt om eenvoudiger CFD-THT-modellen voor geforceerde straalstromen van lage Pr vloeistoffen te ontwikkelen en te optimaliseren. We hebben eenvoudigere CFD-THT-modellen uit de vier parameter lage-Pr THT-modelklasse getest in zowel RANS- als T-RANS-simulaties. Bij deze modellen zagen we enige overschatting van de temperatuurschommelingen, met name in het menggebied van de triple-jet testcase.

Wij concluderen dat, van de bestudeerde CFD-technieken, wandopgeloste dynamische LES/DNS-simulaties zijn aan te bevelen om de meest nauwkeurige voorspelling van temperatuurfluctuaties te krijgen, die een cruciale rol spelen bij studies naar vermoeiingseffecten op structurele materialen. Voor reactorsimulaties en ontwerpstudies op volle schaal is wandoplossing van dynamische LES/DNS simulaties niet haalbaar vanwege de hoge rekenkosten. Hier zouden hybride CFD-technieken een interessant alternatief kunnen zijn om te bestuderen als vervolg op het huidige promotieonderzoek.

De uitgevoerde CFD-analyse werd uitgevoerd in het kader van het Horizon 2020-programma van de Europese Commissie binnen de SESAME- en MYRTE-projecten, waarvoor één deliverable werd verstrekt. Het promotieonderzoek werd gesponsord door SCK CEN en ENGIE.

1 Introduction

1.1 Application background

The Belgian Nuclear Research Centre (SCK CEN), is at the forefront of Heavy Liquid-Metal (HLM) nuclear technology worldwide with the development of the Multi-purpose hYbrid Research Reactor for High-tech Applications (MYRRHA), [1]. Within the MYRRHA project, SCK CEN is designing a flexible fast-spectrum irradiation facility, configured as an Accelerator-Driven System (ADS), able to operate in subcritical and critical mode. In addition to material testing and fuel research, the objectives of the facility are to prove the feasibility of the ADS technology for the transmutation of long-lived nuclear waste as well as to represent a demonstration plant for Generation IV heavy liquid metal-cooled reactors. In 2010, MYRRHA was on the high-priority list of the large infrastructures as established by the European Strategic Forum for Research Infrastructures, [2]. The system design (version 1.6) features a pool-type primary cooling system operating with Lead-Bismuth Eutectic (LBE). As shown in Fig. 1.1, a diaphragm inside the reactor vessel separates the hot from the cold plenum and supports the in-vessel fuel storage. In-vessel fuel handling machines transfer fuel assemblies from the core to the in-vessel fuel storage.

The core of MYRRHA, consisting of mixed-oxide fuel assemblies (108 in the critical core) of 127 wire-wrapped fuel pins with an active length of 600 mm, is located between the plena. Fifty-five positions in the core can be occupied by in-pile test sections or by control and safety rods (in the critical configuration). The central position can house the spallation target (in the subcritical configuration) or a fuel assembly or an in-pile test section (in the critical configuration). The primary, secondary, and tertiary cooling systems have been designed to evacuate a maximum power of 110 MW (thermal). The primary cooling system consists of two pumps and four heat exchangers. The secondary cooling system is a water/steam system at 16 bar. Given the innovative nature of MYRRHA, the project is currently going through a pre-licensing phase, [3]. SCK CEN will demonstrate the technical maturity of the design to start the licensing process through the submission to the Belgian Federal Agency for Nuclear Control of a Design Options and Provisions File

This chapter is partially based on the scientific publication:
K. Van Tichelen, G. Kennedy, F. Mirelli, A. Marino, A. Toti, D. Rozzia, ***E. Cascioli****, S. Keijers and P. Planquart, Advanced liquid-metal thermal-hydraulic research for MYRRHA, Nuclear Technology 206 (2020) 150-163.*

1

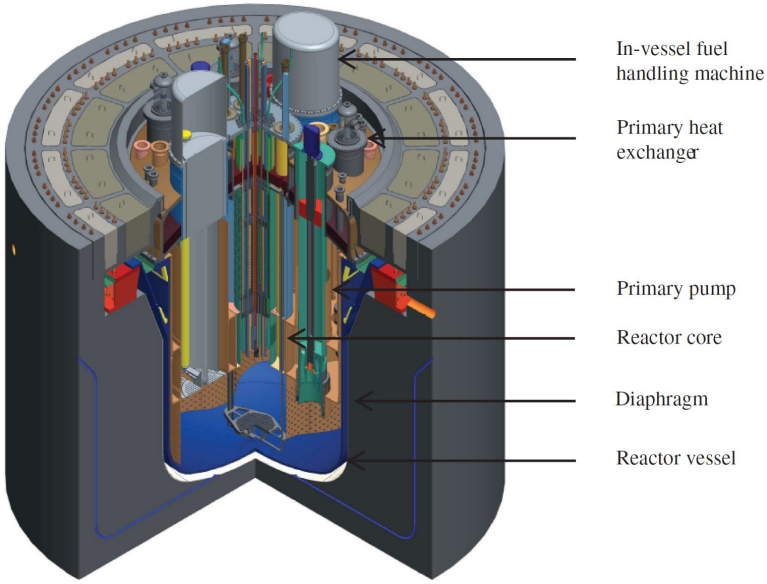

Figure 1.1: MYRRHA reactor vessel and internals.

describing the selected safety and security provisions implemented within the design, and so-called Focus Point Deliverables describing the status of and approach toward thematic issues that are specific for the HLM-cooled MYRRHA that are considered new or not mature enough and may have an impact on the safety of the facility. The MYRRHA Research and Development (R&D) program is driven by this pre-licensing process and aims to fill the existing gaps in knowledge with respect to LBE chemistry, material behavior, fuel behavior, instrumentation, and, of course, HLM thermal hydraulics. An ambitious program has been put in place and a large number of experimental facilities have been built over the past years for fundamental research and for performance tests and qualification of equipment in representative MYRRHA conditions, [4]. In this critical review we focus on important aspects of the R&D program for HLM thermal hydraulics.

1.1.1 MYRRHA R&D approach

Information on the thermal-hydraulic behavior of MYRRHA is requested by reactor designers and safety analysts to support the pre-licensing activities. The information needed ranges from understanding of basic phenomena to the qualification of complete reactor components. Moreover, the models and numerical tools used in the safety analyses are subject to a Validation and Verification (V&V) process. This V&V process is goal based rather than rule based. Safety analysts identify and prioritize V&V needs and list outstanding issues that should be addressed by R&D. Whereas in the first years of the project this process of identification and prioritization was mostly based on expert judgement, it is now progressively made more systematic (by using tools like the Phenomena Identification and Ranking Table and uncertainty quantification) and in consultation with the safety authorities. In the R&D program, basic phenomena are investigated in separate effect tests. The

thermal-hydraulic behavior of reactor components is characterized in component-level tests. System-level integral tests study the dynamics of the reactor system from the interaction of different components. A large number of experimental facilities, from small to very large scales with appropriate levels of instrumentation, is necessary to cover the complete R&D program for MYRRHA. In parallel, numerical models and tools are being developed and validated for design and safety analysis. Here as well, different scales of modeling can be identified, from one-dimensional System Thermal-Hydraulic tools (STHs) to high-fidelity Large Eddy Simulations (LESs) and Direct Numerical Simulations (DNSs) in Computational Fluid Dynamics (CFD), matching the requirements put forward by the end users.

1.1.2 International framework

The favorable characteristics of Lead(-bismuth)–cooled Fast Reactors (LFRs) and ADS with respect to safety and sustainability result in increasing international efforts in the design of these systems and in the development of HLM technology. MYRRHA contributes to and benefits from these activities. In Russia, interest in LFR development has always been strong and is currently focused on two critical reactor concepts: the LBE-cooled Svintsovo Vismutovyi Bystriy Reaktor (SVBR) and the lead-cooled Bystriy Reaktor Estestrennoy Bezopasnosti (BREST), [5] [6]. In 2011, the Chinese Academy of Sciences launched an engineering project to develop an ADS for nuclear waste transmutation. The China Lead-based Reactor (CLEAR) was selected as the reference reactor for ADS development, as well as for the technology development of the Generation IV lead-cooled fast reactors, [7]. In the United States, Westinghouse, after careful evaluation of several nuclear reactor technologies, selected the LFR as the Generation IV technology with the best potential for commercial deployment, [8]. In Europe, next to MYRRHA, the Advanced Lead Fast Reactor European Demonstrator (ALFRED) project has the objective to demonstrate the LFR technology at the host site of Mioveni, near Pitesti in southern Romania, [9]. In addition, SEALER is a small lead-cooled reactor under development by the Swedish company BlyKalla, with the aim to ensure reliable and safe production of power in remote areas without connection to the national power grid, [10]. To support the development of HLM technology, national, European, and international research programs are giving access to an extensive platform of HLM facilities and tools in Europe and the rest of the world. The International Atomic Energy Agency provides a database of experimental facilities in support of the development and deployment of liquid-metal-cooled fast neutron systems (LMFNS catalogue), [11]. The database includes 150 experimental facilities of which 72 are specifically in support of LFR. In Europe, a strong collaborative network has been built in the past 20 years through the mechanism of the Framework Programs of the European Commission (EC). Important projects focusing on HLM thermal hydraulics to be mentioned here are ASCHLIM, EUROTRANS, THINS, SEARCH, MAXSIMA, MYRTE and SESAME, [12], and the more recent PATRICA and PASCAL. In 2019, a textbook was published summarizing the thermal-hydraulic challenges in HLM-cooled reactors describing the state of the art and formulating the needs for development, [13].

1

1.1.3 E-SCAPE experimental facility

One of the major HLM thermal-hydraulic facilities at SCK CEN is the European SCAled Pool Experiment (E-SCAPE) facility. It is a thermal-hydraulic 1/6-scale model of the primary system of the MYRRHA reactor, with a 100-kW electrical core simulator cooled by LBE, as shown in Fig. 1.2, [14]. It provides experimental feedback to the designers on the forced and natural circulation flow patterns. Moreover, it provides experimental data to validate system numerical codes for their use with LBE. Scaled replicas of all main components of MYRRHA are placed in the main vessel in order to maintain a geometric similarity. The main vessel outer diameter of E-SCAPE is 1400 mm. The total LBE inventory is 2.5 m^3. The total LBE mass flow rate can amount to 120 kg/s; the temperature range is 200°C to 340°C. E-SCAPE is densely instrumented to allow for a good characterization of the thermalhydraulic phenomena in view of the validation of numerical thermal hydraulic CFD simulations - more than 300 thermocouples determine temperature distributions and identify possible stratification.

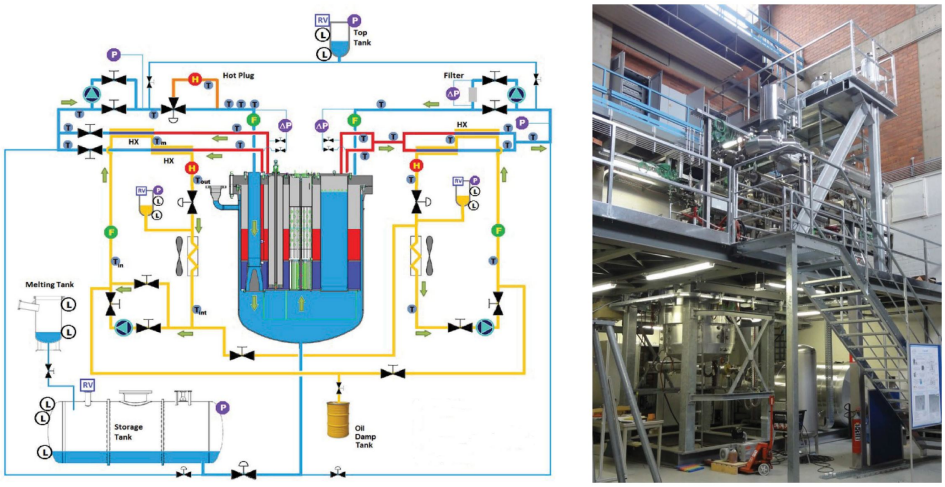

Figure 1.2: Schematic view (left) and picture (right) of the E-SCAPE facility.

1.2 Turbulent heat transfer in unconfined flow

Fig. 1.3 shows preliminary CFD simulations of the flow field in the MYRRHA and E-SCAPE facilities, [14]. Jet flows are recognized as fundamental flow regimes in such pool-type systems and are of major importance in the heat transfer and temperature distribution. In contrast, the largest part of CFD tools and methods have been optimized on wall-confined flows, such as pipe and channel flows. The first heat transfer study specifically applicable to liquid metals was performed in 1947 by Martinelli, [17]. From turbulent uniformly heated pipe flow experiments with mercury, it was recognized the thermal conduction dominates heat transfer in the turbulent core region of the pipe, [18]. The high thermal conductivity of low Prandtl (Pr) number liquid metals also leads to a thicker thermal boundary layer than the one which typically characterizes flows of higher Pr fluids like water

or air, [19]. In 1950s and 1960s, several experiments of turbulent pipe and duct flows with mercury and sodium-potassium eutectic in forced convection were performed. The purpose was to deeply investigate the low-Pr heat transfer phenomena and derive correlations for non-dimensional heat transfer and other thermal quantities.

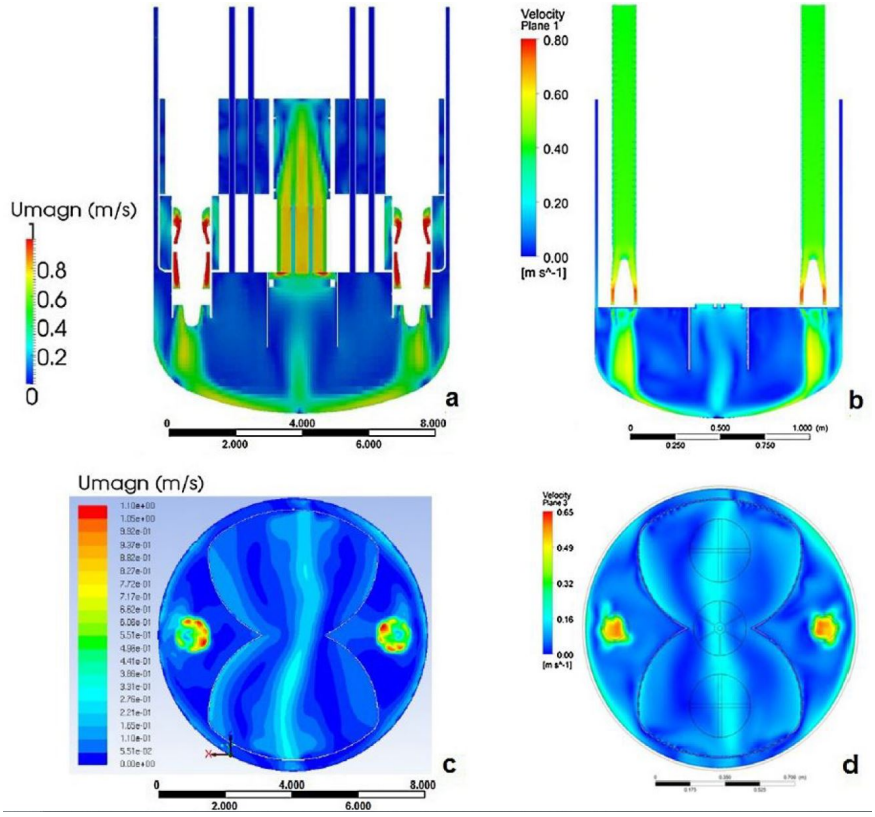

Figure 1.3: Velocity profile in the pump plane for MYRRHA (a) and E-SCAPE (b) and in a horizontal plane 0.3 m below the diaphragm for MYRRHA (c) and E-SCAPE (d).

Since the 1970s, CFD techniques have become a fundamental tool for thermal-hydraulic investigations in a wide variety of fields being currently integrated in the daily practice of researchers and designers, [15]. The recent and renewed attention for the next generation of nuclear liquid metal-cooled technology triggered again the interest in low-Pr heat transfer phenomena. Several DNS and LES studies on turbulent pipe and channel flows with low-Pr in forced convection have been performed, for example from the references [20] [21] [22] [23] [24] [25] [26]. On the other hand, concerning wall-unconfined flows of low-Pr fluids, some experimentally validated numerical reference simulations were performed for flows in a heated cavity and backward-facing step validated numerical reference studies on low-Pr were investigated, for example [27] [28] [29]. A more limited amount of validated DNS and LES data has been found about jet flows. An important experimental campaign on turbulent hot round jets in sodium (Pr = 0.006) with a cold co-flow was per-

1

formed by the end of 1990s in the test facility TEFLU at the Forschungszentrum Karlsruhe. Forced jet, buoyant jet and plume flow regimes were investigated with three different excess temperatures against the cold co-flow, [30] [31]. A combined LES/DNS simulation study was performed on the forced round jet flow correspondent to the TEFLU experiment too, [32]. Another relevant experimental campaign is represented by the PLAJEST experiment, which consisted of a non-isothermal triple jet with sodium performed by the Japanese Atomic Energy Agency (JAEA), [34]. Finally, and in parallel to present research project, a DNS study of a buoyant triple jet with low-Pr fluid (Pr = 0.031) has been performed and represents an important benchmark for the case of natural convection [33].

1.2.1 Modeling approaches

Concerning industrial CFD, the most frequently used Reynolds Averaged Navier-Stokes (RANS) and Transient-RANS (T-RANS) simulation approaches rely on the closure of Reynolds-averaged energy conservation equation by modeling the turbulent heat flux proportionally to the mean temperature gradients through eddy diffusivity. The latter is an anisotropic tensor but it is usually replaced by an isotropic scalar in most models. Furthermore, the Reynolds analogy is applied. This means that similarity is assumed between the turbulent transport features of momentum and heat: the isotropic eddy diffusivity is assumed to be proportional to the eddy viscosity. Hence, the turbulent Prandtl number (Pr_t), defined as the ratio between eddy viscosity and diffusivity, is set to a constant value, [35]. Fig. 1.4 shows the dependence of $1/Pr_t$ on flow parameters from DNS data on channel flows. The current best-practice guideline consists of setting Pr_t = 0.85 in the case of air, [19]. For the same type of flow configuration, similar performances in modeling low-Pr heat fluxes can be obtained by imposing Pr_t = 2.

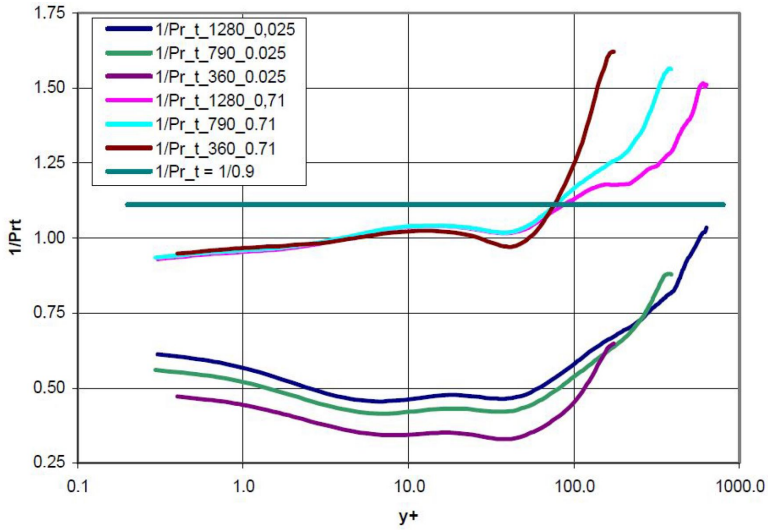

Figure 1.4: Profiles of the inverse of Pr_t from DNSs of turbulent channel flows at different friction Reynolds numbers (Re_τ = 360, 790, 1280) and Pr = 0.025 and 0.71 compared with the constant-value approach (Pr_t = 0.9), [19].

First improvements to the constant-value Pr_t approach consisted of correlations derived from the available experimental database, as aforementioned, on pipe and channel flows, [36] [37] [38]. Fig. 1.5 shows a comparison among three selected Pr_t correlations, and LES simulations. The "Kays" correlation is recognized to perform the best within the turbulent core of wall-confined turbulent flows, [39].

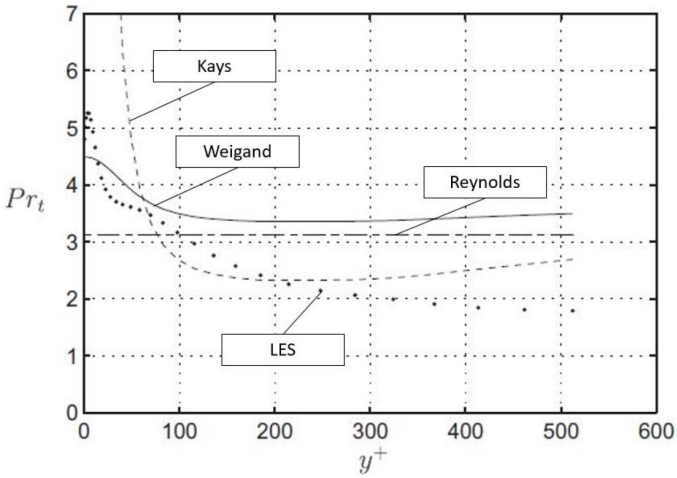

Figure 1.5: Comparison of Pr_t profiles from RANS simulations with Reynolds, Kays and Weigand correlations and LES for a turbulent channel flow at Re_τ = 590 and Pr = 0.01, [39].

High-Reynolds turbulence models are also normally used in industrial CFD, and require wall-functions for the treatment of near-wall region for both momentum and heat transfer. Standard wall functions are known to be inadequate for complex flows, especially for thermally active surfaces where the energy equilibrium is not present. This leads to an overestimation of the wall temperature. It can be solved by integrating discretized equations up to the wall using so-called low-Reynolds modification turbulence models. In this case, finer numerical meshes are required, [40]. Modified wall functions have been derived from experimental data, allowing to use high-Re turbulence models with advantages in terms of computational cost, [41]. Within this approach, a more advanced modeling approach for the low-Pr heat transfer consists of the two-equation ($k_\theta - \epsilon_\theta$) model. In this case, the low-Reynolds modification $k - \epsilon$ turbulence models are required for the Reynolds stresses modeling up to the wall. Turbulent heat fluxes are still proportional to mean temperature gradients by means of an eddy diffusivity. The latter is now modelled analogously to the eddy viscosity introducing the turbulent thermal energy (k_θ) and its dissipation rate (ϵ_θ). Hence, despite of two more differential transport equations have to be modelled and calibrated, the Pr_t concept can be kept with advantages in terms of implementation in CFD codes. Fig. 1.6 shows the good performances of the resulting four-parameter $k - \epsilon - k_\theta - \epsilon_\theta$ model with respect to DNS data of turbulent channel and pipe flows with low-Pr heat transfer, [42]. Further investigations have been performed to provide a comparative assessment with standard Pr_t models on more complex wall-confined

1

test cases too, [43].

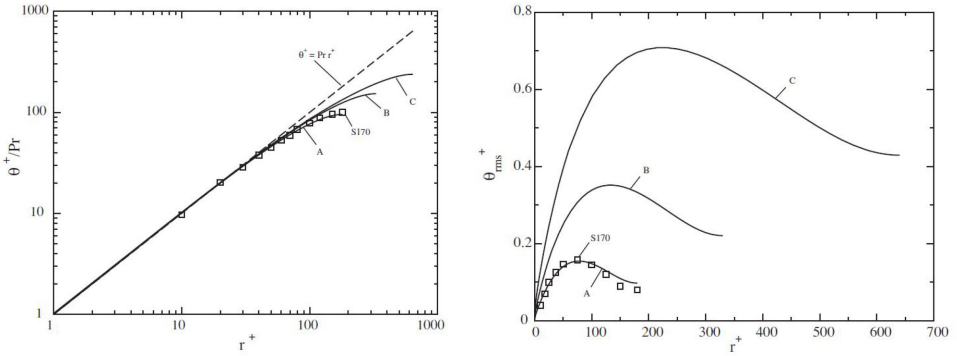

Figure 1.6: Universal temperature (left) and non-dimensional root-mean-square (rms) temperature fluctuations (right) profiles for Re_τ = 180 (A), 395 (B) and 640 (C), and comparison with DNS data for Re_τ = 170 (S170) of a turbulent pipe flow with heat transfer, [42].

Finally, second-order turbulent heat transfer models are the most interesting from an academic point of view, [19]. Early second-order models were proposed as alternative method for the Pr_t definition to keep the easiest implementations for RANS simulations, [44]. Then, this approach was applied as a stand-alone method for the closure of the Reynolds-averaged energy equations. Improvements have also concerned buoyant flows with separate transport equations not only for turbulent heat fluxes but also for temperature variance, [45] [46] [47]. In this case buoyancy effects need to be calculated with more accuracy, [19]. Since major interactions occur in the near-wall region in buoyancy-driven flows, the integration up to the wall is required. Hence, the low-Reynolds modification turbulence models are recommended to avoid the computation of a full stress and flux system of discretized differential equations, [46] [40]. On the basis of validated DNS database, successive coefficient calibrations have led to improved performances against first-order closure methods for both forced and mixed/natural convection regimes, as shown in Fig. 1.7, [48].

Algebraic heat flux models have recently been implemented in commercial CFD codes, such as FLUTAN and STAR-CCM+. In 2003, comparative assessment between the constant-Pr_t and second-order turbulent heat transfer modelling approaches was performed referring to the TEFLU experiments too. In both cases, a low-Re modification turbulence model was adopted. RANS simulation results showed that the eddy diffusivity approach would provide acceptable agreement with measurements when the heat fluxes are mainly governed by molecular diffusivity. Temperature fields from the second-order turbulent heat flux model better agreed with experimental data, [31].

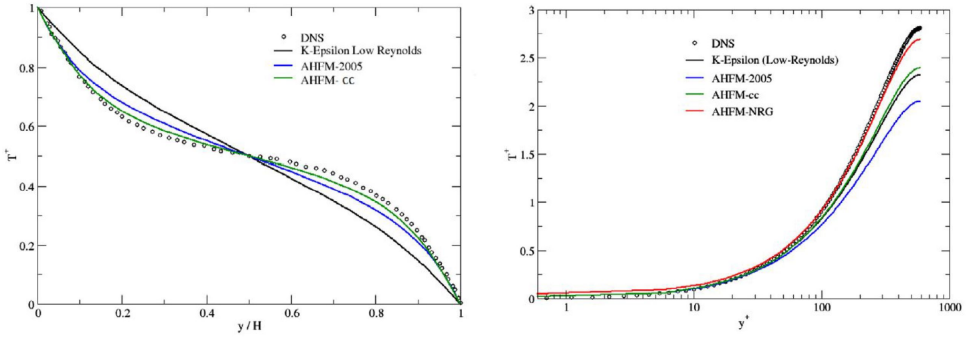

Figure 1.7: Universal temperature profiles from different low-Pr heat transfer models for Rayleigh-Bérnard convection with Rayleigh number of 100000 and Pr = 0.025 (left) and channel flow (right) with Re_τ = 590 and Pr = 0.01, [48].

1.3 Research objectives

We saw that industrial and commercial CFD tools normally rely on turbulent heat transfer models, which cannot reliably be used in the case of low-Pr turbulent flows. More advanced approaches have only been validated for wall-confined configurations, while they still need to be tested for wall-unconfined flows. Among these latter flows, we selected forced jets with low-Pr fluids as a fundamental test case, being representative for the operational conditions of pool-type nuclear facilities cooled by liquid metals. We also underlined that the improvement of the existing experimental and numerical database is a necessary requirement too. In this frame, the present research has been initiated, with the main objective of contributing to the development of a new robust turbulent heat transfer model for low-Pr wall-(un)confined configurations. The first objective is to define the fundamental flow configuration(s) for forced low-Pr jets, on which industrial and high-fidelity CFD simulations can be tested. In this phase, the novelty would mainly rely on the generation of numerical database, either on a new reference set-up or further detailing existing references in literature. Then, it could be possible to evaluate the state-of-the-art of the (selected) advanced low-Pr turbulent heat transfer models, e.g. performing sensitivity analyses with respect to the fluid thermal conductivity. Possible modifications might be proposed for such models, aiming to finally apply them to full-scale configurations, such as E-SCAPE. Overall, we aim to answer three main research questions:

1. **How can a new universal forced jet-flow configuration be developed to study turbulent heat transfer phenomena of both standard and low-Pr fluids?**

2. **What is the sensitivity of the forced convection turbulent heat transfer regime to increasing thermal conductivity (i.e. decreasing Prandtl number) of the fluid?**

3. **What is the recommended CFD approach for industrial applications on multiple forced jets with liquid metals?**

1

1.4 Outline

The CFD simulations were performed between 2015 and 2019, starting from simple pipe and channel flows, and evolving to multiple-jet configurations. The OpenFOAM CFD open-source code (version 2.4.x) was initially identified as suitable for the research, while the ChemE computational cluster of the Applied Sciences Faculty at Delft University of Technology was used to perform all the CFD simulations. We first addressed the lack of reference databases for jet flows, particularly when concerning the forced convection regime. Thanks to the collaboration with the von Karman Institute for Fluid Dynamics, in the frame of the European Commission HORIZON2020 projects SESAME and MYRTE, it was possible to perform RANS simulations and LES analysis on a new experimental set-up: a wind tunnel filled with a mixture of helium and xenon to experimentally investigate low-Pr heat transfer (Pr_{He-Xe} = 0.2), shown in Fig.1.8, [16]. This wind tunnel was a closed-loop sealed facility. The gas mixture was driven by an axial fan with a maximum velocity of 30 m/s in the test section. Experiments were performed in different wall-unconfined flow configurations, among which the forced single-jet with heated co-flow was the one of reference for the present research. Experimental data from Particle Image Velocimetry (PIV), hot-wire anemometry and micro-thermocouples were collected and provided in the second half of 2018. On this first test case, both LES/DNSs and RANS simulations were performed, additionally performing simulations for even lower Pr-values for the operating fluids, e.g. LBE (Pr = 0.025) and sodium (Pr = 0.006).

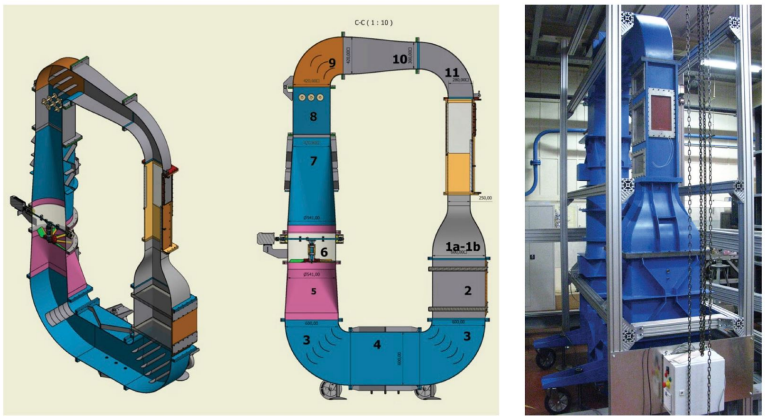

Figure 1.8: Schematic and picture of the MYRTE wind tunnel.

The second test case consisted of the PLAJEST experiment performed by JAEA in 2007, [34]. As mentioned, it was a forced triple-jet (hot-cold-hot) configuration with sodium (Pr = 0.006) and it has been selected as multi-jet configuration for the present research because of the lack of exhaustive numerical studies in literature, except for (poorly accessible) detailed internal reports from JAEA. Here, the first goal consisted of generating a new numerical database through (well refined) LES/DNS, characterized by a complete set of turbulence and heat transfer parameters from a wider range of streamwise locations. Then, a preliminary comparison with T-RANS simulations was performed, to estimate the

performance of low-Pr four-parameter turbulent heat transfer modelling and highlighting the key-factors to be improved. The performed CFD simulations have been presented in three (drafted, published or accepted) scientific papers, between 2020 and 2023, on which the following three chapters are fully based:

- in Chapter 2, we present a preliminary comparison between RANS simulations and experimental results on the single jet configuration of the MYRTE wind tunnel, only considering the experimental fluids, i.e. air (Pr = 0.71) and He-Xe (Pr = 0.2);
- in Chapter 3, we further investigate the same single jet flow configuration by performing dynamic LES and combined LES/DNS simulations, also simulating lower Pr numbers, i.e. liquid LBE (Pr = 0.025) and sodium (Pr 0.006);
- in Chapter 4, we cover the more complex triple-jet flow configuration with liquid sodium (Pr = 0.006) of the PLAJEST experiment, which is studied by performing combined LES/DNS and T-RANS simulations.

References

[1] H. Ait Abderrahim and K. Nakajima, Nuclear back-end and transmutation technology for waste disposal, Springer Nature - 2015.

[2] European Commission website (accessed Mar. 26, 2019): http://ec.europa.eu/research/infrastructures.

[3] G. Rubio Antón and G. Scheveneels, The MYRRHA reactor: approach to nuclear safety, Proc. IAEA Technical Mtg. Challenges in the Application of the Design Safety Requirements for Nuclear Power Plants to Small and Medium Sized Reactors, Vienna, Austria, September 4–8, 2017, International Atomic Energy Agency (2017).

[4] A. Aerts et al., R&D on heavy liquid metal technology in support of MYRRHA: state of the art, Proc. 14th Information Exchange Mtg. Actinide and Fission Product Partitioning and Transmutation, San Diego, California, October 17–20, 2016, Organisation for Economic Co-operation and Development, Nuclear Energy Agency (2016).

[5] V. V. Petrochenko, S. A. Grigoriev, O. G. Komlev, A. V. Kondaurov and G. I. Toshinsky, SVBR project: status and possible development, Proc. Int. Conf. Fast Reactors and Related Fuel Cycles, Yekaterinburg, Russian Federation, June 26–29, 2017, International Atomic Energy Agency (2017).

[6] Y. G. Dragunv et al., BREST-OD-300 reactor facility: development stages and justification, Transactions of the American Nuclear Society, Washington, D.C., October 29–November 2, 2017, Vol. 117, American Nuclear Society (2017).

[7] Y. Wu, Design and R&D progress of China lead-based reactor for ADS research facility, Engineering 2 (1) (2016) 124-131.

[8] P. Ferroni et al., Westinghouse's lead fast reactor program, Proc. Transactions of the American Nuclear Society, Washington, D.C., October 29–November 2, 2017, Vol. 117, American Nuclear Society (2017).

[9] M. Frignani et al., FALCON Advancements Towards the Implementation of the ALFRED Project, Proc. Int. Conf. Fast Reactors and Related Fuel Cycles, Yekaterinburg, Russian Federation, June 26–29, 2017, International Atomic Energy Agency (2017).

[10] J. Wallenius, S. Qvist, I. Mickus, S. Bortot, P. Szakalos and J. Ejenstam, Design of SEALER, a Very Small Lead-Cooled Reactor for Commercial Power Production in Off-Grid Applications, Nuclear Engineering and Design 338 (2018) 23-33.

[11] International Atomic Energy Agency website (accessed Apr. 30, 2019): https://nucleaus.iaea.org/sites.

[12] European Commission website (accessed Apr. 30, 2019): http://cordis.europa.eu.

[13] F. Roelofs, Thermal Hydraulics Aspects of Liquid Metal Cooled Nuclear Reactors, Woodhead Publishing - 2019.

[14] K. Van Tichelen, F. Mirelli, M. Greco and G. Viviani, E-SCAPE: a scale facility for liquid-metal, pool-type reactor thermal hydraulic investigations, Nuclear Engineering and Design 290 (2015) 65-77.

[15] F. Roelofs, A. Shams, I. Otic, M. Böttcher, M. Duponcheel, Y. Bartosiewicz, D. Lakehal, E. Baglietto, S. Lardeau and X. Cheng, Status and perspective of turbulence heat transfer modelling for the industrial application of liquid metal flows, Nuclear Engineering and Design 290 (2015) 99-106.

[16] P. H. Planquart et al., Description of a New Wind Tunnel to Study Heat Transfer Phenomena in a Gas Mixture at Low Prandtl Number, Proc. Int. Heat Transfer Conf., Beijing, China, August 10–15, 2018, IHTC (2018).

[17] R. C. Martinelli, Heat transfer to molten metals. Transactions of the American Society of Mechanical Engineers 69(8) (1947) 947-959.

[18] H. O. Buhr, A. D. Carr and R. E. Balzhiser, Temperature profiles in liquid metals and the effect of superimposed free convection in turbulent flow, International Journal of Heat and Mass Transfer, 11(4) (1968) 641-654.

[19] G. Grötzbach, Challenges in simulation and modeling of heat transfer in low Prandtl number fluids, Proc. 14th International Topical Meeting on Nuclear Reactor Thermal Hydraulics (NURETH-14), Toronto, Canada, September 25-30, 2011, American Nuclear Society (2011).

[20] H. Kawamura, K. Ohsaka, H. Abe and K. Yamamoto, DNS of turbulent heat transfer in channel flow with low to medium-high Prandtl number fluid; International Journal of Heat and Fluid Flow 19 (1998) 482-491.

[21] H. Kawamura, H. Abe and Y. Matsuo, DNS of turbulent heat transfer in channel flow with respect to Reynolds and Prandtl number effects, International Journal of Heat and Fluid Flow 20 (1999) 196-207.

[22] H. Abe, H. Kawamura and Y. Matsuo, Surface heat-flux fluctuations in a turbulent channel flow up to Re_τ = 1020 with Pr = 0.025 and 0.71, International Journal of Heat and Fluid Flow 25(3) (2004) 404-419.

[23] L. Redjem-Saad, M. Ould-Rouiss and G. Lauriat, Direct numerical simulation of turbulent heat transfer in pipe flows: Effect of Prandtl number, International Journal of Heat and Fluid Flow 28 (2007) 847-861.

[24] S. Saha, C. Chin, H. M. Blackburn and A. S. H. Ooi, The influence of pipe length on thermal statistics computed from DNS of turbulent heat transfer, International Journal of Heat and Fluid Flow 32 (2011) 1083-1097.

[25] L. Bricteux, M. Duponcheel, G. Winckelmans, I. Tiselj, I. and Y. Bartosiewicz, Direct and large eddy simulation of turbulent heat transfer at very low Prandtl number: Application to lead-bismuth flows, Nuclear Engineering and Design 246 (2012) 91-97.

[26] I. Tiselj, Tracking of large-scale structures in turbulent channel with direct numerical simulation of low Prandtl number passive scalar, Physics of Fluids 26 (2014) 1-17.

[27] G. Grötzbach and M. Wörner, Direct numerical and large eddy simulations in nuclear applications, International Journal of Heat and Fluid Flow 20 (1999) 222-240.

[28] I. A. Ermolaev, A. I. Zhbanov, V. S. Koshelev and S. V. Otpushchennikov, Investigation of the effect of the Prandtl number on the local properties of low-intensity convection in a rectangular region heated from below, High Temperature 49(4) (2011) 571-575.

[29] M. Niemann and J. Fröhlich, Buoyancy-affected backward-facing step flow with heat transfer at low Prandtl number, International Journal of Heat and Mass Transfer 101 (2016) 1237-1250.

[30] U. Knebel, L. Krebs, U. Müller and B. P. Axcell, Experimental investigation of a confined heated sodium jet in a co-flow, Journal of Fluid Mechanics 368 (1998) 51-79.

[31] L. Carteciano and G. Grötzbach, Validation of turbulence models in the computer code FLUTAN for a free hot sodium jet in different buoyancy flow regimes, Wissenschaftliche Berichte FZKA 6600 (2003) 1-34.

[32] I. Otić and G. Class, Numerical investigation of a heated sodium jet in a co-flow, Proc. of the ASME/JSME 2007 5th Joint Fluids Engineering Conference, San Diego, California, USA, July 30–August 2, 2007, ASME (2009).

[33] A. Fregni, D. Angeli, A. Cimarelli and E. Stalio, Direct numerical simulation of a buoyant triple jet at low-Prandtl number, International Journal of Heat and Mass Transfer 143 (2019) 118466.

[34] N. Kimura, H. Miyakoshi and H. Kamide, Experimental investigation on transfer characteristics of temperature fluctuation from liquid sodium to wall in parallel triple-jet, International Journal of Heat and Mass Transfer 50 (2007) 2024–2036.

[35] S. B. Pope, Turbulent Flows, Cambridge University - Cambridge Univ. Press 2000.

[36] A. M. Reynolds, The prediction of turbulent Prandtl and Schmidt numbers, International Journal of Heat and Mass Transfer 18 (1975) 1055-1069.

[37] W. M. Kays, Turbulent Prandtl number - Where are we? Journal of Heat Transfer 116 (1994) 284-295.

[38] B. Weigand, J. R. Ferguson and M. E. Crawford, An extended Kays and Crawford turbulent Prandtl number model, International Journal of Heat and Mass Transfer 40(17) (1997) 4191-4196.

[39] M. Duponcheel, L. Bricteux, M. Manconi, G. Winckelmans and Y. Bartosiewicz, Assessment of RANS and improved near-wall modeling for forced convection at low Prandtl numbers based on LES up to Re_τ = 2000, International Journal of Heat and Mass Transfer 75 (2014) 470-482.

[40] S. Kenjereš, S. B. Gunarjo and K. Hanjalić, Contribution to elliptic relaxation modelling of turbulent natural and mixed convection, International Journal of Heat and Fluid Flow 26 (2005) 569-586.

[41] B. A. Kader, Temperature and concentration profiles in fully turbulent boundary-layers, International Journal of Heat and Mass Transfer 24(9) (1981) 1541-1544.

[42] S. Manservisi and F. Menghini, A CFD four parameter heat transfer turbulence model for engineering applications in heavy liquid metals, International Journal of Heat and Mass Transfer 69 (2014) 312-326.

[43] S. Manservisi and F. Menghini, CFD simulations in heavy liquid metal flows for square lattice bare rod bundle geometries with a four parameter heat transfer turbulence model, Nuclear Engineering and Design 295 (2015) 251-260.

[44] M. Jischa and H. B. Rieke, About the prediction of turbulent Prandtl and Schmidt numbers from modeled transport equations, International Journal of Heat and Mass Transfer 22 (1979) 1547-1555.

[45] N. Shikazono and N. Kasagi, Second-moment closure for turbulent scalar transport at various Prandtl numbers, International Journal of Heat and Mass Transfer 39(14) (1996) 2977-2987.

[46] H. S. Dol, K. Hanjalič and S. Kenjereš, A comparative assessment of the second-moment differential and algebraic models in turbulent natural convection, International Journal of Heat and Fluid Flow 18 (1997) 4-14.

[47] I. Otić, G. Grötzbach and M. Wörner, Analysis and modelling of the temperature variance equation in turbulent natural convection for low-Prandtl-number fluids, Journal of Fluid Mechanics 525 (2005) 237-261.

[48] A. Shams, F. Roelofs, E. Baglietto, S. Lardeau and S. Kenjereš, Assessment and calibration of an algebraic turbulent heat flux model for low-Prandtl fluids, International Journal of Heat and Mass Transfer 79 (2014) 589-601.

2

Numerical and experimental analysis of a planar jet with heated co-flow at medium and low Prandtl-number values

In the present work, we combine experiments and numerical simulations of a planar jet with heated co-flow with medium (air) and low-Prandtl (He-Xe gas mixture) fluids. Jets are recognized as representative test cases to be investigated in large components of pool-type liquid metal-cooled nuclear systems, like the Multi-purpose hYbrid Research Reactor for High-tech Applications (MYRRHA), currently under design at SCK CEN. The present planar jet configuration mimics a closed wind tunnel that is designed and operated at VKI to generate an experimental database for velocity and temperature fields of a turbulent forced-convection flow regime. The performed experiments combine the Particle Imaging Velocimetry (PIV) (in characteristic planes) and thermocouple (single point) measurements. In parallel with experiments, comprehensive numerical simulations have been performed within the RANS modeling framework. Next to the standard eddy viscosity-based two-equation $k-\varepsilon$ model, an extended variant based on the low-Reynolds elliptic relaxation concept (so-called $\zeta-f$ model) has been applied too. To investigate the low-Prandtl effects on the heat transfer, series of the turbulent heat transfer models have been applied, ranging from a conventional constant turbulent Prandtl number to a more elaborate $k_\theta-\varepsilon_\theta$ model. The combination of the low-Reynolds $\zeta-f$ and $k_\theta-\varepsilon_\theta$ models was explored for the first time in the content of nuclear engineering applications. The focus of the numerical studies is to address in details the effects of low-Prandtl fluid in the strongly forced convection flow (central planar cold jet) in presence of a strong shear (hot co-flow). We demonstrate the importance of the proper specification of the in-

This chapter is fully based on the scientific publication:
***E. Cascioli**, S. Buckingham, S. Keijers, K. Van Tichelen and S. Kenjereš, Numerical and experimental analysis of a planar jet with heated co-flow at medium and low Prandtl-number values, Nuclear Engineering and Design 361 (2020) 1–11 .*

let boundary conditions in numerical simulations to properly mimic experimentally observed asymmetrical distributions of the cross-wise profiles of stream-wise velocity, turbulent kinetic energy and temperature. Finally, the minor differences in results between the assumed constant turbulent Prandtl number and more advanced $k_\theta - \varepsilon_\theta$ model of the turbulent heat flux confirmed the overly dominant mechanisms of the strong convection and molecular diffusion in the present configuration.

2.1 Introduction

The Multi-purpose hYbrid Research Reactor for High-tech Applications (MYRRHA) is a flexible fast-spectrum research reactor under design at the Belgian Nuclear Research Center (SCK CEN). MYRRHA is a pool-type reactor cooled by the liquid metal Lead-Bismuth Eutectic (LBE) and contributes to the demonstration of transmutation of long-lived radioactive waste. It also represents a prototype of the next generation of the fast reactor technology cooled by liquid metals, [1]. The high safety standards require a good understanding of heat transfer phenomena in liquid metals. Experiments are necessary to understand the mass, momentum, and heat transfer physics and validate the engineering models used in Computational Fluid Dynamics (CFD) codes, supporting the design and safety analyses of such advanced nuclear systems, [2]. Industrial CFD analyses are commonly based on Reynolds Averaged Navier-Stokes (RANS) simulations, where the Reynolds analogy is the standard approach in representing the turbulent heat transfer. This implies modeling turbulent heat fluxes analogously to Reynolds stresses in the time-averaged transport equations. This is acceptable and provides prediction of temperature fields in case of fluids with a molecular Prandtl number (Pr) of about the unity. Since liquid metals are characterized by significantly lower Pr values, as a consequence of their high thermal conductivity, the previous analogy is not applicable and more advanced Turbulent Heat Transfer (THT) models can be required, [3] [4]. Considering the pool-type configuration of the MYRRHA reactor, typical flow patterns in large components (i.e. upper and lower plena) are characterized by multi-jet interactions. Hence, the jet flow was selected as a fundamental test case to be investigated. The current amount of reference data for wall-unconfined flows is still limited. In the open literature, only two relevant experiments are TEFLU and PLAJEST, in which single- and triple-jet liquid metal flows were investigated, respectively, [5] [6]. Related Direct Numerical (DNS) and Large-Eddy Simulations (LES) only counts a few examples too, [7] [8]. Despite of the recent numerical studies on predicting momentum and passive scalar fields in forced jet flows ([9] [10] [11]), specific low-Pr fluid applications are still missing both experimentally and numerically.
In the present work, we compare the recently performed experiments (conducted at the von Karman Institute for Fluid Dynamics (VKI) within the MYRTE program funded by the European Commission) on a forced planar jet with heated co-flow with air (Pr=0.71) and He-Xe gas mixture (Pr=0.2), with RANS-based numerical simulations (performed at SCK CEN and Delft University of Technology). The aim is to compare standard Reynolds analogy-based approaches (i.e. [12] [13]) and a more advanced low-Pr two-equation THT model, which was previously presented and solely validated with reference to the wall-confined flows (i.e. [14][15] [16]).

2.2 Experimental setup

The MYRTE wind tunnel was designed and operated at VKI to experimentally investigate a forced planar jet with heated co-flow and other fundamental test cases (i.e. backward-facing step). Air and He-Xe gas mixture were considered as working fluids with Pr=0.71 and 0.2, respectively. Although the lowest Pr value is approximately one order of magnitude higher than the liquid metal range (i.e. LBE, Pr=0.025), previous DNS studies on pipe flow at Pr=0.2 demonstrated a sufficient impact on THT phenomena against air [17]. Moreover, a liquid metal experiment would have involved large difficulties in performing measurements of the turbulent quantities due to the opacity and high temperature of the fluid. A sketch of the experimental wind tunnel with a characteristic test section and Particle Image Velocimetry (PIV) set-up is shown in Fig. 2.1.

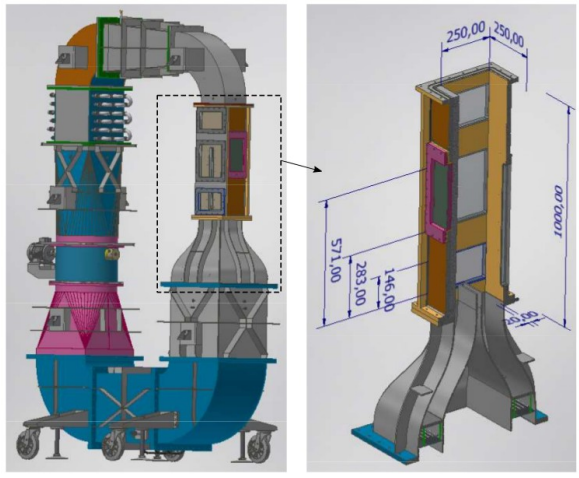

(a)

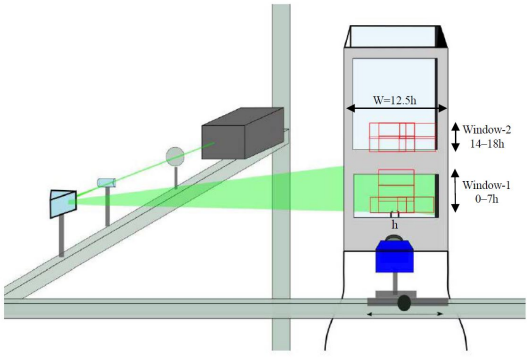

(b)

Figure 2.1: Sketch of the MYRTE wind tunnel (a) and PIV experimental set-up (b).

Entering the jet convergent region, the co-flow was heated-up by two electrical resistances placed at either side of the planar jet. The resulting temperature difference between the co-flow and jet-flow was kept at $\Delta T = T_{CO} - T_J = 12$ K throughout the measurements. These temperatures were monitored by two fixed thermocouples at the end of both jet and co-flow entrainment regions. A third movable thermocouple, coupled to a hot-wire probe for velocity measurements, performed acquisition further downstream. Two porous plates upstream of the heaters were dimensioned to achieve a co-flow to jet velocity ratio of about $U_{CO}/U_J = 0.17$. Geometrical specifications of interest for the following numerical analyses are the jet-nozzle height of $h = 0.021$ m and global width of the test section of $W = 12.5h$. Mean velocities at the inlet were $U_J = 16.01$ m/s and $U_{CO} = 2.67$ m/s. On the basis of the velocity difference between jet and co-flow, jet-nozzle height and kinematic viscosity of air at standard conditions, the Reynolds number of the jet was about 18000, confirming the forced convection regime. Further information on the MYRTE experiment, including the assessment of uncertainties for the performed PIV, hot-wire anemometry and thermocouple measurements can be found in reference [18]. In the present work, the measured first- and second-order statistics of flow and temperature will be used for comparison with simulations.

2.3 Numerical method

2.3.1 Governing equations

The steady-state RANS simulations were performed assuming a constant-property incompressible fluid and eddy viscosity/diffusivity hypotheses for turbulent transport. The Reynolds averaged velocity (U_i) and temperature (T) transport equations are:

$$\frac{\partial U_i}{\partial t} + U_j \frac{\partial U_i}{\partial x_j} = -\frac{1}{\rho}\frac{\partial p}{\partial x_i} + \frac{\partial}{\partial x_j}\left[(\nu + \nu_t)\frac{\partial U_i}{\partial x_j}\right] \tag{2.1}$$

$$\frac{\partial T}{\partial t} + U_j \frac{\partial T}{\partial x_j} = \frac{\partial}{\partial x_j}\left[(\alpha + \alpha_t)\frac{\partial T}{\partial x_j}\right] \tag{2.2}$$

where ν and α are the kinematic viscosity and thermal diffusivity of the fluid, respectively, whereas ν_t and α_t are the eddy viscosity and thermal diffusivity, [19].

2.3.2 Turbulence models

The standard $k-\varepsilon$ turbulence model is widely used in CFD to predict turbulent transport of momentum and different variants are currently available in industrial tools. It was also selected as a basic turbulence model in the present study. The additional transport equations of turbulent kinetic energy (k) and its dissipation rate (ε) are:

$$\frac{\partial k}{\partial t} + U_j \frac{\partial k}{\partial x_j} = P_k - \varepsilon + \frac{\partial}{\partial x_j}\left[\left(\nu + \frac{\nu_t}{\sigma_k}\right)\frac{\partial k}{\partial x_j}\right] \tag{2.3}$$

$$\frac{\partial \varepsilon}{\partial t} + U_j \frac{\partial \varepsilon}{\partial x_j} = (C_{\varepsilon_1} P_k - C_{\varepsilon_2}\varepsilon)\frac{\varepsilon}{k} + \frac{\partial}{\partial x_j}\left[\left(\nu + \frac{\nu_t}{\sigma_\varepsilon}\right)\frac{\partial \varepsilon}{\partial x_j}\right] \tag{2.4}$$

where $P_k = \left[\nu_t \left(\frac{\partial U_i}{\partial x_j} + \frac{\partial U_j}{\partial x_i} \right) - \frac{2}{3}\delta_{ij}k \right] \frac{\partial U_i}{\partial x_j}$ represents the modeled production of turbulent kinetic energy. The eddy viscosity can now be defined as:

$$\nu_t = C_\mu \frac{k^2}{\varepsilon} \tag{2.5}$$

where σ_k, C_{ε_1}, C_{ε_2}, σ_ε and C_μ are model coefficients ([31]) listed in Table 2.1.

Table 2.1: Model coefficients of the $k-\varepsilon$ turbulence model.

C_μ	C_{ε_1}	C_{ε_2}	σ_k	σ_ε
0.09	1.44	1.92	1	1.3

The standard wall functions were used for all turbulent quantities along the adiabatic walls. The low-Reynolds variant of the $k-\varepsilon$ model is usually applied when more accurate predictions of the local wall-heat transfer is required, [20] [15]. In the present work, we also consider such class of turbulence models. We selected $k-\varepsilon-\zeta-f$ turbulence model of [21] due to its numerical robustness and limited sensitivity to the grid non-uniformities. In this model, a velocity scale ratio $\zeta = \overline{v^2}/k$, replaced the original "wall-normal" velocity scale $\overline{v^2}$, which was previously proposed in [22] and [23]. The elliptic function f is also introduced in order to mimic separately the viscous wall-blocking effect. The final version of the model includes two additional transport equations:

$$\frac{\partial \zeta}{\partial t} + U_j \frac{\partial \zeta}{\partial x_j} = f - \frac{\zeta}{k} P_k - \varepsilon + \frac{\partial}{\partial x_j} \left[\left(\nu + \frac{\nu_t}{\sigma_\zeta} \right) \frac{\partial \zeta}{\partial x_j} \right] \tag{2.6}$$

$$L^2 \nabla^2 f - f = \frac{1}{\tau} \left(C_1 + C_2 \frac{P_k}{\varepsilon} \right) \left(\zeta - \frac{2}{3} \right) \tag{2.7}$$

where σ_ζ, C_1 and C_2 are model coefficients, listed in Table 2.2.

Table 2.2: Model coefficients of the $k-\varepsilon-\zeta-f$ turbulence model.

C'_μ	C'_{ε_1}	C'_{ε_2}	σ_ζ	a	C_τ	C_η	C_L
0.22	$1.4\left(1 + \frac{0.012}{\zeta}\right)$	1.9	1.2	0.6	6	85	0.36

In contrast to the standard $k-\varepsilon$ models, both the length (L) and global dynamical time (τ) scales are now bounded by the Kolmogorov scales in combination with Durbin's realizability constraints as:

$$\tau = max \left[min \left(\frac{k}{\varepsilon}, \frac{a}{\sqrt{6}\, C'_\mu \mid S \mid \zeta} \right), C_\tau \left(\frac{\nu}{\varepsilon} \right)^{\frac{1}{2}} \right] \tag{2.8}$$

$$L = C_L\, max \left[min \left(\frac{k^{\frac{3}{2}}}{\varepsilon}, \frac{k^{\frac{1}{2}}}{\sqrt{6}\, C'_\mu \mid S \mid \zeta} \right), C_\eta \left(\frac{\nu^3}{\varepsilon} \right)^{\frac{1}{4}} \right] \tag{2.9}$$

where S is the stress-strain tensor, while a, C_τ, C_η and C_L are model coefficients reported in Table 2.2. Finally, the eddy viscosity can be defined as:

$$\nu_t = C'_\mu \zeta k \tau \tag{2.10}$$

with C'_μ as a model coefficient. The boundary conditions used in the elliptic-relaxation based turbulence models are as follows: zero-values were imposed to ν_t, k and ζ, while $\varepsilon = 2\nu k/\delta^2$ and $f = -2\nu\zeta/\delta^2$, where δ is the wall distance. It is expected that the more advanced $k-\varepsilon-\zeta-f$ model will predict more accurately the near-wall phenomena when compared to the standard $k-\varepsilon$ model employing the wall-functions. On the other hand, the numerical mesh needs to be refined to get the characteristic non-dimensional wall distance less than one, which will significantly increase the computational costs. For flows in the non-confined geometries, such as in the present planar jet with heated co-flow, it is interesting to compare these two approaches, especially in the jet-spreading region, where the wall effects are diminishing.

2.3.3 Turbulent heat transfer models

The simplest way of modeling of the turbulent heat flux is to apply so called "simple-gradient hypothesis", as follows:

$$\overline{\theta u_i} = -\alpha_t \frac{\partial T}{\partial x_i} \tag{2.11}$$

where the eddy diffusivity (α_t) is calculated though the Reynolds analogy:

$$\alpha_t = \frac{\nu_t}{\mathrm{Pr_t}} \tag{2.12}$$

In the present work, two values of the turbulent Prandtl number are considered: the standard value (Pr_t=0.85) and the value recommended for the low-Prandtl fluids (Pr_t=2), [3]. Departing from this constant-value approach, Pr_t-correlations for low-Prandtl fluids are also available in the literature. One of the most popular is so-called Kays correlation derived from the series of experimental data on pipe and duct flows for various values of Prandtl number, [13]:

$$\mathrm{Pr_t}^{Kays} = 0.85 + \frac{2}{\frac{\nu_t}{\nu}\mathrm{Pr}} \tag{2.13}$$

Another approach in modeling of the turbulent heat flux is to use additional transport equations for energy of the temperature fluctuations (temperature variance, k_θ) and its dissipation rate (ε_θ), i.e. [24], [25], [26], [14], which eliminates necessity to define the turbulent Prandtl number. Here, we will apply a recent low-Prandtl $k-\varepsilon-k_\theta-\varepsilon_\theta$ model of [15], which was extensively validated for the wall-confined flows:

$$\frac{\partial k_\theta}{\partial t} + U_j \frac{\partial k_\theta}{\partial x_j} = \frac{\partial}{\partial x_j}\left[\left(\alpha + \frac{\alpha_t}{\sigma_{k_\theta}}\right)\frac{\partial k_\theta}{\partial x_j}\right] + P_{k_\theta} - \varepsilon_\theta \tag{2.14}$$

$$\begin{aligned}\frac{\partial \varepsilon_\theta}{\partial t} + U_j \frac{\partial \varepsilon_\theta}{\partial x_j} &= \frac{\partial}{\partial x_j}\left[\left(\alpha + \frac{\alpha_t}{\sigma_{\varepsilon_\theta}}\right)\frac{\partial \varepsilon_\theta}{\partial x_j}\right] \\ &+ \left(C_{p_1} P_{k_\theta} - C_{d_1}\varepsilon_\theta\right)\frac{\varepsilon_\theta}{k_\theta} + \left(C_{p_2} P_k - C_{d_2}\varepsilon\right)\frac{\varepsilon_\theta}{k}\end{aligned} \tag{2.15}$$

where $P_{k_\theta} = \alpha_t \left(\frac{\partial T}{\partial x_j} \right)^2$ is the production term of temperature variance (k_θ), while σ_{k_θ}, $\sigma_{\varepsilon_\theta}$, C_{p_1} and C_{p_2} are model coefficients, listed in Table 2.3.

Table 2.3: Model coefficients of the $k_\theta - \varepsilon_\theta$ heat transfer model.

C_θ	C_{p_1}	C_{p_2}	C_{d_1}	B_∞	σ_{k_θ}	$\sigma_{\varepsilon_\theta}$	C_γ
0.1	0.925	0.9	1	0.9	1.4	1.4	0.3

The remaining C_{d_2} coefficient is a function of the turbulent Reynolds number (defined as $R_t = k^2/(\varepsilon\nu)$) and normalized wall distance (defined as $R_\delta = \delta(\varepsilon\nu)^{1/4}/\nu$) and is calculated as:

$$C_{d_2} = \left[1.9 \left(1 - 0.3 e^{-0.0237 {R_t}^2} \right) - 1 \right] \left(1 - e^{-0.1754 R_\delta} \right)^2 \tag{2.16}$$

The eddy diffusivity is defined as:

$$\alpha_t = C_\theta k \tau_{l_\theta} \tag{2.17}$$

where C_θ is model coefficient reported in Table 2.3, and τ_{l_θ} is the local thermal characteristic time scale calculated as:

$$\tau_{l_\theta} = (f_{1_\theta} B_{1_\theta} + f_{2_\theta} B_{2_\theta}) \tag{2.18}$$

which consists of the asymptotic, mixed and local contributions, implicitly defined as:

$$f_{1_\theta} = \left(1 - e^{-0.0526 R_\delta \sqrt{Pr}} \right) \left(1 - e^{-0.0714 R_\delta} \right) \tag{2.19}$$

$$B_{1_\theta} = \tau_u B_\infty \tag{2.20}$$

$$f_{2_\theta} B_{2_\theta} = \tau_u \left(f_{2a_\theta} \frac{2R}{R + C_\gamma} + f_{2b_\theta} \sqrt{\frac{2R}{Pr}} \frac{1.3}{\sqrt{Pr} {R_t}^{3/4}} \right) \tag{2.21}$$

$$f_{2a_\theta} = f_{1_\theta} e^{-4 \cdot 10^{-6} R_t^2} \tag{2.22}$$

$$f_{2b_\theta} = f_{1_\theta} e^{-2.5 \cdot 10^{-5} R_t^2} \tag{2.23}$$

where C_γ and B_∞ are constants also reported in Table 2.3. Here, the time-scale ratio is defined as $R = \tau_\theta / \tau_u$, with the global dynamical time scale $\tau_u = k/\varepsilon$, and the global thermal time scale $\tau_\theta = k_\theta/\varepsilon_\theta$. The boundary conditions at the wall are zero values of k_θ and α_θ, whereas zero-gradient is applied for ε_θ.

2.3.4 Computational code

The OpenFOAM-2.4.0 CFD code was used to perform the RANS simulations. All numerical simulations were executed in the steady mode. This steady mode approach proved to be appropriate because of the strong stabilizing effect of the imposed co-flow in the closed test section, which practically eliminated a typical oscillatory behavior of plumes and other forced convection jets, [27]. This was additionally proven by ability to get a fully convergent solutions for all performed simulations, which will be impossible if any kind of the oscillatory behavior will be triggered. The simulations were performed by using the SIMPLE algorithm for coupling between the velocity and pressure fields. The

second-order central differencing scheme was used to discretize the gradient and Laplacian terms, whereas the second-order TVD scheme was used for the divergence terms, [28]. The steady simulations were performed with typical under-relaxation parameters of 0.1 for the pressure, 0.3 for the velocity and 0.5 for all remaining turbulence variables. The convergence criterion of 10^{-8} was applied (and achieved) for all variables.

2.3.5 Computational domain and boundary conditions

The experimental test section was represented using two computational domains and three different numerical meshes, Fig. 2.2.

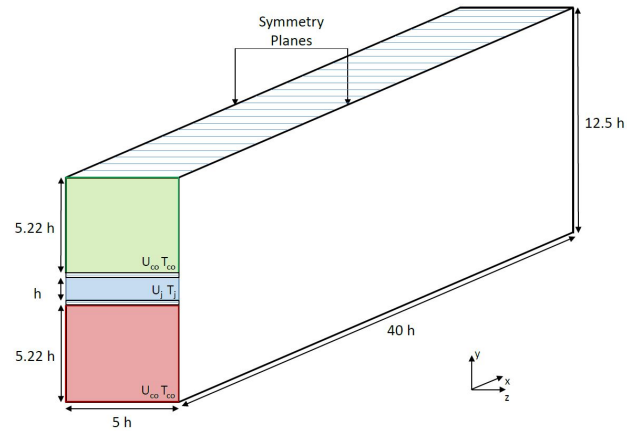

(a)

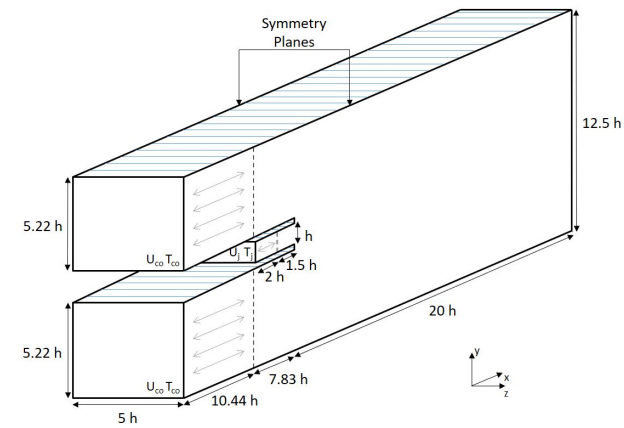

(b)

Figure 2.2: Sketch of the computational domains D1 (a) and D2/D2.1 (b).

It was decided to generate three-dimensional symmetrical domains in order to have a

universal configuration which can be used also for initialization of velocity and temperature fields, as well as to check the required numerical resolution of a high-fidelity CFD approach (Large Eddy Simulation) (the follow-up numerical study). The first computational domain (defined as 'D1') was designed to be as simple as possible. It is starting at the nozzle outlet plane of the experimental setup, which makes it possible to simply prescribe measured profiles of the velocity and turbulence kinetic energy. This option is also used to mimic some experimentally observed imperfections (in terms of the asymmetrical distributions of the incoming flow, which will have a significant impact on the flow profiles in the jet mixing zone). These can be investigated further by modeling the actual shape of the curved inlet segment of the experimental wind tunnel, but this was not considered in the present work. The second computational domain (defined as 'D2') was created to achieve a more universal description of planar jet flow, estimating possible design-specific deviations from the theoretical behavior (i.e. unbalanced co-flows at the jet side). In the 'D2' configuration, three periodic channels were set as the pre-cursor simulation domains in order to provide the fully developed flows before entering the jet-mixing zone. The special attention was devoted to obtaining the desired characteristic ratio between the velocity magnitude of the central jet and its co-flow counterparts. This was achieved by taking the most uniform co-flow side from experiments (the left side) with the mean inlet velocity of 3.15 m/s, which was set to both co-flow inlets. Then, the mean jet velocity is imposed to be 14.97 m/s to ensure the total flow rate balance. Expectations were to get a reasonable agreement with experimental data mainly in the left-side and in the center of the jet. The coordinate system in the numerical model of the experimental test section was oriented in such a way that U, V, and W represent the velocity components in streamwise (x), crosswise (y) and spanwise (z) directions, respectively. Gravity effects were neglected considering the high Reynolds number of the jet (experimentally, about 18000), which also leads to a Richardson number much lower than the unity. Both working fluids (air and He-Xe gas mixture) were assumed to have a constant kinematic viscosity, $\nu = 1.55 \cdot 10^{-5}$ m^2/s, whereas the thermal properties assumed molecular Prandtl numbers of 0.71 and 0.2, respectively. Fixed-scalar inlet conditions were set for temperature in both domains. In case of air, co-flow and jet inlet temperatures were $T_{CO} = 311.1$ K and $T_J = 299.1$ K, respectively. In case of the He-Xe gas mixture, they were $T_{CO} = 307.5$ K for the co-flow and $T_J = 295.5$ K for the jet. These values resulted from the monitoring of experimental inlet conditions, showing that the target temperature difference of 12 K was actually maintained during the MYRTE wind tunnel operation. Finally, turbulent quantities were also imposed as uniform fixed-scalar values at the channels inlet of pre-cursor simulations (only the very first iteration) of domains D2 and D2.1, i.e. $k^{in} = 1.5\left(I_t\ \overline{U}\right)^2$, with $\overline{U}$ is the mean velocity (obtained from PIV), $I_t = 0.1$ is the turbulence intensity, and $\varepsilon^{in} = \left(C_\mu^{3/4}(k^{in})^{3/2}\right)/0.07h$ is the dissipation rate of the turbulent kinetic energy. For the temperature variance and its dissipation rate, following values are imposed, $k_\theta = 10^{-3}$ K^2, and $\varepsilon_\theta = 10^{-3}$ K^2/s, respectively. The remaining boundary conditions were analogously set in both domains D1 and D2. The crosswise-normal surfaces were defined as no-slip adiabatic walls. The spanwise-normal patches were defined as symmetry planes. The outlet boundary condition was set to zero-gradient for velocity and turbulent quantities. A zero-gradient inlet condition was also set for the pressure while this was fixed at a reference

value of zero at the outlet.

2.3.6 Mesh details

Three different meshes were generated as a consequence of the selected turbulence models. In domains D1 and D2, the standard $k-\varepsilon$ model was solely used (i.e. the high-Reynolds model with wall-functions) while the $k-\varepsilon-\zeta-f$ was tested in a domain D2-variant (D2.1) (i.e. the low-Reynolds model with integration up to the wall). The D2.1 configuration is geometrically identical to the D2, but with a significantly finer numerical mesh in the proximity of walls. To better visualize differences from meshes in domains D2 and D2.1, Figure 2.3 shows details around the jet nozzle.

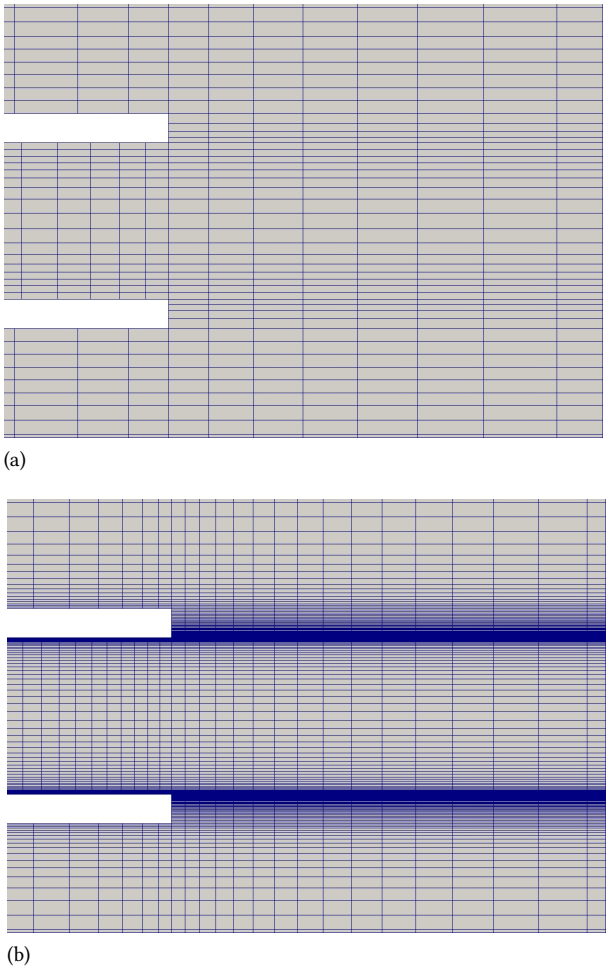

(a)

(b)

Figure 2.3: Mesh details at the inlet from computational domains D2 (a) and D2.1 (b).

The most important mesh specifications are collected in Tables 2.4 and 2.5.

Table 2.4: Mesh details of the jet-spreading region from the different computational domains.

	N_x	N_y	N_z	$Total$	$l_c\,[mm]$
D1	120	141	11	$186.1k$	4.94
D2	36	113	11	$44.8k$	6.3
D2.1	46	283	21	$273.4k$	3.45

Table 2.5: Mesh details of the periodic jet and co-flow channels in domains D2 and D2.1.

	${N_x}^J$	${N_y}^J$	${N_x}^{CO}$	${N_y}^{CO}$	N_z	$Total^{Jet}$	$Total^{Coflow}$	y^{+Jet}	$y^{+Coflow}$
D2	14	17	29	44	11	$2.6k$	$14k$	22	11
D2.1	28	67	58	62	21	$39.4k$	$75.5k$	0.5	0.9

In addition to the partial (in the jet-spreading and co-flow regions) and the total amount of control volumes, additional information containing the characteristic non-dimensional wall distance (y^+) and typical mean cell length (l_c, which was defined as the cubic-root of the ratio between the total volume of specific subdomain and number of the control volumes in that region, providing an indication of the isotropic mesh element size). To verify the initial formation of the mixing layer, additional mesh sensitivity analyses were also performed by doubling the number of control volumes in the streamwise direction (which are indicated with '(f)').

2.4 Results and discussion

2.4.1 Qualitative analysis of flow and temperature fields

In order to provide a qualitative analysis of the planar jet flow behavior at Pr = 0.2 (He-Xe gas mixture), contour plots in the central (x, y)-plane for domain D2.1 are presented in Figs.2.4-2.6.

Note that all plots are extracted from results obtained by the most comprehensive low-Reynolds models, using the $k-\varepsilon-\zeta-f$ for the flow fields and $k_\theta-\varepsilon_\theta$ for thermal fields. We start our analysis with a presentation of typical flow and turbulence parameters associated with the velocity field. The contours of the velocity magnitude show a centrally located plane jet, which is additionally stabilized by the co-flow jets (which are just slightly visible due to rather small flow ratio U_{CO}/U_J = 0.21), Fig.2.4(a). This strong shear between the central and co-flow jets is the major source of the turbulence kinetic production, which can be observed from contours of the turbulent kinetic energy in Fig. 2.4(b). The global dynamical time scale ($\tau_u = k/\varepsilon$) distribution, shown in Fig. 2.4(c), portrays that the central jet region (where the turbulent diffusion is the dominant mechanism) and the edges of the central jet (where the shear-production is dominant mechanism) are characterized by the smallest length-scales at which dissipation of turbulence takes place. The contours of the parameter ($\zeta = \overline{v^2}/k$), are plotted in Fig. 2.4(d). Note that ($\overline{v^2}$) should be analyzed as the intensity of the velocity fluctuations perpendicular to the flow direction, and is reduced to its classical definition of the normal turbulent-stress component in the proximity of

the wall. Next to small regions close to the inlet plane (resulting from the incoming wall-bounded channel), the strongest deviation of $\overline{v^2}$ from the total turbulence kinetic energy ($k = 0.5(\overline{u_i u_i})$) coincides with strong-shear regions.

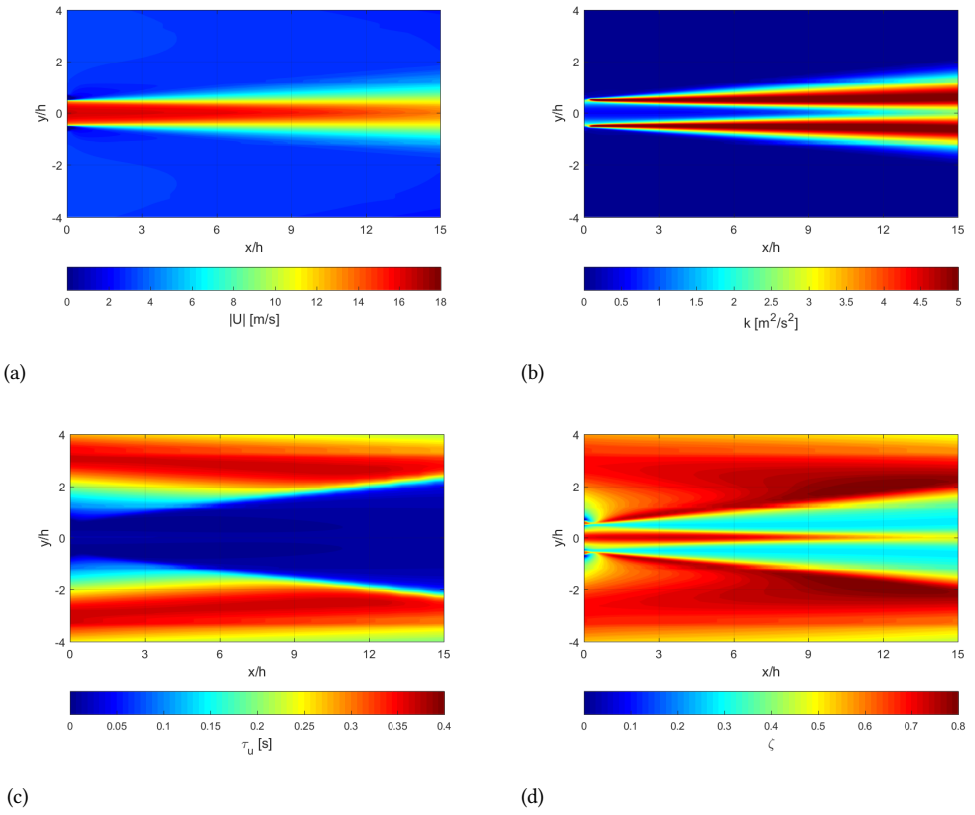

Figure 2.4: Contours of velocity magnitude (a), turbulent kinetic energy (b), global dynamical time-scale (c) and velocity-scale ratio (d) from the low-Reynolds ($k-\varepsilon-\zeta-f$) + ($k_\theta-\varepsilon_\theta$) turbulence model (domain D2.1).

Distributions of the mean temperature and temperature variance show a similar trend as for the velocity field counterparts, Figs. 2.5(a) and (b). On first sight, it can be surprising considering the low value of the Prandtl number ($Pr = 0.2$), which should lead to the different dynamic behavior of the velocity and thermal fields. On another hand, the considered case is strongly dominated by the forced convection, which makes the molecular contributions to the heat flux almost negligible in the central part of the jet. The differences between the temperature variance (Fig.2.5(b)) and turbulent kinetic energy (Fig.2.4(b)) are more pronounced. The former one shows the highest values in the proximity of the inlet, with a diminishing trend as the central jet is developing, whereas the latter one shows the consistent behavior. The contours of the global thermal time-scale are shown in Fig. 2.5(c). It can be seen that contours show a similar distribution to the previously analyzed global

dynamical time-scale (shown in Fig. 2.4(c)), with the smallest values in the center and along edges of the jet. Finally, contours of the turbulent Prandtl are plotted in Fig. 2.5(d). Here, the turbulent Prandtl number is evaluated (by combining Eqs.(2.10) and (2.17)) as:

$$\mathrm{Pr_t} = \frac{\nu_t}{\alpha_t} = \frac{C_\mu^{'}\ \overline{v^2}\ \tau}{C_\theta\ k\ \tau_{l_\theta}} \tag{2.24}$$

It can be seen that a strongly non-uniform distribution of $\mathrm{Pr_t}$ is obtained (similarly to [29]), with values varying in the 0.2 - 2 range. The lower values of the $\mathrm{Pr_t}$ are obtained in regions bounded with the shear-layers and central jet, indicating the regions where the turbulent thermal diffusion dominates over the turbulent momentum diffusion.

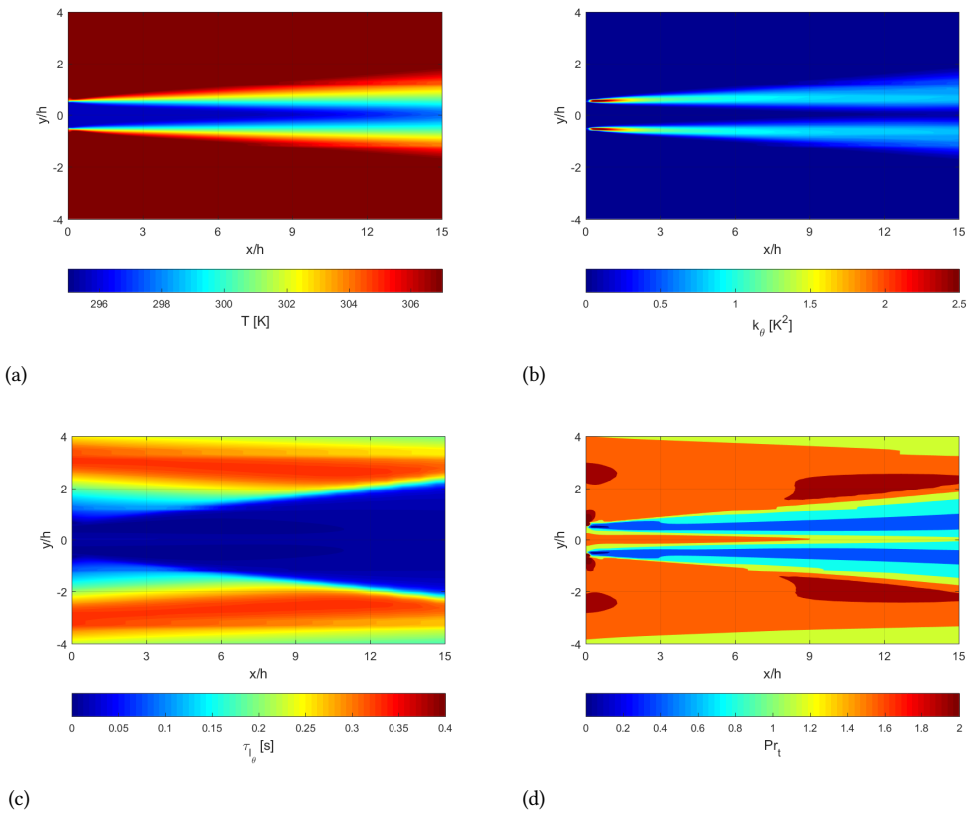

Figure 2.5: Contours of temperature (a), temperature variance (b), local thermal time scale (c) and turbulent Prandtl number (d) at $Pr = 0.2$, obtained from the low-Reynolds $(k-\varepsilon-\zeta-f)+(k_\theta-\varepsilon_\theta)$ turbulence model (domain D2.1).

Finally, Fig.2.6 shows the ratio between turbulent and molecular viscosity (a) and diffusivity (b). It can be seen that this ratio is significantly larger for the momentum transfer compared to its thermal counterpart.

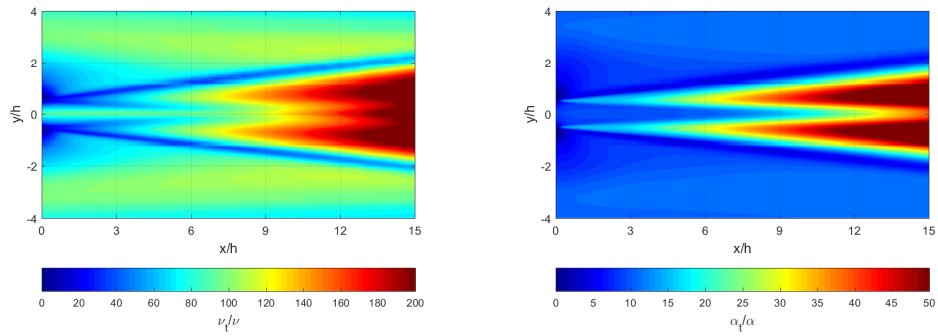

(a) (b)

Figure 2.6: Contours of turbulent to molecular viscosity (a) and diffusivity (b) ratios at $Pr = 0.2$, obtained from the low-Reynolds $(k-\varepsilon-\zeta-f)+(k_\theta-\varepsilon_\theta)$ turbulence model (domain D2.1).

2.4.2 Quantitative analysis of the flow field

We will consider next a detailed comparative assessment between the PIV measurements and numerical simulations. The streamwise velocity and turbulent kinetic energy were normalized by characteristic difference between the inlet experimental and numerical jet- and co-flow velocities (defined as $\Delta U = U_J - U_{CO}$). Since two-dimensional PIV measurements were performed, the streamwise ($\overline{uu}$) and crosswise ($\overline{vv}$) turbulent stress components are directly available. The total turbulent kinetic energy is estimated as $k_{\text{PIV}} = 0.5\left(\overline{uu}_{\text{PIV}} + \overline{vv}_{\text{PIV}} + \overline{ww}\right)$, with $\overline{ww} = 2/3\overline{vv}_{\text{PIV}}$ ([19]), and this value is used for comparison with RANS results.

We evaluate first the inlet profiles of the non-dimensional streamwise velocity and turbulent kinetic energy profiles for the central jet of 'D2' and 'D2.1' configurations, in order to check that fully developed turbulence profiles are obtained, Fig. 2.7. Note that 'D2' indicates coarser mesh and application of the high-Reynolds turbulence model, while 'D2.1' indicates a refined numerical mesh with integration up to the wall of the low-Reynolds turbulence model. The profiles are extracted at $x/h = -2.5$, i.e. at the half-length of the periodic channels. It can be concluded that for both RANS models a good agreement is obtained for the non-dimensional streamwise velocity in comparison with the DNS data of [30], Fig.2.7(a). In contrast to that, profiles of the turbulent kinetic energy reveal that high-Reynolds variant of the model is not able to accurately predict the near-wall behavior, with a significant under-prediction of the characteristic peak, Fig.2.7(b). This is in accordance with a known deficiency of the standard high-Reynolds $k-\varepsilon$ model of [31]. Prediction of the low-Reynolds $k-\varepsilon-\zeta-f$ RANS model shows significant improvement and overall good agreement with the DNS profiles of the turbulent kinetic energy. This improvement is due to the accurate prediction of the wall-blockage effect included through the elliptic-relaxation approach. Additional mesh sensitivity analysis is performed by doubling the number of control volumes in the x-direction (as indicated by '(f)'). It can be seen that the obtained results are grid-independent. The same validation exercise was also performed in case of the periodic co-flow channels providing an analogous result, i.e. the

fully developed turbulence profiles were obtained.

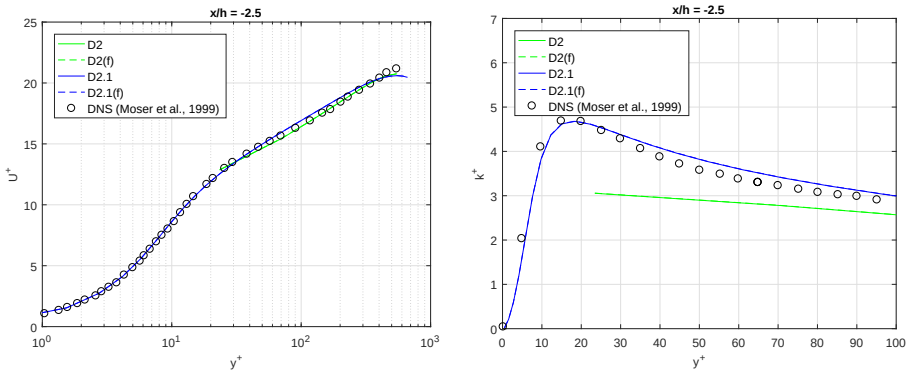

(a) (b)

Figure 2.7: Universal log-law profiles of velocity (a) and turbulent kinetic energy (b) as jet inlet conditions in domain D2 (the high-Reynolds turbulence model) and D2.1 (the low-Reynolds turbulence model). Note that (f) indicates the mesh refinement with a factor two in the streamwise direction.

The profiles of the non-dimensional streamwise velocity and turbulent kinetic energy exactly at the inlet plane (at $x/h = 0$) are shown in Fig. 2.8. It is obvious that experimental data are showing asymmetrical distributions ('D1' domain), caused by some constraints of the experimental setup, which include a presence of internal components and a convergent-shape of co-flow channels. The extended simulation domain results (with pre-cursor simulation to get fully developed profiles) exhibit, as expected, symmetrical profiles ('D2' and 'D2.1' domains). It should be noted that differences between the 'D1' and 'D1(f)' profiles are due to the sampling settings in OpenFOAM, since the values in the centers of control volumes are used instead of their cell-faces. Consequently, results obtained in 'D1(f)' domain show a better agreement with experiments at $y/h = 0.5$ and $y/h = -0.5$ locations due to their smaller distance of the first row of control volumes from the inlet plane in comparison to 'D1' domain, Fig. 2.8(a). It can be also seen that the low-Reynolds RANS model ('D2.1') captures the best characteristic wakes at the nozzle near-wall regions (located in the proximity of above mentioned $y/h = 0.5$ and -0.5 locations). The profiles of non-dimensional turbulent kinetic energy show larger differences between simulations and experiments, Fig. 2.8(b). In addition to already mentioned asymmetrical behavior, there is also a significant difference in predicting the characteristic peaks, indicating that simulated fully developed inflows are underpredicting the turbulence intensity in the co-flow channels, whereas its intensity in the central-jet inflow is overpredicted - independently on used turbulence model (i.e. for both high- ('D2') and low-Reynolds ('D2.1') models, respectively). In the central jet, this can be explained by partial laminarization effects due to nozzle constriction, as discussed in [32].

The effects of the experimentally observed asymmetrical distributions and symmetrical fully developed turbulence conditions will be compared at different streamwise locations, $x/h = 3, 5, 7$, respectively, in Fig. 2.9. At $x/h = 3$ location, the peak of the central jet velocity and its cross-wise spreading show an overall good agreement with experiments,

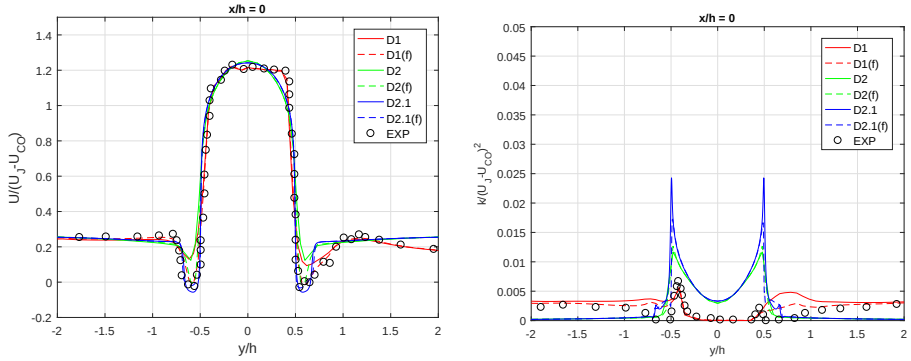

(a) (b)

Figure 2.8: Profiles of normalized streamwise velocity (a) and turbulent kinetic energy (b) at the jet inlet.

Fig. 2.9(a). The low-Reynolds RANS model results ('D2' and 'D2.1') show a slight overprediction for the upper co-flow region ($y/h > 0$). At the same location, the numerically predicted non-dimensional turbulent kinetic energy profiles show significant underprediction in the central jet region for both models, Fig. 2.9(b). It is surprising that the PIV data exhibit behavior with identical peaks, despite of the non-symmetrical trends at $x/h = 0$. Agreement with PIV measurements is better in the co-flow regions for the high-Reynolds model ('D1' and 'D1(f)') results. The low-Reynolds model ('D2.1') shows the best agreement with measurements for the mean streamwise velocity component at $x/h = 5$ location, Fig. 2.9(c). The only deviation is obtained for the upper co-flow region. The high-Reynolds model ('D1') shows better prediction in this upper co-flow region, but cross-wise spreading is significantly underpredicted. Agreement between measurements and simulations of turbulent kinetic energy profiles at this location is much better, as shown in Fig. 2.9(d). The peak values are well predicted with all models. The high-Reynolds model ('D1') shows good agreement in the co-flow regions, but underpredicts the level of turbulent kinetic energy in the jet center. With further increase of the distance from the inlet plane, $x/h = 7$, the experimentally observed asymmetry in the upper co-flow region increases for both velocity and turbulent kinetic energy profiles, Fig. 2.9(e) and (f). The velocity peak value is again well predicted with all models, Fig.2.9(e). The turbulent kinetic energy profiles indicate that the low-Reynolds ('D2.1') model shows the good prediction of the peaks, whereas the high-Reynolds ('D1') model is closest to PIV in the co-flow regions, Fig. 2.9(f). The profiles of the normalized turbulent shear stress component ($\overline{uv}$) at characteristic locations are shown in Fig. 2.10. The shear turbulent stress component prediction is important since it makes the most important source in the production of the turbulent kinetic energy. It can be seen that the asymmetrical distribution is again predicted better with the experimentally adjusted turbulent inlet for the high-Reynolds $k-\varepsilon$ model. In summarizing the quantitative analysis of the flow field, an overall good agreement between PIV measurements and RANS simulations is obtained. The cross-wise profiles of the mean streamwise velocity at different locations downstream from the inlet plane show a good prediction of the characteristic peak values in the center of the jet.

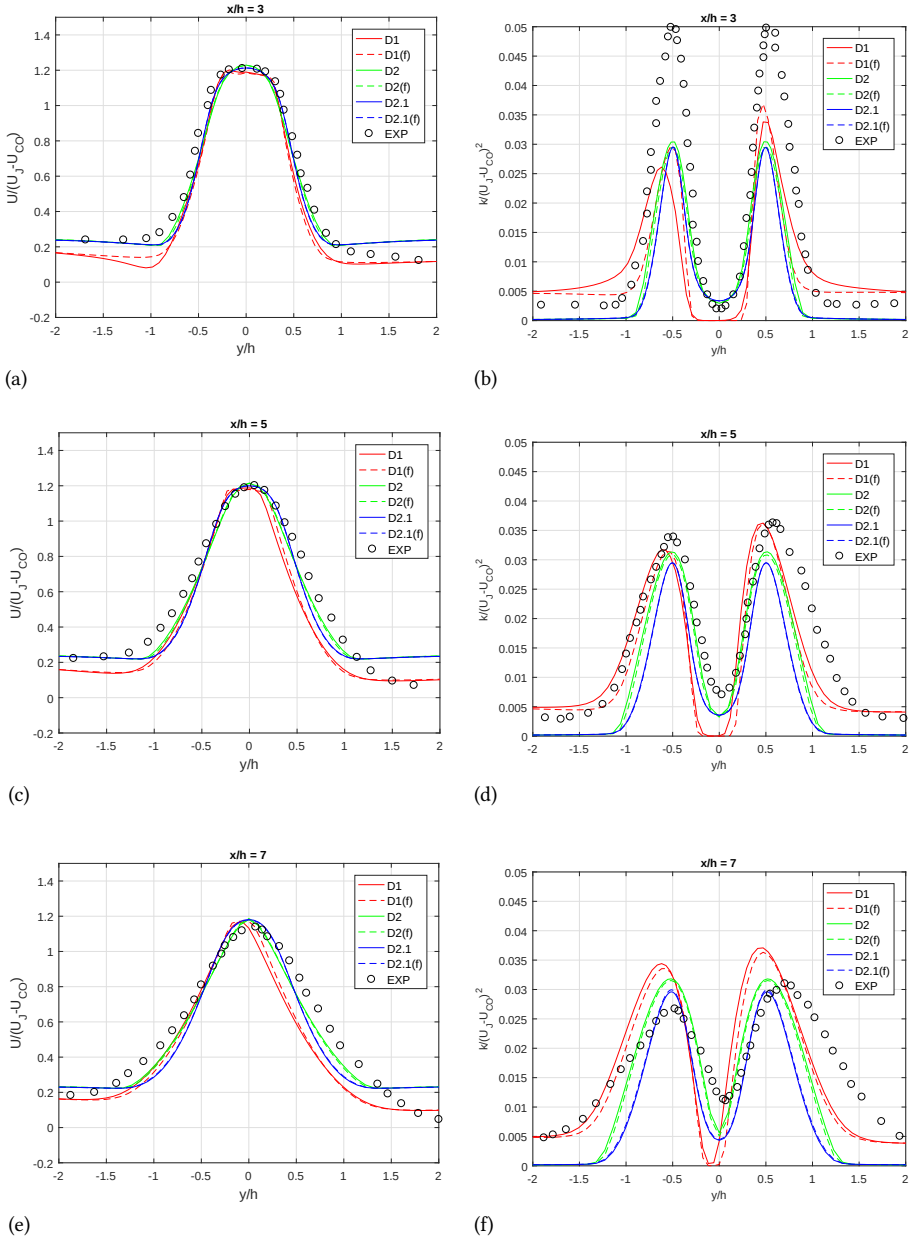

Figure 2.9: Profiles of normalized streamwise velocity (a, c, e) and turbulent kinetic energy (b, d, f) at different locations.

Also, the jet spreading is well captured too. Similarly, the simulated cross-wise profiles of the turbulent kinetic energy show a proper behavior with two characteristic peaks caused by strong shear between the central and co-flow jets. The experimental data of turbulent kinetic energy in comparison with the numerical results indicate more rapid decay of the peak values of turbulent kinetic energy in the streamwise direction. An additional attempt is made to mimic more closely asymmetrical distributions of measured profiles. It is shown that experimentally obtained differences between the upper and lower co-flow regions can be reasonably predicted by imposing corresponding inlet profiles for mean velocity and turbulent kinetic energy.

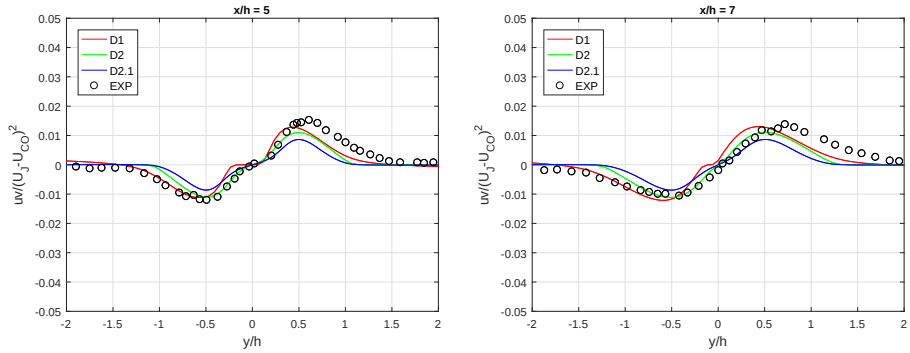

Figure 2.10: Profiles of normalized turbulent shear stress component ($\overline{uv}$) at different locations (a, b).

2.4.3 Quantitative analysis of the thermal field

Furthermore, we perform a comparison between measured and numerically obtained mean temperature profiles at two locations, x/h = 5 and 7, for two different values of Prandtl number, respectively, Figs.2.11 and 2.12.

During experiments, it was observed that the mean temperature of the working fluid was slightly increasing over time. This increase resulted in a time-dependent behavior of the jet and co-flow inlet temperatures. To eliminate these time-dependencies, the mean temperature was non-dimensionalized as: $T^* = (T_{CO} - T)/(T_{CO} - T_c)$, with T_c as the centerline temperature. Note that a constant uniform inlet temperature profiles of the central jet and co-flows were specified for all numerical simulations. For the air as working fluid case, a simple Reynolds analogy in the modeling of the turbulent heat flux is applied with the characteristic values of the turbulent Prandtl number of Pr_t = 0.85. It can be seen that a reasonable agreement is obtained with experimental data at both locations (Fig.2.11). The agreement is best for the 'D1' model where the asymmetrical inlets are imposed, although the cross-wise spreading is still underpredicted compared to the experiments. For the low-Prandtl working fluid case (Pr = 0.2), various approaches in modeling the turbulent heat flux are tested, including: (i) the Reynolds analogy with two values of the turbulent Prandtl number (Pr_t = 0.85 and 2, respectively), (ii) the Prandtl number is evaluated from Kays correlation, and finally (iii) the full six-equation low-Reynolds model $k - \varepsilon - \zeta - f - k_\theta - \varepsilon_\theta$

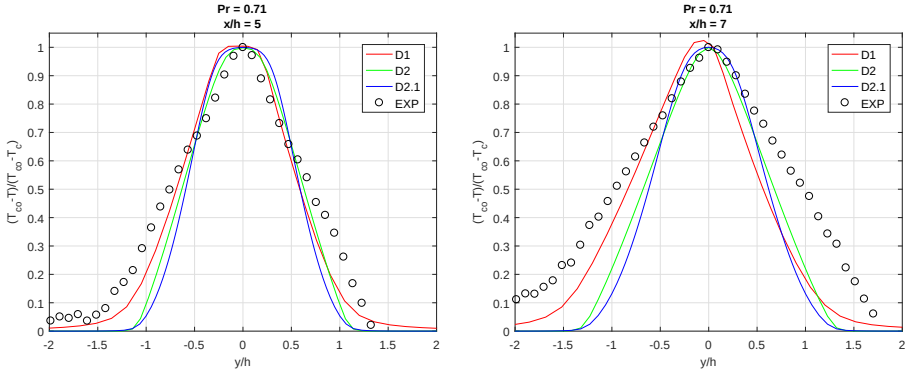

Figure 2.11: Profiles of normalized temperature at Pr = 0.71 and Pr_t = 0.85 from domains D1, D2 and D2.1 at different locations (a, b).

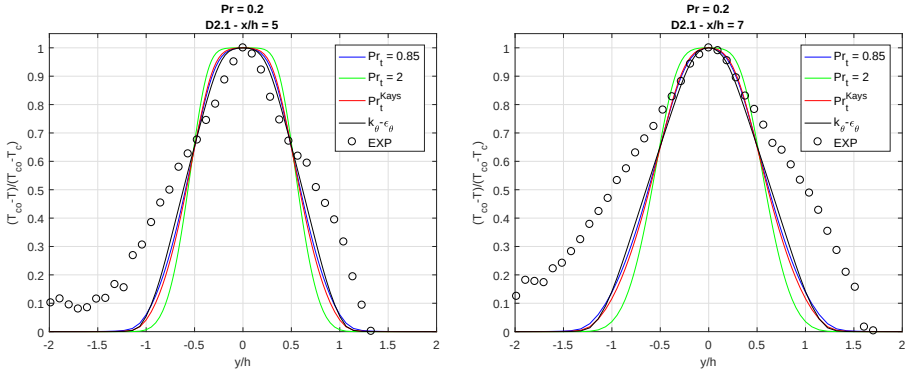

Figure 2.12: Profiles of normalized temperature at Pr = 0.2 with different THT models from domain D2.1 at different locations (a, b).

model, which does not require specification of the Pr_t. From the non-dimensional temperature profiles at x/h = 5 and 7, it can be concluded that more accurate modeling of the turbulent heat flux does not bring many differences, Fig. 2.12. The agreement between simulations and experiments is poor. The experiments indicate significantly wider and asymmetrical distributions outside the $-0.5 \leq y/h \leq 0.5$ region, whereas the numerical simulations exhibit theoretically more proper Gaussian-like profiles, which were also reported in experimental studies of [33]. In conclusion of the analysis of the thermal field, we postulate that agreement between experiments and simulations is still not satisfactory. This disagreement is most probably a consequence of a combination of the used measuring techniques and still some uncounted experimental heat losses since the numerical simulation profiles exhibit typical behavior in a close agreement with similar studies in the

literature.

2.5 Conclusions

A new experimental campaign was conducted at VKI on a forced planar jet with heated co-flow at two values of Prandtl number, Pr=0.71 (air) and 0.2 (He-Xe gas mixture). The PIV and thermocouple measurement data were used to validate the RANS simulations, which included a series of approaches ranging from a standard two-equation $k-\varepsilon$ to the state-of-art low-Reynolds elliptic-relaxation based $\zeta-f$ model. For temperature field predictions, a range of turbulent heat flux models was applied, ranging from the standard constant turbulent Prandtl number approach to a more elaborate $k_\theta-\varepsilon_\theta$ models. Overall good agreement between the experiments and simulations in predicting the cross-wise profiles of the mean velocity, turbulent kinetic energy and turbulent shear stress at different locations. The quality of agreement was improved when typical asymmetrical inlet conditions were imposed at the co-flow inlet planes. In contrast to the velocity field, the temperature profiles showed a good agreement in the central part of the domain (i.e. within the central jet region), whereas significant deviations were observed in the co-flow and connecting regions. A rather small differences between different turbulent heat flux models, which ranged from a standard constant turbulent Prandtl number to a more comprehensive model based on the solving of additional equations for the temperature variance and its dissipation rate ($k_\theta-\varepsilon_\theta$), indicated an overall dominance of the strong convective forced convection and passive behavior of the temperature. The more advanced models of the turbulent heat flux considered here will have a significantly more important role for mixed and especially natural convection situations involving low Prandtl fluids.

References

[1] R. Fernandez, D. De Bruyn, P. Baeten and H. Ait Adberrahim, The evolution of the primary system design of the MYRRHA facility, IAEA-CN-245-258 2017.

[2] K. Van Tichelen, F. Mirelli, M. Greco and G. Viviani, E-SCAPE: A scale facility for liquid-metal, pool-type reactor thermal hydraulic investigations, Nuclear Engineering and Design 290 (2015) 65–77.

[3] G. Grotzbach, Challenges in low-Prandtl number heat transfer simulation and modelling, Nuclear Engineering and Design 264 (2013) 41–55.

[4] F. Roelofs, A. Shams, I. Otić, M. Bottcher, M. Duponcheel, Y. Bartosiewicz, D. Lakehal, E. Baglietto, S. Lardeau and X. Cheng, Status and perspective of turbulence heat transfer modelling for the industrial application of liquid metal flows, Nuclear Engineering and Design 290 (2015) 99–106.

[5] U. Knebel, L. Krebs, U. Muller and B. P. Axcell, Experimental investigation of a confined heated sodium jet in a co-flow, Journal of Fluid Mechanics 368 (1998) 51–79.

[6] N. Kimura, H. Miyakoshi and H. Kamide, Experimental investigation on transfer characteristics of temperature fluctuation from liquid sodium to wall in parallel triple-jet, International Journal of Heat and Mass Transfer 50 (2007) 2024–2036.

[7] I. Otić and A. Class, Numerical investigation of a heated sodium jet in a co-flow, FEDSM2007-37566 2007.

[8] D. Tenchine, S. Vandroux, V. Barthel and O. Cioni, Experimental and numerical studies on mixing jets for sodium cooled fast reactors, Nuclear Engineering and Design 263 (2013) 263–272.

[9] C. Le Ribault, S. Sarkar and A. Stanley, Large eddy simulation of a plane jet, Physics of Fluids 11(10) (1999) 3069–3083.

[10] C. Bogey and C. Bailly, Turbulence and energy budget in a self-preserving round jet: direct evaluation using large eddy simulation, Journal of Fluid Mechanics 627 (2009) 129–160.

[11] I. Di Venuta, A. Boghi, M. Angelino and F. Gori, Passive scalar diffusion in three-dimensional turbulent rectangular free jets with numerical evaluation of turbulent Prandtl/Schmidt number, International Communications in Heat and Mass Transfer 95 (2018) 106–115.

[12] B. A Kader, Temperature and concentration proles in fully turbulent boundary-layers, International Journal of Heat and Mass Transfer 24(9) (1981) 1541–1544.

[13] W. M. Kays, Turbulent Prandtl number - Where are we?, Journal of Heat Transfer 116 (1994) 284–295.

[14] S. Manservisi and F. Menghini, A CFD four parameter heat transfer turbulence model for engineering applications in heavy liquid metals, International Journal of Heat and Mass Transfer 69 (2014) 312–326.

[15] S. Manservisi and F. Menghini, CFD simulations in heavy liquid metal flows for square lattice bare rod bundle geometries with a four parameter heat transfer turbulence model, Nuclear Engineering and Design 295 (2015) 251–260.

[16] R. Da Via, S. Manservisi and F. Menghini, A $k-\Omega-k_\theta-\Omega_\theta$ four parameter logarithmic turbulence model for liquid metals, International Journal of Heat and Mass Transfer 101 (2016) 1030–1041.

[17] O. Errico and E. Stalio, Direct numerical simulation of low Prandtl number turbulent convection above a wavy channel, Nuclear Engineering and Design 290 (2015) 87–98.

[18] S. Buckingham, Experimental results on BFS and jet flow test case, MYRTE D3.14-v3 2018.

[19] S. B. Pope, Turbulent Flows, Cambridge University - Cambridge Univ. Press 2000.

[20] P. W. Jones and B. E. Launder, The prediction of laminarization with a two equation model of turbulence, International Journal of Heat and Mass Transfer 15 (1972) 301–314.

[21] K. Hanjalić, M. Popovac and M. Hadžiabdić, A robust near-wall elliptic-relaxation eddy-viscosity turbulence model for CFD, International Journal of Heat and Fluid Flow 25 (2004) 1047–1051.

[22] P. A. Durbin, Separated flow computations with the $k-\varepsilon-\overline{v^2}$ model, AIAA Journal 33 (1995) 659–664.

[23] F.S. Lien and G. Kalitzin, Computations of transonic flow with the v^2-f turbulence model, International Journal of Heat and Fluid Flow 22 (2001) 53–61.

[24] K. Abe , T. Kondoh and Y. Nagano, A new turbulence model for predicting fluid flow and heat transfer in separating and reattaching flows - II. Thermal calculations, International Journal of Heat and Mass Transfer 38(8) (1995) 1467–1481.

[25] K. Hanjalić, S. Kenjereš and F. Durst, Natural convection in partitioned two-dimensional enclosures at higher Rayleigh numbers, International Journal of Heat and Mass Transfer 39(7) (1996) 1407–1427.

[26] S. Kenjereš, K. Hanjalić, Convective rolls and heat transfer in finite-length Rayleigh-Benard convection: a two-dimensional numerical study, Physical Review E 62(6) (2000) 1–12.

[27] A. Fregni, D. Angeli, A. Cimarelli and E. Stalio, Direct numerical simulation of a buoyant triple jet at low-prandtl number, International Journal of Heat and Mass Transfer 143 (2019) 118466.

[28] H. K. Versteeg and W. Malalasekera, An introduction to computational fluid dynamics - The finite volume method, Longman Scientific & Technical 1995.

[29] L. P. Chua and R. A. Antonia, Turbulent Prandtl number in a circular jet, International Journal of Heat and Mass Transfer 33(2) (1990) 331–339.

[30] R. D. Moser, J. Kim and N. N. Mansour, Direct numerical simulation of turbulent channel flow up to Re_τ = 590, Physics of Fluids 11(4) (1999) 943–945.

[31] B. E. Launder and D. B. Spalding, The numerical computation of turbulent flows, Computed Methods in Applied Mechanics and Engineering 3 (1973) 269–289.

[32] L.H. Back , R. F. Cuffel and P. F. Massier, Laminarization of a turbulent boundary layer in nozzle flow - Boundary layer and heat transfer measurements with wall cooling, Journal of Heat Transfer 92(3) (1970) 333–344.

[33] F. Franco-Medrano, Y. Fukumoto, C. Velte and A. Hodzic, Mass entrainment rate of an ideal momentum turbulent round jet, Journal of Physics Society in Japan 86 (2017) 034401–034427.

3

Combined large-eddy and direct numerical simulations of a planar jet with heated co-flow with medium and low Prandtl fluids

In the present work, we have applied a combined dynamic Large-Eddy Simulation (LES) and Direct Numerical Simulation (DNS) approach for a three-dimensional planar jet in a turbulent forced convection regime (Re = 18000) with a heated co-flow. Results from LES are compared with Reynolds Averaged Navier-Stokes (RANS) simulations and experimental data. We have analyzed flow and heat transfer features for four values of the characteristic Prandtl numbers (Pr = 0.71, 0.2, 0.025, and 0.006), which are representatives of air, He-Xe gas mixture, Lead-Bismuth Eutectic (LBE), and sodium, respectively. The latter two low-Prandtl fluids have been considered because of their role as primary coolants in advanced fast pool-type reactor prototypes (such as the Multi-purpose Hybrid Research Reactor for High-tech Applications (MYRRHA) at SCK CEN, Belgium). We have provided detailed insights into instantaneous and long-term time-averaged behavior of the velocity and temperature fields (the first- and second-order moments). Furthermore, we have analyzed profiles of characteristic velocity and temperature time scales and dissipation rates, as well as the power spectra of the streamwise velocity component and temperature at several characteristic locations. The mean temperature profiles demonstrated rather low sensitivity for various values of the Prandtl number. In contrast, profiles of the temperature standard deviation exhibited larger variations, decreasing in magnitude with lower Prandtl values. Here presented results of the high fidelity numerical simulations (dynamic LES/DNS) for the low-Prandtl working fluids can be used for further development, testing, and validation of the advanced RANS-type turbulence models.

This chapter is fully based on the scientific publication:
***E. Cascioli**, S. Keijers, K. Van Tichelen, J. E. Vesper, S. Kenjereš, Combined large-eddy and direct numerical simulations of a planar jet with heated co-flow with medium and low Prandtl fluids, International Journal of Heat and Mass Transfer 191 (2022) 122774 .*

3.1 Introduction

Computational Fluid Dynamics (CFD) represents a powerful tool for thermal-hydraulics investigations, supporting both the design phase and safety analyses of advanced nuclear reactors. The Multi-purpose hYbrid Research Reactor for High-tech Applications (MYRRHA) is a prototype of advanced nuclear reactor technology cooled by liquid LBE, which is under design at the Belgian Nuclear Research Center (SCK CEN) [1]. This nuclear reactor prototype is characterized by a pool-type configuration in which all primary components are contained inside the main vessel. In this study, we focused on the upper and lower plena, where the jet-like mixing phenomena take place, [2]. Standard CFD tools are based on the Reynolds Averaged Navier-Stokes (RANS) approach where the eddy-diffusivity and a simple-gradient hypothesis are used as models of the turbulent momentum and heat flux, respectively, [3]. Furthermore, by introducing a constant turbulent Prandtl number (a ratio between eddy viscosity and eddy diffusivity), the Reynolds analogy is usually assumed between the dynamics of the turbulent velocity and thermal fields, [4]. This simplified approach demonstrated relatively good performances and reliability for working fluids with Prandtl number values close to one (i.e. $Pr \approx 1$). For the low-Prandtl number fluids, such as liquid metals, this simplified approach does not hold and more advanced Turbulent Heat Transfer (THT) models are required, [5]. Suitable options for industrial applications are four-equations ($k - \epsilon - k_\theta - \varepsilon_\theta$) models in combination with algebraic heat flux models, [6], [7], [8], [9], [10]. Due to the complexity of such RANS-type turbulence models, there is a continuous need for their detailed validation in various flow configurations and over a wide range of working parameters.

The detailed flow field characteristics and theoretical behavior of a turbulent submerged jet impingement were addressed in [11]. Transient features of the rectangular jet at a relatively low value of Reynolds number (Re = 2000) were presented in [12]. Numerical validation of the four-equation RANS-type turbulence model for the impinging jet test case was performed in [10]. The high-fidelity LES and DNS studies were performed for low-Prandtl fluids in the backward-facing step of [13] and natural convection boundary layer of [14], respectively.

The experimental investigations of the low-Prandtl fluids are challenging due to numerous limitations of measuring techniques, especially when the turbulent heat transfer is of main interest. Some important experimental studies of turbulent single jet flow for $Pr < 1$ fluids were conducted at the Karlsruhe Institute of Technology ([15]), and more recently at the von Karman Institute for Fluid Dynamics (VKI) ([16]). In the former, a confined heated sodium jet was analyzed in forced-, mixed-, and natural-convection regimes. In the latter, the MYRTE wind tunnel investigations were performed on a cold forced-convection planar jet surrounded by heated co-flows with air (Pr = 0.71) and He-Xe gas mixture (Pr = 0.2) as working fluids.

In the present work, we perform combined dynamic LES/DNS simulations on a simplified setup of the MYRTE wind tunnel, which was previously discussed and studied by using RANS-based turbulence model simulations, [17]. We cover an extensive range of Prandtl numbers: for air (Pr = 0.71) and He-Xe gas mixture (Pr = 0.2) (operative working fluids of the MYRTE wind tunnel), as well as for liquid metals, Lead-Bismuth Eutectic (LBE, which is the primary coolant of the MYRRHA nuclear reactor) (Pr = 0.025) and sodium (Pr = 0.006). We present the first- and second-order statistics of the velocity and tempera-

ture fields, as well as characteristic mechanical and thermal time-scales. Frequency-based power spectra of velocity and temperature at characteristic locations are analyzed too. This database can be used for additional validation and testing of advanced RANS models for forced-convection flows of low-Prandtl fluids, complementing the recent numerical studies of [18]. The possible future extensions include the application of such validated models for simulations of the complex multiple-jets in mixed, [19], and natural convection regimes, [20].

3.2 Numerical method

3.2.1 Fundamental equations

The fundamental transport equations of the instantaneous velocity and a passive scalar (temperature) are the conservation of mass, momentum and energy, as follows:

$$\frac{\partial \hat{U}_i}{\partial x_i} = 0 \tag{3.1}$$

$$\frac{\partial \hat{U}_i}{\partial t} + \frac{\partial \hat{U}_i \hat{U}_j}{\partial x_j} = -\frac{1}{\rho}\frac{\partial \hat{p}}{\partial x_i} + \nu \frac{\partial^2 \hat{U}_i}{\partial {x_j}^2} \tag{3.2}$$

$$\frac{\partial \hat{T}}{\partial t} + \frac{\partial \hat{U}_j \hat{T}}{\partial x_j} = \alpha \frac{\partial^2 \hat{T}}{\partial {x_j}^2} \tag{3.3}$$

where ρ, ν and α are the molecular density, kinematic viscosity and thermal diffusivity, respectively. In the present study, all thermophysical fluid properties are assumed to be constant. In the LES technique, a filtering operation is applied to instantaneous variables as:

$$\bar{f}(x) = \int_D \hat{f}(x') G(x, x', \bar{\Delta}) dx' \tag{3.4}$$

where D is the entire domain and G is the filter function. The latter determines the smallest size of turbulent and thermal structures which can be directly resolved. This size is related to the filter width, $\bar{\Delta}$. In most cases, the filter width is taken to be proportional to the grid cell length, l_c, as $\bar{\Delta} = n\ l_c$. In this work, $n = 1$ and for this reason unfiltered structures will be directly addressed as SubGrid-Scales (SGS). Applying Eq.(3.4) to Eqs.(3.2) and (3.3), filtered quantities (denoted with '-') appear in transport equations as:

$$\frac{\partial \overline{U_i}}{\partial t} + \frac{\partial \overline{U_i}\ \overline{U_j}}{\partial x_j} = -\frac{1}{\rho}\frac{\partial \overline{p}}{\partial x_i} - \frac{\partial \tau_{ij}}{\partial x_j} + \nu \frac{\partial^2 \overline{U_i}}{\partial {x_j}^2} \tag{3.5}$$

$$\frac{\partial \overline{T}}{\partial t} + \frac{\partial \overline{U_j}\ \overline{T}}{\partial x_j} = -\frac{\partial q_j}{\partial x_j} + \alpha \frac{\partial^2 \overline{T}}{\partial {x_j}^2} \tag{3.6}$$

where the SGS turbulent stresses, τ_{ij}, and turbulent heat flux, q_j, can be also defined as:

$$\tau_{ij} = \overline{U_i U_j} - \overline{U_i}\ \overline{U_j} \tag{3.7}$$

$$q_j = \overline{U_j T} - \overline{U_j}\ \overline{T} \tag{3.8}$$

and need to be modeled, [3].

3.2.2 Dynamic subgrid-scale Smagorinsky model

The dynamic estimate of the SGS contributions ([21]) significantly improved performances of the standard Smagorinsky approach, [22]. In the dynamic procedure, the SGS model coefficients are not prescribed *a priori*, but are locally calculated during the LES runtime. This is achieved by defining a test grid (denoted with ' ~ '), whose width is $\widetilde{\overline{\Delta}} = 2\overline{\Delta}$. Then, by applying the test-filter over the momentum equation, a new subtest-stress tensor (T_{ij}) is obtained as:

$$T_{ij} = \widetilde{\overline{U_i U_j}} - \widetilde{\overline{U_i}}\,\widetilde{\overline{U_j}} \tag{3.9}$$

It is shown in [21] that resolved stress can be expressed as:

$$L_{ij} = T_{ij} - \widetilde{\tau_{ij}} \tag{3.10}$$

and it can be explicitly evaluated from the large-scales as:

$$L_{ij} = \widetilde{\overline{U_i}\,\overline{U_j}} - \widetilde{\overline{U_i}}\,\widetilde{\overline{U_j}} \tag{3.11}$$

The same closure of the Smagorinsky model is applied for both the grid-filter and test-filter turbulent stresses with an identical value of the model coefficient C_s, and it can be written as:

$$\tau_{ij} - \frac{1}{3}\delta_{ij}\tau_{kk} = -2C_s\overline{\Delta}^2\,\overline{|S|S_{ij}} \tag{3.12}$$

$$T_{ij} - \frac{1}{3}\delta_{ij}T_{kk} = -2C_s\widetilde{\overline{\Delta}}^2\,\widetilde{\overline{|S|}}\,\widetilde{\overline{S_{ij}}} \tag{3.13}$$

where C_s is the dynamic Smagorinsky constant (to be determined), $\overline{S_{ij}} = \frac{1}{2}\left(\frac{\partial\overline{U_i}}{\partial x_j} + \frac{\partial\overline{U_j}}{\partial x_i}\right)$ and $\widetilde{\overline{S_{ij}}} = \frac{1}{2}\left(\frac{\partial\widetilde{\overline{U_i}}}{\partial x_j} + \frac{\partial\widetilde{\overline{U_j}}}{\partial x_i}\right)$ are the strain rate tensors evaluated at the grid-filter $\overline{\Delta}$ and test-filter $\widetilde{\overline{\Delta}}$, respectively. By combining Eqs.(3.10), (3.12) and (3.13), we have:

$$L_{ij} - \frac{1}{3}\delta_{ij}L_{kk} = 2C_sM_{ij} \tag{3.14}$$

where:

$$M_{ij} = \widetilde{\overline{\Delta}}^2\,\widetilde{\overline{|S|}}\,\widetilde{\overline{S_{ij}}} - \overline{\Delta}^2\,\widetilde{\overline{|S|S_{ij}}} \tag{3.15}$$

An adaptation of the original model, [21], was proposed in [23] who applied a least squares method to find an optimal value of C_s by minimizing the error in Eq.(3.14) as:

$$\left(e_{ij}\right)^2 = \left(L_{ij} - \frac{1}{3}\delta_{ij}L_{kk} - 2C_sM_{ij}\right)^2 \tag{3.16}$$

Since $e_{ij} = e_{ij}(C_s)$, by evaluating its first derivative in respect to C_s, i.e. $\partial\left(e_{ij}\right)^2/\partial C_s = 0$, we have:

$$C_s = \frac{1}{2}\frac{L_{ij}M_{ij}}{M_{ij}^2} \tag{3.17}$$

Finally, the turbulent SGS viscosity is calculated as:

$$\nu_{SGS} = C_s \overline{\Delta}^2 |\overline{S}| \tag{3.18}$$

which makes a complete closure of the filtered momentum equation. In the present work, instead of applying spatial averaging of C_s in the homogeneous directions, we introduce a local spatial averaging involving six neighboring control volumes. This local averaging procedure makes this approach suitable also for complex geometries. Furthermore, the SGS turbulent viscosity was also bounded such that $\nu_{SGS} \geq -\nu$, allowing for at least some backscattering, [24] [25].

3.2.3 Dynamic subgrid-scale turbulent Prandtl model

A standard approach to model the thermal SGS is to use the Reynolds analogy through imposing the turbulent Prandtl number as a scaling coefficient, [26] [27]:

$$\alpha_{SGS} = \frac{\nu_{SGS}}{\mathrm{Pr}_{SGS}} \tag{3.19}$$

Now, by imposing a simple-gradient-diffusion hypothesis, the unresolved turbulent heat flux will be calculated as:

$$q_j = -\alpha_{SGS} \frac{\partial \overline{T}}{\partial x_j} \tag{3.20}$$

In the present work, to make fully consistent dynamic procedure for both velocity and temperature fields, the turbulent Prandtl number is estimated similarly to the Smagorinsky coefficient presented above, [28]. Again, a least-square minimization is applied to obtain the smallest differences between the closure assumption and resolved turbulent heat flux, [29] [30], as:

$$\frac{1}{\mathrm{Pr}_{SGS}} = \frac{M_{ik}^2}{L_{ik} M_{ik}} \frac{P_j R_j}{P_j^2} \tag{3.21}$$

where:

$$L_{ik} = -\widetilde{\overline{U_i}\,\overline{U_k}} + \widetilde{\overline{U_i}}\,\widetilde{\overline{U_k}} \tag{3.22}$$

$$M_{ik} = \overline{\Delta}^2 \, |\tilde{\overline{S}}| \, \widetilde{\overline{S_{ik}}} - \overline{\Delta}^2 \, \widetilde{|\overline{S}| \, \overline{S_{ik}}} \tag{3.23}$$

$$R_j = \tilde{\overline{\Delta}}^2 \, |\tilde{\overline{S}}| \, \widetilde{\frac{\partial \overline{T}}{\partial x_j}} - \tilde{\overline{\Delta}}^2 \, \widetilde{|\overline{S}| \, \frac{\partial \overline{T}}{\partial x_j}} \tag{3.24}$$

The P_j is the test-filter resolved heat flux, which can be directly calculated from the resolved test-filter fields as:

$$P_j = \widetilde{\overline{U_j}\,\overline{T}} - \widetilde{\overline{U_j}}\,\tilde{\overline{T}} \tag{3.25}$$

Finally, we also bounded the thermal SGS diffusivity, similarly to the SGS viscosity, such as $\alpha_{SGS} \geq -\alpha$.

3.2.4 Computational code

The OpenFOAM-2.4.0 CFD code is used to perform the dynamic LESs. The dynamic SGS treatment for both momentum and temperature is originally implemented through additional source code libraries. The PISO algorithm is used for coupling between the velocity and pressure fields, [31]. The second-order central differencing scheme is used to discretize gradient, Laplacian, and divergence terms of transport equations. The second-order backward implicit scheme is applied for the time integration. The maximum local Courant number is limited to 1.2, whereas its mean value is kept below 1, [32].

3.3 Computational details

3.3.1 Computational domain

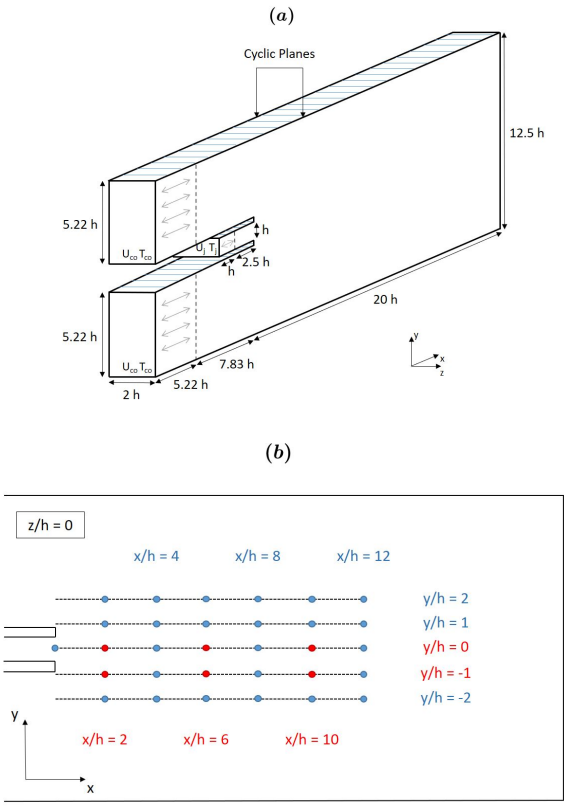

Figure 3.1: Sketch of the computational domain (a) and distribution of monitor points (b).

The adequate computational representation of the wind tunnel test section and exper-

imental inlet conditions were recently discussed in our previous work, where we have applied the RANS simulation approach, [17]. In the present study, we apply the most universal configuration containing three inlet periodic channels (pre-cursor simulations) representing the central jet and co-flow jets, which are mapped to the inlet plane of the simulation domain, as shown in Fig. 3.1(a). A network of monitoring points is distributed in the central vertical plane of the simulation domain to provide detailed insights into local spatial and temporal behavior of the velocity components and temperature, Fig. 3.1(b). The locations at which temporal spectra are analyzed in the present study are marked by red circles. The gravitational force effects are neglected due to a dominant forced convection flow regime with Reynolds and Richardson numbers (based on the experimental velocity difference between jet and co-flow) of Re = 18000 and Ri << 1, respectively, [17]. The most important geometrical dimensions are the jet nozzle height, h = 0.021 m, and jet-mixing domain length and height of 20h and 12.5h, respectively.

The special attention is devoted to obtain fully developed flows before entering the jet-mixing zone and limiting the total amount of control volumes for an affordable computational cost[1]. For this purpose, several simulations were performed to optimize the channel numerical mesh and periodicity length. We found that the periodicity lengths of 1h and 5.22h for the pre-cursor jet and co-flow channels, respectively, provided required fully developed flow conditions. To avoid any artificial numerical interference of the jet flow, the mapping location of the imposed pre-cursor periodicity is kept at the same distance as in our previous RANS simulation of identical configuration, [17]. Furthermore, the width of the simulation domain is limited to 2h to achieve the adequate mesh criteria for the LES (see below). Knowing that specific features of the experimental setup design affected uniformity of the inlet co-flows velocity, we select the co-flow with the most uniform distribution of the mean inlet velocity, [17]. Then, for both co-flow inlets, a uniform velocity of U_{co} = 3.15 m/s is imposed. To keep the mean flow rate balance as in the experiment, the mean jet velocity of U_{J} = 14.97 m/s is imposed at the inlet of the pre-cursor periodic central channel.

We apply a two-step procedure for the specification of the initial turbulence fluctuations. In the first step, entire flow and pressure fields are interpolated from the previous three-dimensional RANS-type simulations, [17]. The reference mean streamwise velocity is imposed at the pre-cursor channel inlets with random perturbation of the fluctuating velocity components, [33]. In this initialization stage, the periodicity distance of the pre-cursor simulation was significantly shortened (i.e. only 1/10 of periodic length was simulated) to allow the random perturbations to survive. In the second phase, as soon as the velocity fluctuations (monitored in time) have reached the end of shortened pre-cursor sub-channel, the random perturbations were switched off and the periodic length was set to the correct value.

At the outlet, the convective boundary condition is imposed for velocity. For the pressure, the zero-gradient boundary condition is applied at the inlets, while the zero value of the pressure is imposed at the outlet. The initial temperature of 298 K was set in the entire domain at the start of simulations. The jet and co-flow temperatures of T_J = 299.1 K and T_{CO} = 311.1 K were imposed to maintain the MYRTE wind tunnel experimental

[1]Numerical simulations were performed by using the ChemE computational cluster of the Applied Sciences Faculty at Delft University of Technology.

conditions ($\Delta T = T_{CO} - T_J = 12$ K temperature difference) for all the considered fluids. The zero-gradient temperature condition is applied at the outlet. At the side boundaries, the cyclic/periodic boundary conditions are imposed.

3.3.2 Mesh details

In the LES of a simple channel flow, the most demanding mesh resolution is in the proximity of walls. This mesh refinement is necessary to properly capture dynamics of the coherent turbulence structures (i.e. the quasi-streamwise vortices), [34]. The requirements of properly resolved turbulent boundary layers are $\Delta x^+ = 100$, $\Delta z^+ = 20$, and $y^+ \leq 1$, where the wall units are defined as $y^+ = u_\tau y/\nu$, [35]. The basic mesh contains in total $12.16{\cdot}10^6$ control volumes, and a finer mesh (denoted as '(f)') is generated by doubling the mesh distribution in the spanwise z-direction. An overview of the most important mesh specifications is given in Tables 3.1, 3.2 and 3.3. Note that a non-dimensional characteristic averaged scale, defined as $\left(\overline{l_c} = \sqrt[3]{\frac{\text{Domain volume}}{\text{Control volumes}}}\right)$, is also provided.

Table 3.1: Mesh details of one pre-cursor co-flow channel.

Mesh	N_x	N_y	N_z	Total	$u_\tau[m/s]$	y^+	Δx^+	Δz^+
Standard	83	124	150	$1.51 \cdot 10^6$ CVs	0.18	0.88	37	3
Finer (f)	83	124	300	$3.02 \cdot 10^6$ CVs	0.18	0.88	37	1.5

Table 3.2: Mesh details of the pre-cursor jet channel.

Mesh	N_x	N_y	N_z	Total	$u_\tau[m/s]$	y^+	Δx^+	Δz^+
Standard	100	133	150	$2.0 \cdot 10^6$ CVs	0.81	0.71	39	15
Finer (f)	100	133	300	$3.02 \cdot 10^6$ CVs	0.81	0.71	39	7.5

Table 3.3: Mesh details of the jet-mixing domain.

Mesh	N_x	N_y	N_z	Total	$\overline{l_c}$[m]
Standard	100	477	150	$7.16 \cdot 10^6$ CVs	$6.79 \cdot 10^{-4}$
Finer (f)	100	477	300	$14.32 \cdot 10^6$ CVs	$5.39 \cdot 10^{-4}$

The special attention is devoted to have an adequate numerical resolution for both velocity and passive scalar (temperature) fields for various values of simulated Prandtl numbers. The characteristic Kolmogorov and Corrsin length scales, [38], are estimated from simulations, being defined as:

$$\eta = \left(\frac{\nu^3}{\epsilon}\right)^{\frac{1}{4}}, \quad \eta_\theta = \eta \, \mathrm{Pr}^{-\frac{3}{4}} \tag{3.26}$$

The characteristic dissipation rate is calculated as $\epsilon = \nu \left\langle \left(\frac{\partial u_i'}{\partial x_j}\right)^2 \right\rangle$, with $u_i' = \hat{U}_i - \langle U_i \rangle$,

where the long-term time-averaging ($\langle ... \rangle$) is performed during the simulation runtime. Contours of the characteristic ratio between the local Control Volume (CV)-based length scale ($l_c = \left(\Delta_{\mathrm{CV}}\right)^{1/3}$) and temperature length scale (η_θ) are shown in Fig. 3.2. We kept constant value of the kinematic viscosity ($\nu = 1.55 \cdot 10^{-5}$ m^2/s), while adjusting the thermal diffusivity in the temperature equation such that $\alpha = \nu/\mathrm{Pr}$. It can be seen that for Pr = 0.71, Fig.3.2(a), we deal with a dynamic LES for both velocity and temperature fields. In contrast to this, for Pr = 0.2, Pr = 0.025 and Pr = 0.006, Figs.3.2(b),(c),(d), we have a fully resolved DNS for temperature field because of $l_c/\eta_\theta \leq 5$. It is noted that a proper $\Delta x^+/\Delta z^+$ proved to be essential for keeping an adequate numerical mesh for combined dynamic LES/DNS simulations over an entire range of Prandtl numbers.

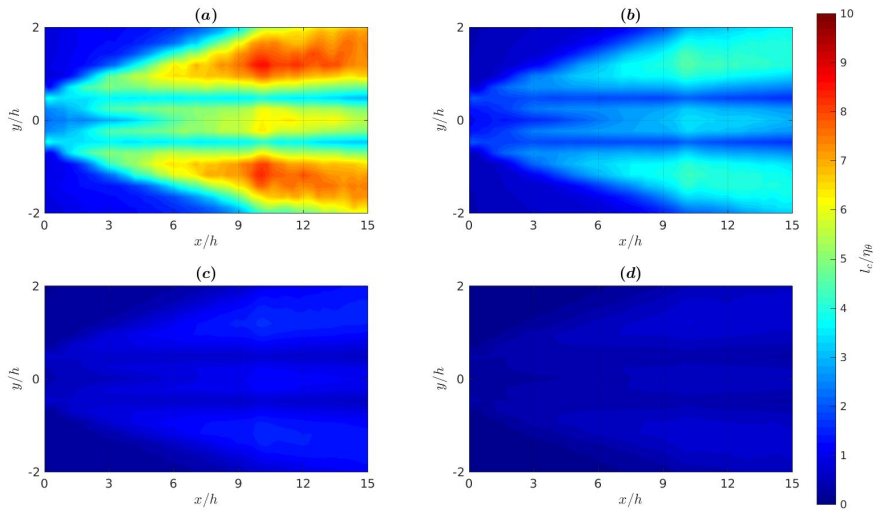

Figure 3.2: Contours of characteristic computational control volume length to smallest temperature scale ratio (l_c/η_θ) at Pr = 0.71 (a), 0.2 (b), 0.025 (c) and 0.006 (d).

3.4 Results

3.4.1 Qualitative analysis of the flow and thermal fields

To get an impression of the flow morphology of the simulated case, instantaneous three-dimensional distributions of the total vorticity and velocity are shown in Fig.3.3. The central high-velocity jet interacting with lower momentum co-flow jets produces well defined shear-layers, Fig.3.3(a). Contours of the instantaneous velocity in various vertical planes are shown in Fig.3.3(b). Here, the process of intensive mixing in the spanwise direction can be observed resulting in continuous weakening of the central jet. Also, the interface between the highly intermittent central jet region and laminar-like region farther away from co-flows can be easily identified.

Contours of the dynamically calculated and locally averaged Smagorinsky constant in the central vertical plane are shown in Fig. 3.4(a). The contours of the instantaneous vor-

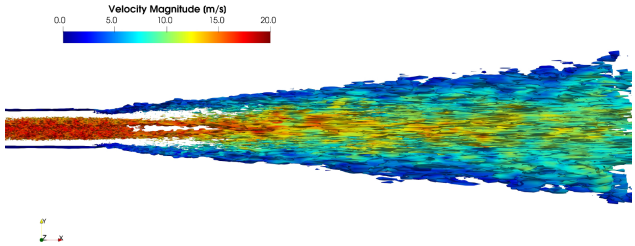

(a)

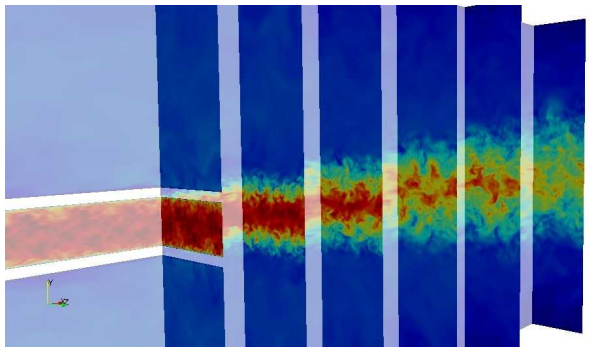

(b)

Figure 3.3: (a) The isosurface of the instantaneous vorticity ω_z = 2 kHz colored by the instantaneous velocity magnitude; (b) the contours of the instantaneous velocity magnitude in characteristic planes aligned and perpendicular to the jet direction.

ticity in the central vertical plane are shown in Fig.3.4(b). The highest concentration of the vorticity can be found in the shear-layers, as well as in the wake of the side-walls separating the central jet and co-flow jets. The instantaneous flow features are a combination of the Kelvin-Helmholtz instability of strong shear-layers, [37], and irregular reattachment of the weak regions behind the side-walls at the inlet plane (wake region). From Eq.(3.21), the contours of the locally calculated SGS turbulent Prandtl number, Pr_{SGS}, for the case with Pr = 0.71 are shown in Fig.3.4(c). It can be seen that the local distribution exhibits a significant variation. Starting from small values in the proximity of the inlets, Pr_{SGS} is close to one along the interface between the jet and outer co-flows, and finally, values larger than one are obtained in the core region of the central jet for $x/h > 3$.

The contours of the instantaneous streamwise velocity ($\overline{U_x}$) and long-term time-averaged turbulent kinetic energy in the central vertical plane are shown in Fig.3.5. The interface between the high-and low-velocity regions is easily distinguishable from contours of the instantaneous streamwise velocity, Fig.3.5(a). The contours of the turbulent kinetic energy ($k = 1/2\langle u_i^2 \rangle$) exhibit a characteristic initial double peak behavior, which originates from a strong shear between the central and co-flow jets, as shown in Fig.3.5(b). We will use these plots also to indicate local similarities and dissimilarities between the velocity and

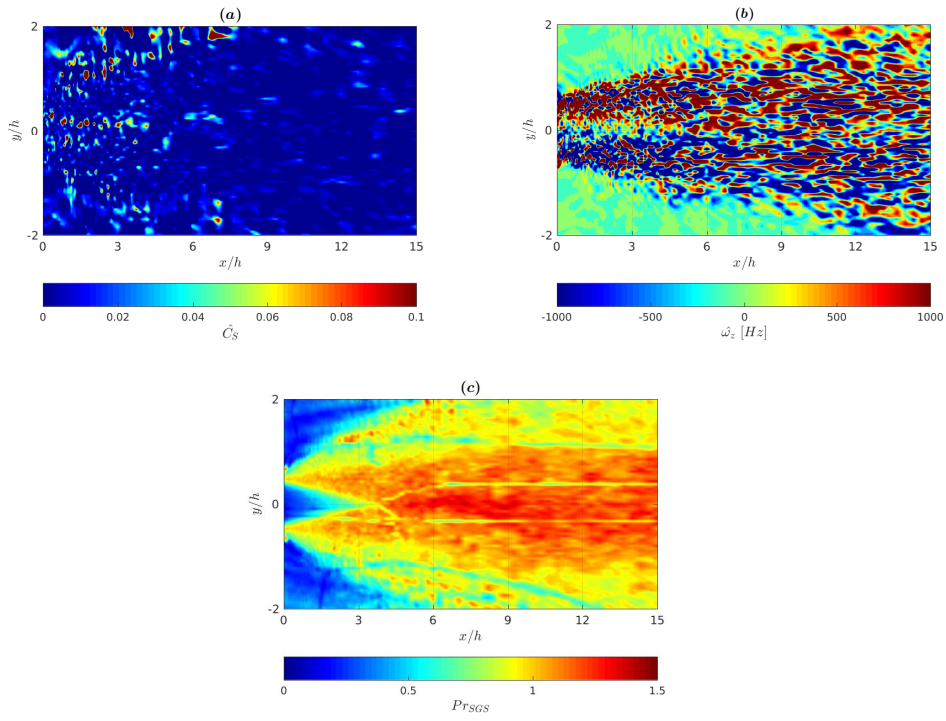

Figure 3.4: Contours of instantaneous dynamically calculated Smagorinsky constant (C_s) (a), instantaneous spanwise vorticity component (b) and subgrid-scale turbulent Prandtl number (Pr_{SGS}) at Pr = 0.71 (c), in the central vertical plane (z/h = 0).

thermal field distributions for different values of the Prandtl number.

Distributions of the instantaneous temperature for different Prandtl numbers (in the same plane) are shown in Fig.3.6. At Pr = 0.71 and Pr = 0.2 (Figs.3.6(a) and (b)), the thermal fluctuations are primarily driven by the velocity fluctuations resulting in corresponding fine-scale thermal imprints. In contrast to this behavior, with further reduction in Prandtl numbers, for Pr = 0.025 and Pr = 0.006, Figs.3.6(c) and (d), instantaneous temperature patterns exhibit more coarse-grained imprints, demonstrating increased importance of thermal diffusion (i.e. dampening of the thermal fluctuations).

Contours of the long-term time-averaged temperature variance ($k_\theta = 1/2\langle\theta^2\rangle$) (again in the central vertical plane) are shown in Fig.3.7. It can be seen that for Pr = 0.71 and Pr = 0.2 (Figs.3.7(a) and (b)), that the highest values are located in shear-layers, because of the highest temperature differences. With the increase of the distance from the inlet plane, as a result of intensive mixing, values of the temperature variance are gradually decreasing. For lower values of Prandtl number, Pr = 0.025 and Pr = 0.006 (Figs.3.7(b) and (c)), the behavior is different. The locations of the maximum temperature variance are moved farther downstream: $6 \leq x/h \leq 12$ for Pr = 0.025 and $9 \leq x/h \leq 12$ for Pr = 0.006.

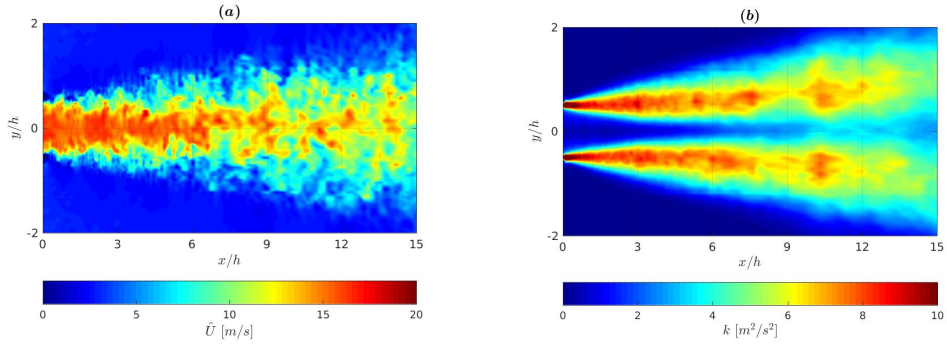

Figure 3.5: Contours of the instantaneous streamwise velocity (a) and long-term time-averaged turbulent kinetic energy (b) in the central vertical plane ($z/h = 0$).

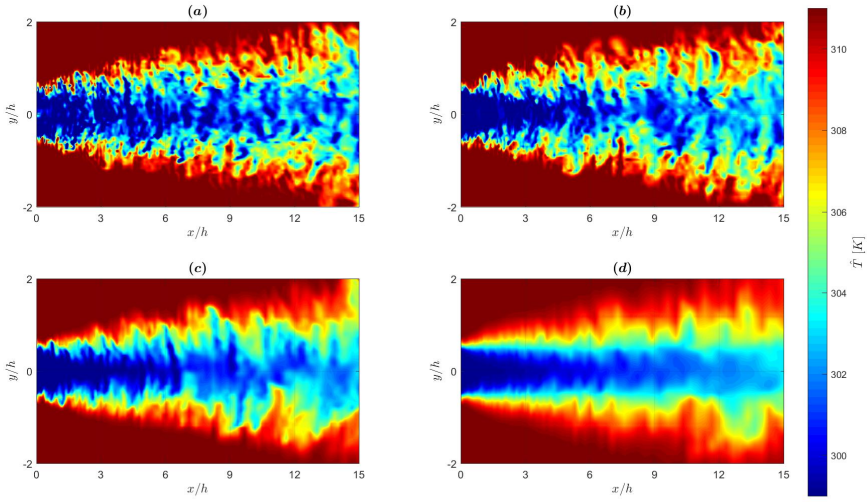

Figure 3.6: Contours of resolved instantaneous temperature ($\hat{T}$) at Pr = 0.71 (a), Pr = 0.2 (b), Pr = 0.025 (c) and Pr = 0.006 (d).

For the lowest simulated value of Pr = 0.006, instead of two distinct regions with high values of the temperature variance, a single region with its maximum along $y/h = 0$ is generated, Fig.3.7(d). This is the result of an overly dominant molecular thermal diffusion mechanism of temperature field, which results in effective suppression of the thermal turbulence contribution.

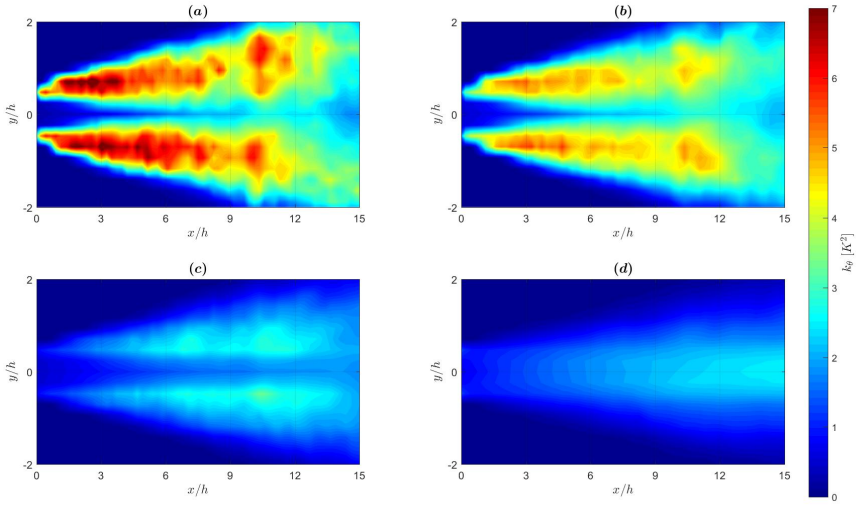

Figure 3.7: Contours of long-term time-averaged temperature variance ($k_\theta = \langle \theta' \theta' \rangle/2$, where $\theta' = \hat{T} - \langle \overline{T} \rangle$) at Pr = 0.71 (a), Pr = 0.2 (b), Pr = 0.025 (c) and Pr = 0.006 (d).

3.4.2 Quantitative analysis of the flow field

Next, we analyze the flow field. The long-term time-averaged quantities are obtained by collecting statistics for more than 60 characteristic Flow-Through Times (FTTs)[2]. The velocity profiles are compared against the MYRTE wind-tunnel measurements (denoted as 'EXP') and results from our previous RANS-type simulations (denoted as 'RANS'), [17]. For the latter, we use results of recently developed low-Reynolds $k-\epsilon-\zeta-f$ and $k_\theta-\epsilon_\theta$ model. First, we demonstrate that fully-developed turbulence conditions are generated and properly maintained in the pre-cursor simulations, Fig.3.8. It can be seen that both the log-law velocity profile (Fig.3.8(a)) and the turbulent kinetic energy (Fig.3.8(b)) agree very well with the reference DNS of [39], confirming a proper level of turbulence. This condition was adequate for both used numerical meshes on which the dynamic LES is performed, with a slight improvement for results obtained with the finer mesh (LES(f)) in the central part of the channel, Fig.3.8(b).

Next, we compare profiles of the non-dimensional mean streamwise velocity ($U/(U_J - U_{CO})$) at different distances from the inlet, i.e. $x/h = 0, 5, 10$ and 15, respectively, as shown in Fig.3.9. Exactly at the inlet plane ($x/h = 0$), there is a disagreement between the experiments and simulations due to some construction limitations of the inlet segment of the wind tunnel, [17]. These limitations resulted in an asymmetry between the two co-flow streams, at the sides of the jet. This asymmetry is eliminated by imposing fully-developed periodic boundary conditions in RANS and LES approaches. At $x/h = 5$ location, it can be seen that the LES produces significantly better agreement with experiments in comparison with the RANS, Fig.3.9(b). The central peak value and jet spreading in the spanwise

[2]The Flow-Through Time (FTT) is here defined as the time required by the massless fluid particle to move from the inlet to the outlet of the jet-mixing domain at the constant velocity of 14.97 m/s. This led to 1 FTT ≅ 0.03 s.

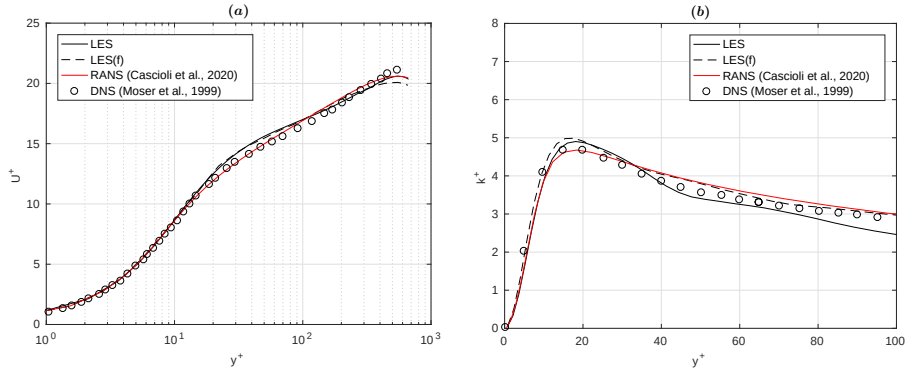

Figure 3.8: Profiles of the log-law velocity (in the semi-log plot diagram, U^+ vs. y^+) (a), and the long-term time-averaged non-dimensional turbulent kinetic energy ($k^+ = \langle u_i' u_i' \rangle / 2u_\tau^2$, where $u' = \hat{U} - \langle \overline{U} \rangle$) (b), both at the half of the periodicity length in the pre-cursor jet channel.

direction are well predicted. The RANS result shows weaker spreading and a higher peak in the jet center. The identical trend of the RANS and LES results is also present at locations farther downstream (i.e. at $x/h = 10$ and 15), Figs.3.9(c) and (d). A good agreement between LES results on two different numerical grids also confirms the reliability of the presented dynamic LES approach.

From the profiles of the long-term time-averaged turbulent kinetic energy at the same locations ($x/h = 0, 5, 10$ and 15), it can be concluded that simulations show significantly higher values in comparison with experiments. To check to what extent this difference can be attributed to the two-dimensionality of the experimental approach, the missing averaged velocity fluctuations in the z-direction are omitted from the LES results (noted as LES(2D)) in Fig.3.10). It can be seen that at $x/h = 5$ location, Fig.3.10(b) resulted in a closer agreement between the LES and experiments, but the general overestimating trend is still present. Interestingly, the peak values of the reduced turbulent kinetic energy from LES are now closer to the peak values from the RANS model, but the spanwise distribution is still significantly higher, Fig.3.10(b). Similar behavior is obtained at the $x/h = 10$, confirming more intensive turbulent mixing produced in LES in comparison with the RANS results. At $x/h = 15$, the profiles within the central jet region indicate similar trends between LES and RANS, whereas in the co-flow regions, the LES results again indicate stronger turbulence, Fig.3.10(d).

The profiles of the resolved turbulent shear-stress are shown in Fig.3.11. Again, the LES results show larger values compared to the RANS. At $x/h = 5$, both LES and RANS results are within the experimental data and in contrast to experiments, show proper symmetrical distributions, Fig.3.11(b). At $x/h = 10$ location, almost identical peak values as at $x/h = 5$ are obtained for both simulations, Fig.3.11(c). Finally, at $x/h = 15$, the peak values of the LES are reduced, and agreement between the LES and RANS is good in the central jet region, Fig.3.11(d). The profiles of the resolved turbulent shear stress at the same locations are shown in Fig.3.11. At $x/h = 5$ location, the experimental data are between the RANS and LES results, Fig.3.11(b). With further increase of the distance from the inlet, the RANS and

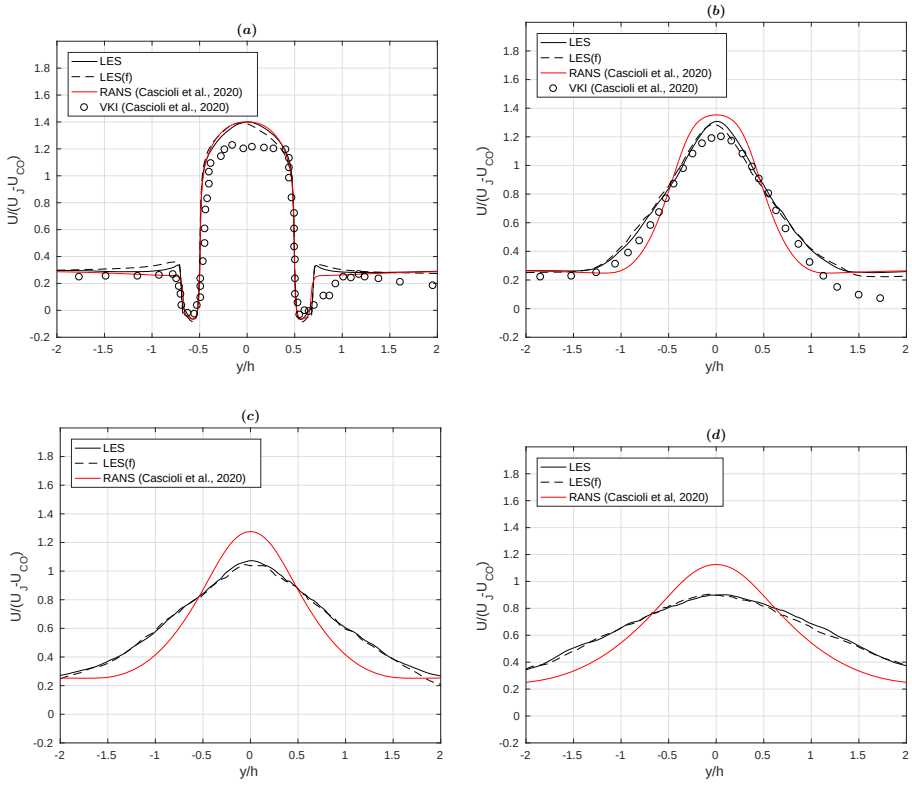

Figure 3.9: Profiles of the long-term time-averaged streamwise velocity component $(\langle\overline{U_x}\rangle/\left(U_J - U_{CO}\right))$ at x/h = 0 (a), 5 (b), 10 (c) and 15 (d).

LES results are getting closer, but the LES data indicate stronger turbulence in the co-flow regions.

Next we show profiles of the characteristic mechanical time-scale of the turbulence, i.e. $\tau_u = \langle k\rangle/\langle\varepsilon\rangle$, Fig.3.12. it can be seen that a good agreement is obtained at the x/h = 0 and 5 locations, Figs.3.12(a)(b). This can be initially surprising since large differences between the turbulent kinetic energy calculated from the RANS and LES are indicated in Fig.3.10(a). This larger value is also accompanied by a larger value of the dissipation, giving the final balanced outcome as shown in Fig.3.12(a). The larger differences are obtained at the intermediate location, x/h = 10, where the RANS profiles indicate much larger values in the co-flow regions, Fig.3.12(b). This can indicate low values of the dissipation (almost the laminar-like regimes), which in turn generates a large value of the mechanical time scale. This is followed by a very good agreement between the RANS and LES at x/h = 15, Fig.3.12(b).

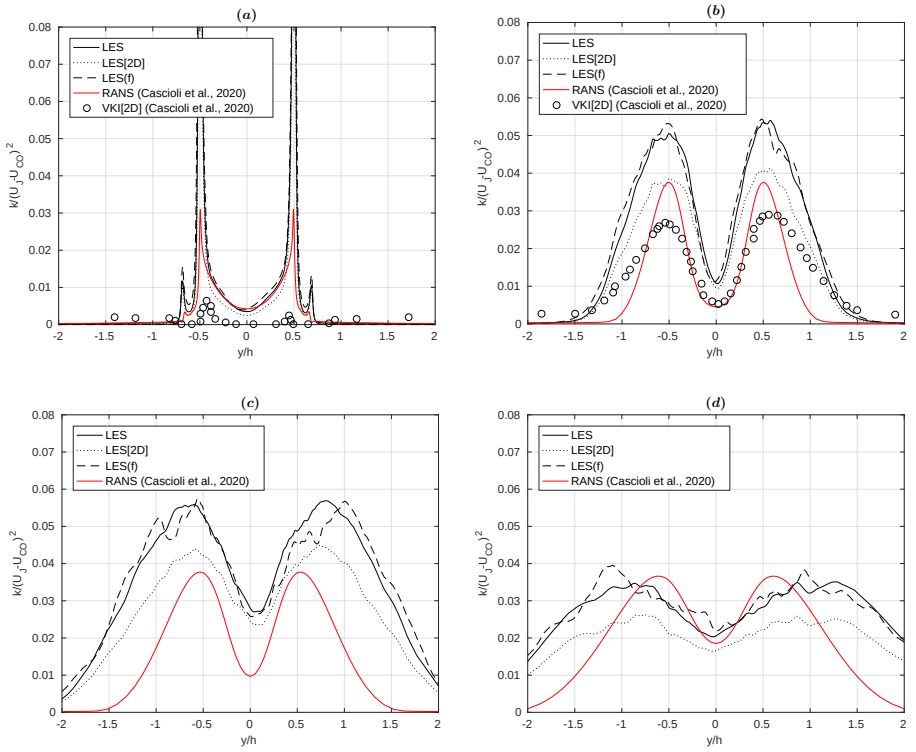

Figure 3.10: Profiles of the resolved time-averaged turbulent kinetic energy at x/h = 0 (a), 5 (b), 10 (c) and 15 (d). Note that LES(2D) indicate the omission of the spanwise velocity fluctuations component, i.e. $k_{2D} = \frac{1}{2}\left(\langle u'u'\rangle + \langle v'v'\rangle\right)$ where $u' = \hat{U} - \langle\overline{U}\rangle$.

3.4.3 Quantitative analysis of the thermal field

We move next to analyze the temperature field. It should be noted that the dynamic SGS for the thermal part was activated only for the Pr = 0.71, whereas for the remaining Prandtl numbers, the numerical resolution was sufficient to fully resolve the typical thermal scales, so we have a hybrid LES/DNS approach for velocity/temperature field, respectively. The resolved long-term time-averaged temperature profiles are shown in Fig.3.13. Effect of changing Prandtl number on temperature profiles is rather small. Note that the RANS results are shown only for Pr = 0.2 for which experimental data are available. It can be seen that the current LES/DNS profile at the $x/h = 5$ is closer to experimental values in comparison with the RANS results, Fig.3.13(b). The central jet peak value and spanwise spreading of the temperature are well captured with the LES/DNS. The RANS profile shows a significant overestimation of the peak value in the jet center and narrower distribution in the spanwise direction. This trend of the RANS profile is kept at other locations too, i.e. $x/h = 10$ and 15, Figs.3.13(c) and (d). At these locations, the LES/DNS results indicate that Prandtl number effects are primarily visible in the jet center, with significantly smaller

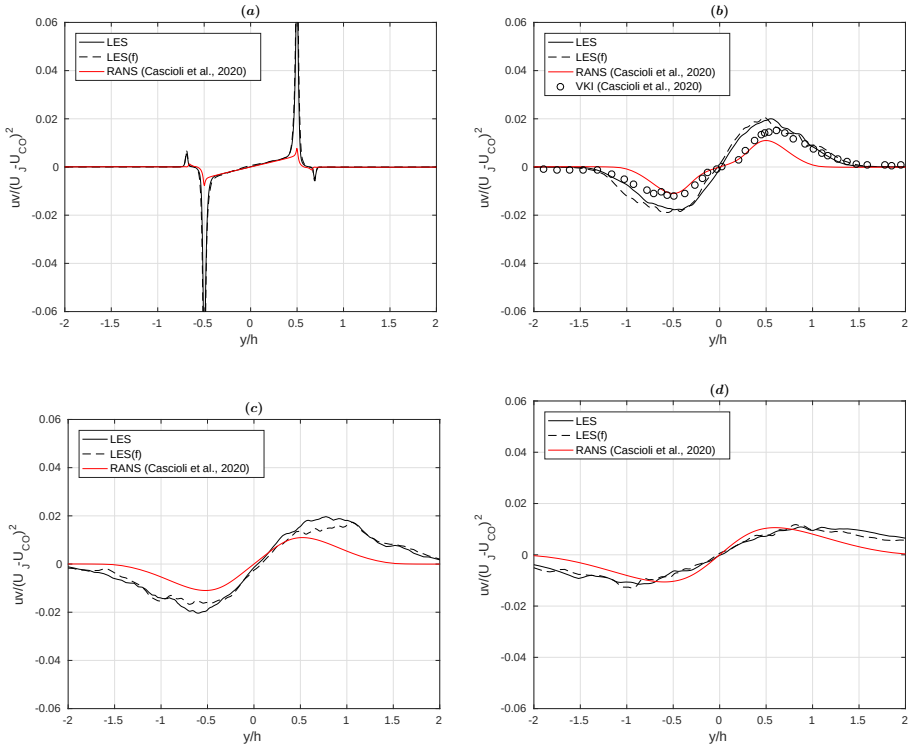

Figure 3.11: Profiles of the resolved time-averaged Reynolds shear stresses at x/h = 0 (a), 5 (b), 10 (c) and 15 (d).

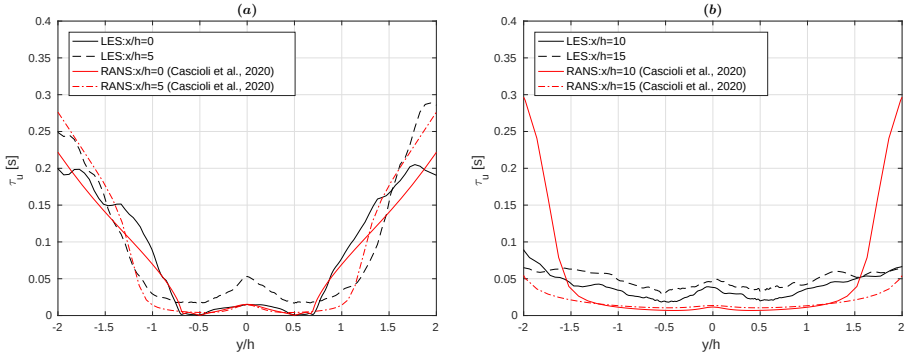

Figure 3.12: Profiles of resolved time-averaged dynamical time-scales in the convergent (a) and self-similar (b) regions of the jet.

differences in the co-flow regions. This additionally confirms that molecular diffusion plays a small role in the distribution of the temperature profiles, where the convective

and turbulence contributions are more important.

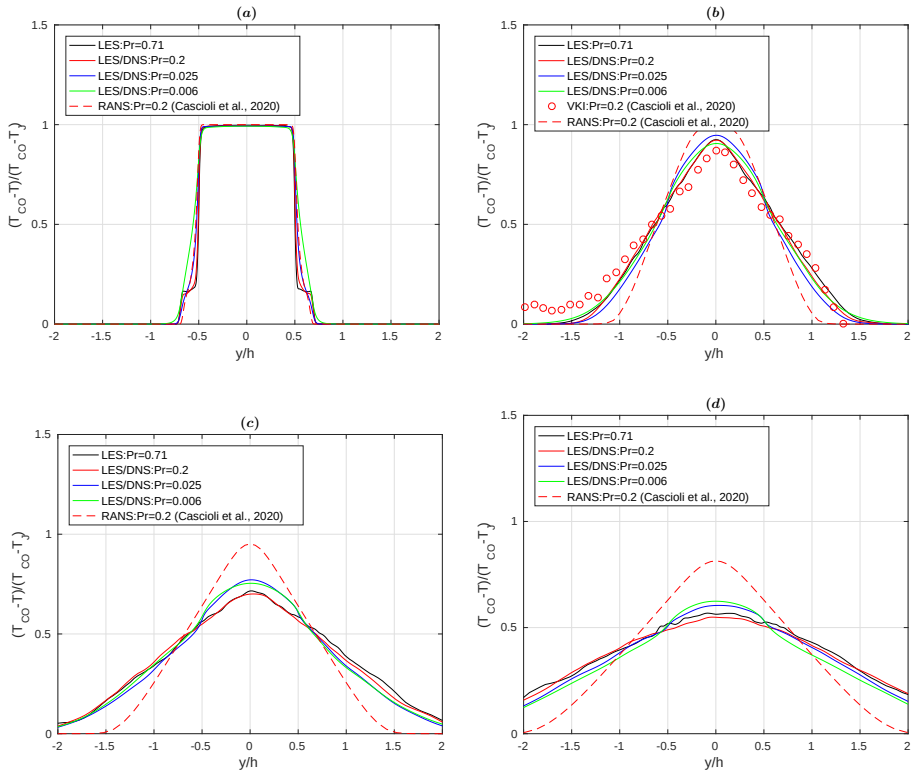

Figure 3.13: Profiles of resolved time-averaged temperature at x/h = 0 (a), 5 (b), 10 (c) and 15 (d).

The characteristic profiles of the non-dimensional temperature standard deviation are shown in Fig.3.14. Single peak distributions are obtained for the lowest value of Pr = 0.006 already at x/h = 5, while the double peak distributions are obtained for remaining Prandtl numbers up to x/h = 10 location. At the x/h = 15, the central jet values are identical for all simulated Prandtl numbers (obtained with the LES/DNS approach), whereas the RANS profile still exhibits the double peak distribution, confirming a weaker mixing.

The profiles of the resolved vertical turbulent heat flux profiles are shown in Fig.3.15. Farther away from the inlet location, a distribution with two characteristic peaks is obtained for all simulated Prandtl numbers. Also, a monotonically decreasing intensity of the turbulent heat flux proportional to the decrease in the Prandtl number is visible at x/h = 5 and 10, Figs.3.15(b) and (c). At the final x/h = 15 location, the values in the center of the jet are very similar, and relatively small differences are still present in the co-flow regions, Fig.3.15(d).

The profiles of the characteristic thermal time-scale ($\tau_\theta = \langle k_\theta \rangle / \langle \varepsilon_\theta \rangle$) are shown in Fig.3.16. At both locations (i.e. x/h = 5 and x/h = 10), profiles exhibit a gradual reduction in the co-

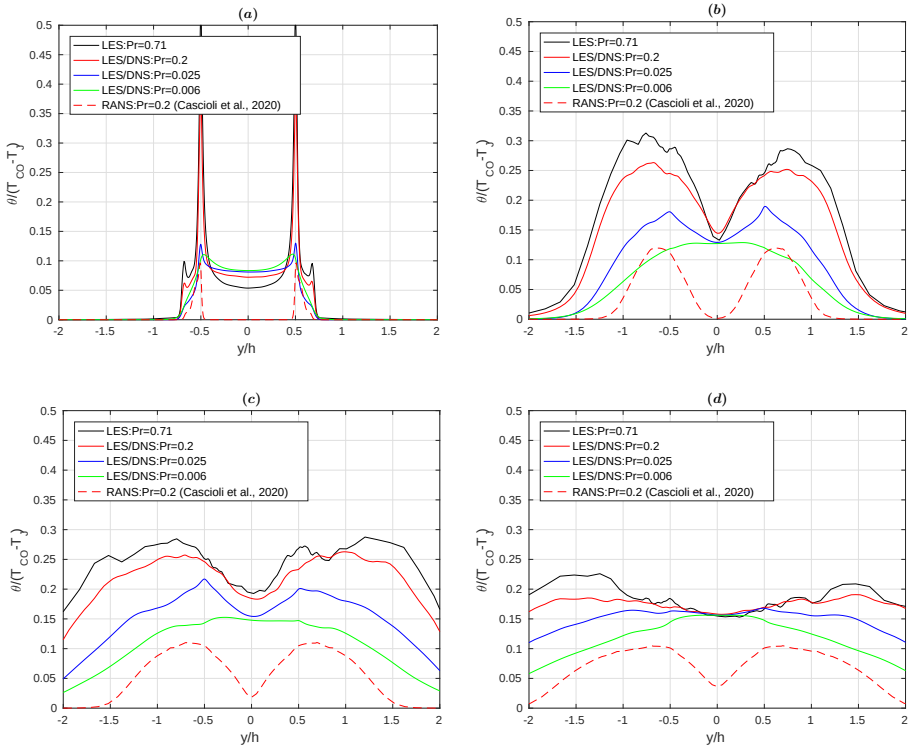

Figure 3.14: Profiles of the non-dimensional standard deviation of temperature at x/h = 0 (a), 5 (b), 10 (c) and 15 (d).

flow regions with the Prandtl number decrease. In contrast to this behavior, in the center of the jet, the values are initially suppressed, but for the lowest value of the Prandtl (Pr = 0.006), the peak value increased and is close to the result of the Pr = 0.71, Figs.3.16(a). At x/h = 10, variations in the time-scale are significantly reduced, and with characteristic dominant peak in the jet center for the for Pr = 0.006, Fig.3.16(b). This is a consequence of the single-peak behavior of the temperature variance (as previously shown in Fig.3.7(d)). For both locations, the profiles of the thermal time-scale obtained from the RANS model of [17] are also extracted for Pr = 0.2. It can be seen that a significant underprediction of the model is obtained for both locations, indicating a crucial point for its further improvement.

Finally, the profiles of the time-scale ratio (defined as $R = \tau_\theta/\tau_u$) are shown in Fig.3.17. It can be seen that relatively uniform distributions are obtained for LES at x/h = 5 location for Pr=0.71 and 0.2, Fig.3.17(a). For lower values of the Prandtl number (Pr = 0.025 and 0.006), at the same location, a non-uniform distribution with a distinct peak in the center of the jet is obtained. At x/h = 10 location, the LES distributions exhibit a non-uniform behavior for all considered values of Prandtl number, Fig.3.17(b). Again, for Pr=0.025 and 0.006, a distinct peak in the jet center is obtained. The RANS-based results of the time-scale ratio

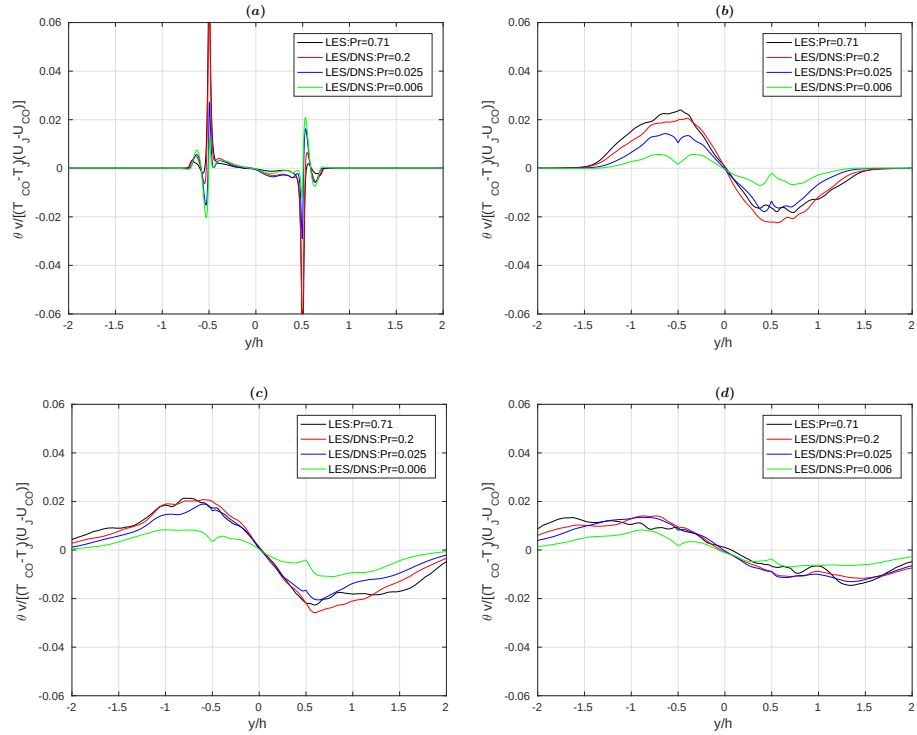

Figure 3.15: Profiles of resolved time-averaged turbulent heat fluxes at x/h = 0 (a), 5 (b), 10 (c) and 15 (d).

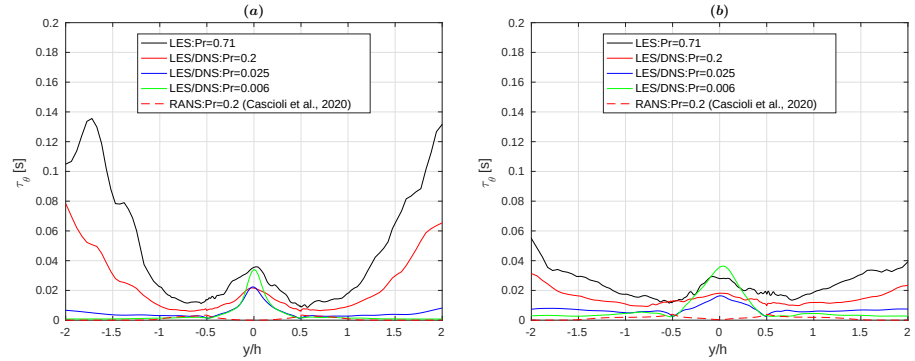

Figure 3.16: Profiles of resolved time-averaged thermal time-scale at at x/h = 5 (a) and 10 (b).

for Pr=0.2 exhibit characteristic two-peak behaviour at both locations, [17]. It can be seen that a large discrepancy is obtained in the jet centre and in the co-flow regions at x/h = 5 location, Fig.3.17(a). A double peak behavior shows values closer to the LES at x/h = 10,

but locations in the jet center and co-flow regions are still significantly underpredicted, Fig.3.17(a).

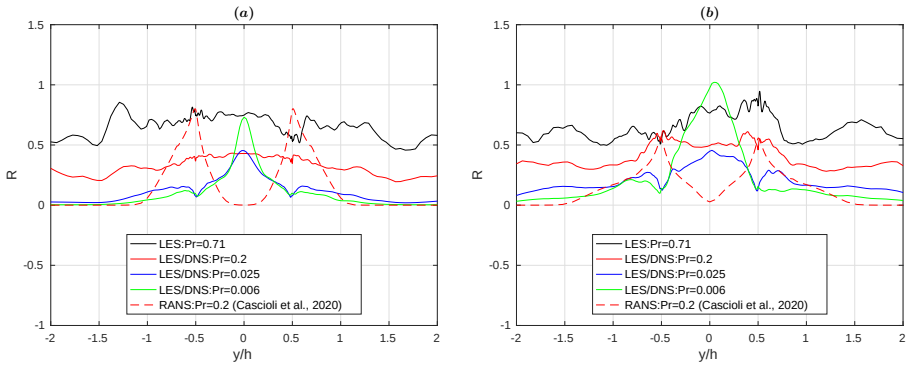

Figure 3.17: Profiles of resolved time-scale ratio ($R = \tau_\theta/\tau_u$) at at x/h = 5 (a) and 10 (b).

The streamwise evolution of the typical shear layer thickness in the central vertical plane is shown in Fig.3.18(a), demonstrating a good agreement between LES and RANS simulations. The profiles of the long-term time-averaged turbulent Prandtl number (calculated as $\mathrm{Pr_t} = \left(\overline{uv}dT/dy\right)/\left(\overline{\theta v}dU/dy\right)$) at $x/h = 10$ are shown in Fig.3.18(b). It can be seen that a constant value of $\mathrm{Pr_t}$ (usually assumed in two-equation $k-\varepsilon$ models) of $\mathrm{Pr_t} = 0.86$ is a reasonable approximation for Pr=0.71. In contrast, for lower values of molecular Prandtl number, $\mathrm{Pr_t}$ profiles exhibit non-uniform distributions with characteristic peaks at $y/h = -0.5$ where the resolved shear-stress reaches its maximum. For Pr=0.025, the $\mathrm{Pr_t} = 1$ is a reasonable approximation except already mentioned peaks at $y/h = -0.5$ with a maximum value of $\mathrm{Pr_t^{max}} = 3$. For the lowest value or Pr=0.006, there is no segment with a constant value and its peak value is approximately $\mathrm{Pr_t^{max}} = 10$. This additionally stresses importance of designing the RANS-closures to take into account this highly non-uniform behavior of Pr_t for low Prandtl fluids. It is interesting to observe that the six-equation RANS closure of [17] at Pr=0.2 agrees well with LES in the $-1 \le y/h \le 0$ region, whereas an overprediction is obtained in the co-flow region ($-2 \le y/h \le -1$).

3.4.4 Frequency-based power spectra

To collect time-series of fluctuating velocity and temperature, a dense network of monitoring points is introduced in the central vertical plane of the computational domain, as shown in Fig.3.1(b). For selected number of locations extracted along the jet centerline ($y/h = 0$) and along the edge of the initial central jet ($y/h = -1$), we performed a discrete Fourier transformation to get the characteristic power-spectral density, Figs.3.19 and 3.20. The fluctuating streamwise velocity spectra ($E_u(f) = \frac{1}{2}u'u'$, where $u' = \hat{U} - \langle\overline{U}\rangle$) is plotted in Fig.3.19. The spectra of the fluctuating streamwise velocity at monitoring points extracted along the jet centerline ($y/h = 0$ and x/h =2, 6 and 10) are shown in Fig.3.19(a). The presented spectra clearly indicate transitions between the energy-containing, convective-inertial, and viscous-dissipative ranges, [3]. It can be seen that for the frequencies up to

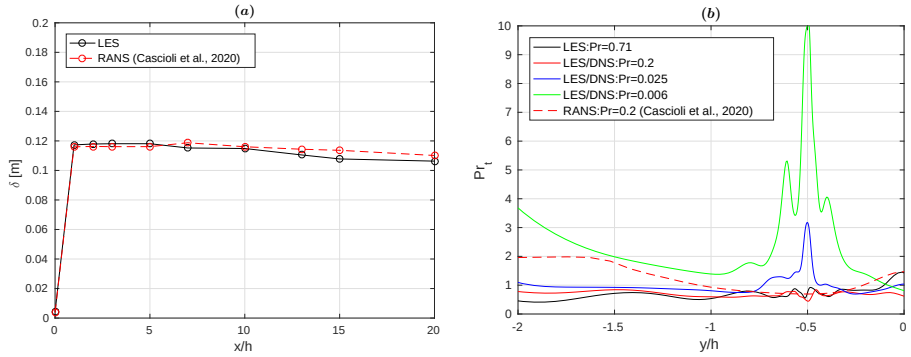

Figure 3.18: Distribution of the shear-layer thickness (δ) in the streamwise direction (a), and zoom-in profiles of the turbulent Prandtl number (Pr_t) at x/h = 10 for various values of Pr.

f = 1 kHz, there is a continuous increase in the amplitude (E_u) with increasing distance from the inlet. There is a relatively narrow inertial range ($E_u \propto f^{-5/3}$, [40] in $0.5 \leq f \leq 2 \times 10^3$ kHz), followed by a rapid dissipation range ($E_u \propto f^{-8}$ in $2 \leq f \leq 6$ kHz) at x/h = 6 and 10, and, finally, with a less steep decay up to f = 200 kHz. At the monitoring point closer to the inlet (x/h = 2), the rapid decay covers $2 \leq f \leq 7$ kHz range, followed with a milder decay range starting at f = 10 kHz and ending at f = 200 kHz.

The spectra of the monitoring points along the $y/h = -1$ line exhibit different behavior, Fig.3.19(b). Compared to the centerline points, a significantly larger inertial ($f^{-5/3}$) range can be observed. The inertial range starts at f = 200 Hz and extends up to f = 6 kHz for the x/h = 10 location. In contrast to the significantly extended inertial range, the rapid-decay (f^{-8}) range is significantly reduced. At the x/h = 6 location, it extends between f = 3 and 6 kHz, whereas at x/h = 10, this range is between $f = 5kHz$ and $7kHz$.

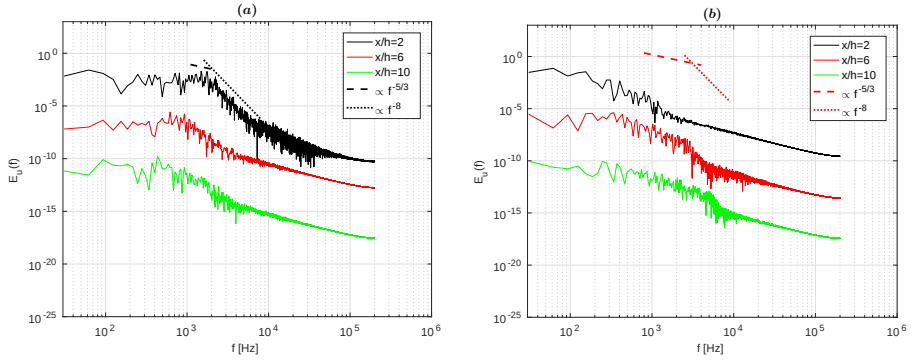

Figure 3.19: The power spectra of the streamwise velocity component at the following monitoring point locations: y/h = 0 (a) and -1 (b) and z/h = 0 - Note that, because of the readability purposes, the red and green profiles have been systematically shifted by dividing the original signals by factors 10^5 and 10^{10}, respectively.

In analysis of temperature fluctuations ($E_\theta(f) = \frac{1}{2}\theta'\theta'$, where $\theta' = \hat{T} - \langle\overline{T}\rangle$) spectra, we selected only the highest (Pr = 0.71) and lowest (Pr = 0.006) values of Prandtl number, Fig.3.20. For air (Pr = 0.71), at $x/h = 2$ and $y/h = 0$ (the jet centerline), distribution shows a close resemblance with the velocity spectra at the Fig.3.20(a). The similarity with the velocity is also obtained in the energy-dominant regime ($f \leq 1$ kHz) at locations $x/h = 6$ and 10. The differences are again noticeable in the viscous-dissipation regimes, where the behavior at $x/h = 6$ is now closer to the $x/h = 2$ than to $x/h = 10$. At the same locations, the temperature spectra for the Pr = 0.006 show similar behavior, but the amplitude E_θ is just shifted vertically to lower values, Fig.3.20(c). At the off-center locations, i.e. $y/h = -1$, the temperature spectra of both Pr = 0.71 and Pr = 0.006 show significantly different distributions compared to the velocity spectra, Figs.3.20(b) and (d). The amplitude E_θ now extends over a significantly larger range of almost ten decades at the off-center locations, but the maximum of the E_θ is significantly lower for Pr = 0.006.

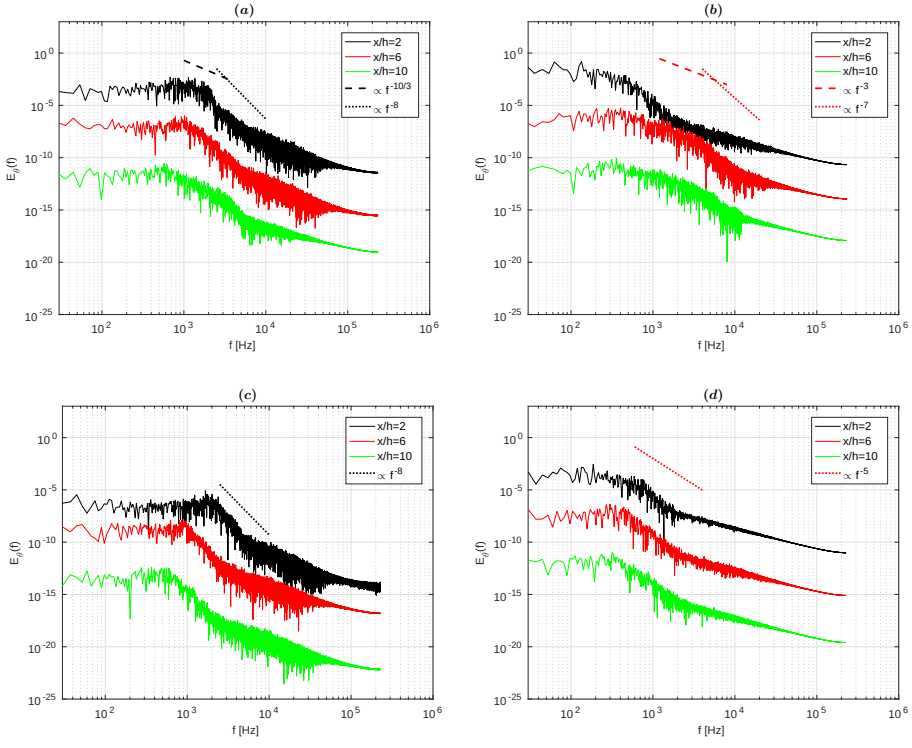

Figure 3.20: The power spectra of the temperature for Pr = 0.71 (a,b) and Pr = 0.006 (c,d) at the following monitoring point locations: y/h = 0 (a,c) and -1 (b,d) and z/h = 0 - Note that, because of readability purposes, the red and green profiles have been systematically shifted by dividing the original signals by factors 10^5 and 10^{10}, respectively.

3.5 Conclusions

We performed fully dynamic LES and combined dynamic LES/DNS simulations on the forced convection planar jet under similar conditions as in recent experiments in the MYRTE wind tunnel operated at VKI. To eliminate some of the design limitations of the experimental setup, which is resulting in asymmetrical inlet conditions, we impose precursor simulations of the central jet and co-flows such that the total flow rate is identical to the experiment. This approach proved to be numerically efficient and provided the fully developed turbulence in good agreement with DNS results from the literature. The obtained results were in good agreement with experiments regarding the mean velocity and temperature profiles. The current approach demonstrated significant improvement in predictions of the mean temperature profile in comparison to the four-equation RANS model, particularly with regards to the spanwise spreading of the jet. The mean temperature profiles demonstrated low sensitivity to changes of the Prandtl number. This is due to dominant mechanisms of convection and turbulent diffusion over molecular diffusion. Here presented results of the second-moments of the velocity and temperature fields can be used for detailed validation of the RANS-type models. Within the framework of the model validations, the here presented characteristic time-scale ratios and corresponding dissipation rates (mechanical and thermal) are important information not easily available from experiments. Finally, the power spectra at characteristic monitoring points revealed interesting local dissimilarities between the velocity and temperature fluctuations for selected values of Prandtl number.

References

[1] R. Fernandez, D. De Bruyn, P. Baeten, H. Aït Adberrahim, The evolution of the primary system design of the MYRRHA facility, IAEA-CN-245-258 2017.

[2] K. Van Tichelen, F. Mirelli, M. Greco, G. Viviani, E-SCAPE: A scale facility for liquid-metal, pool-type reactor thermal hydraulic investigations, Nuclear Engineering and Design 290 (2015) 65–77.

[3] S. B. Pope, Turbulent Flows., Cambridge University - Cambridge Univ. Press. 2000.

[4] G. Grötzbach, Challenges in low-Prandtl number heat transfer simulation and modelling, Nucl. Eng. Des. 264 (2013), 41–55.

[5] F. Roelofs, A. Shams, I. Otic, M. Böttcher, M. Duponcheel, Y. Bartosiewicz, D. Lakehal, E. Baglietto, S. Lardeau, X. Cheng, Status and perspective of turbulence heat transfer modelling for the industrial application of liquid metal flows, Nuclear Engineering and Design 290 (2015) 99–106.

[6] K. Abe, T. Kondoh, Y. Nagano, A new turbulence model for predicting fluid flow and heat transfer in separating and reattaching flows - II. Thermal calculations, International Journal of Heat and Mass Transfer 38 (8) (1995) 1467–1481.

[7] S. Kenjereš, K. Hanjalić, Convective rolls and heat transfer in finite-length Rayleigh–Bénard convection: a two-dimensional numerical study, Physical Review E 62 (6) (2000) 7987.

[8] R. Da Vià, S. Manservisi, F. Menghini, A $k-\Omega-k_\theta-\Omega_\theta$ four parameter logarithmic turbulence model for liquid metals, Nuclear Engineering and Design 101 (2016) 1030–1041.

[9] A. De Santis, A. Shams, Application of an algebraic turbulent heat flux model to a backward facing step flow at low Prandtl number, Annuals of Nuclear Energy 117 (2018) 32–44.

[10] A. De Santis, A. Villa Ortiz, A. Shams, L. Koloszar, Modelling of a planar impinging jet at unity, moderate and low Prandtl number: Assessment of advanced RANS closures, Annuals of Nuclear Energy 129 (2019) 125–145.

[11] C. Y. Li, S. V. Garimella, Prandtl-number effects and generalized correlations for confined and submerged jet impingement, International Journal of Heat and Mass Transfer 44 (2001) 3471–3480.

[12] B. Rembold, N. A. Adams, L. Kleiser, Direct numerical simulation of a transitional rectangular jet, International Journal of Heat and Fluid Flow 23 (5) (2002) 547–553.

[13] J. Oder, A. Shams, L. Cizelj, I. Tiselj, Direct numerical simulation of low-Prandtl fluid flow over a confined backward facing step, International Journal of Heat and Mass Transfer 142 (2019) 118436.

[14] A. Villa Ortiz, L. Koloszar and P. Planquart, Large Eddy Simulations on a natural convection boundary layer at Pr = 0.71 and 0.025, Nuclear Engineering and Design 353 (2019) 110231.

[15] U. Knebel, L. Krebs, U. Muller, B. P. Axcell, Experimental investigation of a confined heated sodium jet in a co-flow, Journal of Fluid Mechanics 368 (1998) 51–79.

[16] S. Buckingham, Prandtl number effects in abruptly separated flows: LES and experiments on an unconfined backward facing step flow, PhD Dissertation – Université Catholique de Louvain 2018.

[17] E. Cascioli, S. Buckingham, S. Keijers, K. Van Tichelen, S. Kenjereš, Numerical and experimental analysis of a planar jet with heated co-flow at medium and low Prandtl-number values, Nuclear Engineering and Design 361 (2020) 110570, 1–11.

[18] I. Di Venuta, A. Boghi, M. Angelino, F. Gori, Passive scalar diffusion in three-dimensional turbulent rectangular free jets with numerical evaluation of turbulent Prandtl/Schmidt number, International Communications in Heat and Mass Transfer 95 (2018) 106–115.

[19] N. Kimura, H. Miyakoshi, H. Kamide, Experimental investigation on transfer characteristics of temperature fluctuation from liquid sodium to wall in parallel triple-jet, International Journal of Heat and Mass Transfer 50 (2007) 2024–2036.

[20] A. Fregni, D. Angeli, A. Cimarelli, E. Stalio, Direct Numerical Simulation of a buoyant triple jet at low-Prandtl number, International Journal of Heat and Mass Transfer 143 (2019) 118466.

[21] M. Germano, U. Piomelli, P. Moin, W. H. Cabot, A dynamic subgrid-scale eddy viscosity model, Physics of Fluids A 3 (1991) 1760–1765.

[22] J. Smagorinsky, General circulation experiments with the primitive equations. I. The basic experiment, Monthly Weather Review 91 (1963) 99–164.

[23] D. K. Lilly, A proposed modification of the Germano subgrid-scale turbulence closure method, Physics of Fluids A 4 (1992) 633–635.

[24] B. W. Righolt, S. Kenjereš, R. Kalter, M. J. Tummers, C. R. Kleijn, Dynamics of an oscillating turbulent jet in a confined cavity, Physics of Fluids **27**, 095107 (2015) 1–16.

[25] B. W. Righolt, S. Kenjereš, R. Kalter, M. J. Tummers, C. R. Kleijn, Electromagnetic control of an oscillating turbulent jet in a confined cavity, Int. J. Heat and Fluid Flow (62), part B (2016) 395–406.

[26] S. Kuhn, S. Kenjereš, P. Rudolf von Rohr, Large-eddy simulations of wall heat transfer and coherent structures in mixed convection over a wavy wall, Int. J. Therm. Sci. 49 (2009), 1209–1226.

[27] C. Wagner, S. Kenjereš, P. Rudolf von Rohr, Dynamic large eddy simulation of momentum and wall heat transfer in forced convection over wavy surfaces, Journal of Turbulence 12 (7), (2010) 1–27.

[28] P. Moin, K. Squires, W. Cabot, S. Lee, A dynamic subgridscale model for compressible turbulence and scalar transport, Physics of Fluids 3 (1991) 2746.

[29] D. Morar, Subgrid-scale heat flux modeling for large eddy simulation of turbulent mixed convection, PhD Dissertation – Karlsruhe Institute of Technology 2014.

[30] J. E. Vesper, Large Eddy Simulation of Heat Transfer Processes in Energy Systems based on Thermodynamically Consistent Models, MSc Dissertation – Darmstadt University of Technology 2017.

[31] R. I. Issa, A. D. Gosman, A. P. Watkins, The computation of compressible and incompressible recirculating flows by a non-iterative implicit scheme, Journal of Computational Physics 62 (1986) 66–82.

[32] H. K. Versteeg, W. Malalasekera, An introduction to computational fluid dynamics - The finite volume method, Longman Scientific & Technical 1995.

[33] A. Smirnov, S. Shi, I. Celik, Random flow generation technique for large eddy simulations and particle dynamics modeling, Journal of Fluids Engineering 123 (2001) 359–371.

[34] S. K. Robinson, Coherent motions in the turbulent boundary layer, Annual Review of Fluid Mechanics 23 (1991) 601–639.

[35] U. Piomelli, E. Balaras, Wall-layer models for large-eddy simulations, Annual Review of Fluid Mechanics 34 (2002) 349–374.

[36] R. W. Davis, E. F. Moore, A numerical study of vortex shedding from rectangles, Journal of Fluid Mechanics 116 (1982) 475–506.

[37] D. J. Price, Modelling discontinuities and Kelvin–Helmholtz instabilities in SPH, Journal of Computational Physics 227 (2008) 10040–10057.

[38] G. Ruiz-Chavarria, C. Baudet, S. Ciliberto, Scaling laws and dissipation scale of a passive scalar in fully developed turbulence, Physica D 99 (1996) 396–380.

[39] R. D. Moser, J. Kim, N. N. Mansour, Direct numerical simulation of turbulent channel flow up to $\mathrm{Re}_\tau = 590$, Physics of fluids 11 (4) (1999) 943–945.

[40] G. K. Batchelor, Small-scale variation of convected quantities like temperature in turbulent fluid Part 1. General discussion and the case of small conductivity, Journal of Fluid Mechanics 5 (1) (1959) 113–133.

4

Numerical analysis of a parallel triple-jet of liquid-sodium in a turbulent forced convection regime

In the present study, we have applied a combined wall-resolving dynamic Large-Eddy Simulation (LES) (for the velocity field) and Direct Numerical Simulation (DNS) (for the temperature field) approach for mixing of parallel triple-jets with different temperatures of liquid sodium in a turbulent forced convection regime. The liquid sodium as primary coolant is considered in the design of advanced fast nuclear reactors, especially from a perspective of currently ongoing developments of the small modular reactor technology. Because of the high thermal conductivity of sodium (i.e. it belongs to the low-Prandtl fluids), we adopted the dynamic Smagorinsky subgrid closure for the unresolved velocity scales, while the thermal scales are fully resolved. Furthermore, the Transient-Reynolds-Averaged Navier-Stokes (T-RANS) approach with the high-Reynolds number variant (i.e. with the wall functions as boundary conditions along solid boundaries) of the four-equation eddy viscosity model ($k-\varepsilon-k_\theta-\varepsilon_\theta$) was applied. Both combined dynamic LES/DNS (with two different mesh levels) and T-RANS approach were compared with available experimental data from the literature. The fine-mesh LES/DNS provided a close agreement with the experimental data for both velocity and temperature fields (for both first- and second-moments). In contrast, the coarse-mesh LES/DNS overestimated the turbulent kinetic energy profiles at different distances from the inlet plane. The T-RANS results confirmed a good agreement with the mean streamwise velocity and turbulent kinetic energy, as well as the mean temperature profiles. The temperature variance profiles from T-RANS were overestimated indicating the necessity of further refinement and validation of the modeled equation for the dissipation rate of temperature variance. Finally, the analysis of the power spectra density distributions of the temperature signal revealed that all simulations techniques captured a dominant flow frequency originating from the induced

This chapter is fully based on the scientific publication:
***E. Cascioli**, B. Kaaks, S. Keijers, K. Van Tichelen, S. Kenjereš, Numerical Analysis of a Parallel Triple-Jet of Liquid-Sodium in a Turbulent Forced Convection Regime, International Communications in Heat and Mass Transfer (2023 - Under Review).*

Kelvin-Helmholtz instabilities between the side and central jets. Interestingly, the T-RANS captured two dominant frequencies in good agreement with the experiment, even for the very short time length intervals, but was not able to capture the dissipative range of the spectra, while the coarse-mesh and fine-mesh LES/DNS captured a single dominant frequency, due to a simplified model of the inlet nozzles. Here, presented combined dynamic LES/DNS approach is recommended for future simulations of the turbulent forced convection flows of low Prandtl fluids especially if thermal fatigue effects need to be predicted correctly.

4.1 Introduction

During the last decade, we have witnessed a renovated interest in liquid metal-cooled fast nuclear reactors in the market, particularly with regards to the small modular reactor technology, [1] [2]. Moreover, other projects on advanced pool-type reactors cooled by liquid metals were already launched, such as the Multi-Purpose hYbrid Research Reactor for High-tech Applications (MYRRHA) by the Belgian Nuclear Research Center (SCK CEN), [3]. For example, considering the MYRRHA reactor, we can recognize that turbulent mixing phenomena also occur in quasi-unconfined regions, namely the upper and lower plena. As well as for the wall-confined flows, it is still important to properly understand the thermal hydraulics phenomena to reliably predict velocity and temperature fields. For this purpose, Computational Fluid Dynamics (CFD) is extensively used to support both safety analysis and design process, as well as for the prediction, control and optimization of the normal and accidental operational conditions. Concerning the present study, two challenges are identified. Firstly, the Turbulent Heat Transfer (THT) modeling for liquid metals imposes a re-evaluation of the Reynolds analogy, which is normally employed in the case of Reynolds Averaged Navier-Stokes (RANS) simulations when the Prandtl number (Pr) of the fluid is close the unity. It is known that such standard approach cannot effectively be applied in case of liquid metals, where $\mathrm{Pr} \ll 1$, [4]. For the THT of such low-Pr fluids, more advanced models have been proposed, with particular reference to wall-confined configurations in terms of development and validation, [5] [6]. We have observed an early modeling approach, which consisted of turbulent Prandtl number (Pr_t) correlations, such as the one proposed by [7]. There was still the need of more advanced models, and four-equation models were presented and widely employed within the nuclear community, i.e. the $k-\varepsilon-k_\theta-\epsilon_\theta$ model. At higher level, departing from the geometry-dependency and calibration optimization, algebraic heat flux THT models have been proposed and improved too. As mentioned, the test cases for such advanced THT models were mainly channel and pipe flows, backward-facing step and impinging jet flows, [8] [9] [10]. Then, the turbulent mixing in larger regions of reactor cannot be represented by any wall-confined flow configurations, while jets are identified as fundamental test case to be investigated. The experimental and numerical database on turbulent jet flows with low-Pr fluids is more limited in literature, as well as the related testing and development of low-Pr THT models: in this frame, our study is set and aims to contribute to both high-fidelity numerical database generation and testing of four-equation low-Pr model on a turbulent low-Pr non-isothermal triple-jet flow. We have recently studied a single-jet configuration with different low-Prandtl fluids, also providing a new set of experimental and numerical databases, [11] [12], but here we aim to analyze a more complex configuration. Therefore, we are now considering the PLAner triple parallel JEts Sodium experimenT

(PLAJEST) with sodium (Pr=0.006) of the Japanese Atomic Energy Agency (JAEA), which was experimentally studied by [13] [14]. This configuration is characterized by a cold central jet and two hot side jets, which could be seen as a representative mixing condition within the upper plenum of the reactor. For this test case, we found few numerical studies in literature only. A relatively coarse Large-Eddy Simulation (LES) approach ($5{\cdot}10^6$ tetrahedral unstructured elements within the fluid domain) was performed by [15], where the SubGrid-Scale (SGS) model was the Wall Adapting Local Eddy-viscosity (WALE) of [16]. The standard wall function was imposed along the different walls. The obtained results were in good agreement with the experiments. More recently, [17] performed a systematic sensitivity analysis of various SGS closures, numerical mesh resolution, and numerical schemes, mostly focusing on the velocity field of the PLAJEST experiment. It was found that the WALE subgrid closure performed better than the standard Smagorinsky, which was slightly too diffusive - especially on the too-coarse numerical mesh. Further numerical studies on even finer numerical mesh were recommended to obtain a better distinction between the numerical viscosity and subgrid-scale contributions. We here present the results of combined dynamic LES for the momentum field and Direct Numerical Simulation (DNS) for the thermal transport, which can represent a complete and reliable numerical database for the PLAJEST test case. We also performed additional Transient-RANS (T-RANS) simulations employing the four-equation ($k-\varepsilon-k_\theta-\varepsilon_\theta$) model, which does not require a priori specification of Pr_t. The rationale behind the T-RANS approach is in its significantly less intensive computational requirements in comparison to LES, both in terms of the requested numerical mesh size as well as in terms of the time integration (larger time steps and a shorter time-averaging procedure), [18] [19] [20]. In addition to instantaneous fields and averaged first- and second-order statistics, we performed Power Spectra Density (PSD) analyses to assess the potential of T-RANS simulations in capturing dominant frequency peaks and dissipation regimes. In fact, the correct prediction of this information plays a crucial role to prevent and properly design the system against mechanical failure of the wall materials subject to thermal fatigue (thermal striping), [21].

4.2 Numerical method

4.2.1 Governing equations

The fundamental conservation of mass, momentum, and energy can be described by the following equations:

$$\frac{\partial \hat{U}_i}{\partial x_i} = 0 \tag{4.1}$$

$$\frac{\partial \hat{U}_i}{\partial t} + \frac{\partial \hat{U}_i \hat{U}_j}{\partial x_j} = -\frac{1}{\rho}\frac{\partial \hat{p}}{\partial x_i} + \nu \frac{\partial^2 \hat{U}_i}{\partial {x_j}^2} \tag{4.2}$$

$$\frac{\partial \hat{T}}{\partial t} + \frac{\partial \hat{U}_j \hat{T}}{\partial x_j} = \alpha \frac{\partial^2 \hat{T}}{\partial {x_j}^2} \tag{4.3}$$

where ρ, ν and α are the molecular density, kinematic viscosity, and thermal diffusion, respectively. These are kept as constants in this study.

For the LES technique, we set the spatial filter (denoted as '$\overline{\cdot}$' and relates to cell size '$\overline{\Delta}$'), leading to the filtered momentum equation:

$$\frac{\partial \overline{U_i}}{\partial t} + \frac{\partial \overline{U_i}\,\overline{U_j}}{\partial x_j} = -\frac{1}{\rho}\frac{\partial \overline{p}}{\partial x_i} - \frac{\partial \tau_{ij}}{\partial x_j} + \nu \frac{\partial^2 \overline{U_i}}{\partial {x_j}^2} \tag{4.4}$$

where τ_{ij} is the SGS turbulent stress, which can be further indicated as:

$$\tau_{ij} = \overline{U_i U_j} - \overline{U_i}\,\overline{U_j} \tag{4.5}$$

and needs to be modeled, [22].

Dealing with a low-Prandtl fluid, and in analogy with [12], we use a combined LES/DNS technique, which consists of the LES approach for the momentum transport (Eq.(4.4)) and DNS approach (full resolution) for the heat transport (Eq.(4.3)).

4

4.2.2 Dynamic subgrid-scale Smagorinsky model

The dynamic Smagorinsky SGS model allows the local calculation of the model coefficients, which are thus not fixed *a priori*, [23]. This aims to improve the standard Smagorinsky SGS model, where a single and constant value of the Smagorinsky constant is set for all the fluid domain, [24]. A test grid (denoted with '$\widetilde{\cdot}$') is defined with a width of $\widetilde{\overline{\Delta}} = 2\overline{\Delta}$. The subtest-tensor ($T_{ij}$) is then achieved as:

$$T_{ij} = \widetilde{\overline{U_i U_j}} - \widetilde{\overline{U_i}}\,\widetilde{\overline{U_j}} \tag{4.6}$$

It is shown in [23] that resolved stress can be expressed as:

$$L_{ij} = T_{ij} - \widetilde{\tau_{ij}} \tag{4.7}$$

and it can be explicitly evaluated from the large-scales as:

$$L_{ij} = \widetilde{\overline{U_i}\,\overline{U_j}} - \widetilde{\overline{U_i}}\,\widetilde{\overline{U_j}} \tag{4.8}$$

The same closure of the Smagorinsky model is applied for both the grid-filter and test-filter turbulent stress with an identical value of the model coefficient C_s, and it can be written as:

$$\tau_{ij} - \frac{1}{3}\delta_{ij}\tau_{kk} = -2C_s\overline{\Delta}^2\,\overline{|S|S_{ij}} \tag{4.9}$$

$$T_{ij} - \frac{1}{3}\delta_{ij}T_{kk} = -2C_s\widetilde{\overline{\Delta}}^2\,\widetilde{\overline{|S|}}\,\widetilde{\overline{S_{ij}}} \tag{4.10}$$

where C_s is the dynamic Smagorinsky constant (to be calculated overtime), while $\overline{S_{ij}} = \frac{1}{2}\left(\frac{\partial \overline{U_i}}{\partial x_j} + \frac{\partial \overline{U_j}}{\partial x_i}\right)$ and $\widetilde{\overline{S_{ij}}} = \frac{1}{2}\left(\frac{\partial \widetilde{\overline{U_i}}}{\partial x_j} + \frac{\partial \widetilde{\overline{U_j}}}{\partial x_i}\right)$ are the strain rate tensors calculated over the grid-filter $\overline{\Delta}$ and test-filter $\widetilde{\overline{\Delta}}$, respectively.

Considering the Eqs.(4.8), (4.9) and (4.10), we achieve:

$$L_{ij} - \frac{1}{3}\delta_{ij}L_{kk} = 2C_s M_{ij} \tag{4.11}$$

where:

$$M_{ij} = \widetilde{\overline{\Delta}^2}\,\tilde{\overline{|S|}}\,\widetilde{\overline{S_{ij}}} - \overline{\Delta}^2\,\widetilde{\overline{|S|}\,\overline{S_{ij}}} \tag{4.12}$$

Particularly, we consider an adapted version of the original dynamic approach, as developed by [25], where a least squares method is applied to optimize the C_s value as:

$$\left(e_{ij}\right)^2 = \left(L_{ij} - \frac{1}{3}\delta_{ij}L_{kk} - 2C_s M_{ij}\right)^2 \tag{4.13}$$

The turbulent SGS viscosity can be finally defined as:

$$\nu_{SGS} = C_s\overline{\Delta}^2\,\overline{|S|} \tag{4.14}$$

to close of the filtered momentum equation. In analogy with [12], we locally average C_s within the six "neighbor" cells, and bind the turbulent SGS viscosity ($\nu_{SGS} \geq -\nu$), to allow some backscattering, [26] [27].

4.2.3 T-RANS simulation

The unsteady T-RANS simulations were run considering constant-value fluid properties and eddy-viscosity and -diffusivity assumptions. The Reynolds-averaged transport equations are:

$$\frac{\partial U_i}{\partial t} + U_j\frac{\partial U_i}{\partial x_j} = -\frac{1}{\rho}\frac{\partial p}{\partial x_i} + \frac{\partial}{\partial x_j}\left[(\nu + \nu_t)\frac{\partial U_i}{\partial x_j}\right] \tag{4.15}$$

$$\frac{\partial T}{\partial t} + U_j\frac{\partial T}{\partial x_j} = \frac{\partial}{\partial x_j}\left[(\alpha + \alpha_t)\frac{\partial T}{\partial x_j}\right] \tag{4.16}$$

where ν_t is the eddy viscosity and α_t is the turbulent thermal diffusivity, to be modeled. In analogy to [11], a four equation model $k-\varepsilon-k_\theta-\varepsilon_\theta$ is here employed, though not in its low-Reynolds variant. The original low-Reynolds modeling was introduced and further developed by [28] [29] [30]. The transport equations are:

$$\frac{\partial k}{\partial t} + U_j\frac{\partial k}{\partial x_j} = P_k - \varepsilon + \frac{\partial}{\partial x_j}\left[\left(\nu + \frac{\nu_t}{\sigma_k}\right)\frac{\partial k}{\partial x_j}\right] \tag{4.17}$$

$$\frac{\partial \varepsilon}{\partial t} + U_j\frac{\partial \varepsilon}{\partial x_j} = (C_{\varepsilon_1}P_k - C_{\varepsilon_2}\varepsilon)\frac{\varepsilon}{k} + \frac{\partial}{\partial x_j}\left[\left(\nu + \frac{\nu_t}{\sigma_\varepsilon}\right)\frac{\partial \varepsilon}{\partial x_j}\right] \tag{4.18}$$

$$\frac{\partial k_\theta}{\partial t} + U_j\frac{\partial k_\theta}{\partial x_j} = \frac{\partial}{\partial x_j}\left[\left(\alpha + \frac{\alpha_t}{\sigma_{k_\theta}}\right)\frac{\partial k_\theta}{\partial x_j}\right] + P_\theta - \varepsilon_\theta \tag{4.19}$$

$$\frac{\partial \varepsilon_\theta}{\partial t} + U_j \frac{\partial \varepsilon_\theta}{\partial x_j} = \frac{\partial}{\partial x_j}\left[\left(\alpha + \frac{\alpha_t}{\sigma_{\varepsilon_\theta}}\right)\frac{\varepsilon_\theta}{\partial x_j}\right] + \frac{\varepsilon_\theta}{k_\theta}\left(C_{p_1} P_\theta - C_{d_1}\varepsilon_\theta\right) + \frac{\varepsilon_\theta}{k}\left(C_{p_2} P_k - C_{d_2}\varepsilon\right) \tag{4.20}$$

where $P_k = \left[\nu_t\left(\frac{\partial U_i}{\partial x_j} + \frac{\partial U_j}{\partial x_i}\right) - \frac{2}{3}\delta_{ij}k\right]\frac{\partial U_i}{\partial x_j}$ and $P_\theta = \alpha_\theta\left(\frac{\partial T}{\partial x_j}\right)\left(\frac{\partial T}{\partial x_j}\right)$ represent the modeled productions of turbulent kinetic energy and thermal fluctuations.

The eddy viscosity and thermal diffusivity can be defined as:

$$\nu_t = C_\mu \frac{k^2}{\varepsilon} \tag{4.21}$$

$$\alpha_t = C_\theta \frac{k^2}{\varepsilon}\frac{2R}{R+0.5} \tag{4.22}$$

where $R = \frac{\tau_\theta}{\tau_u} = \left(\frac{k_\theta}{\varepsilon_\theta}\right)/\left(\frac{k}{\varepsilon}\right)$ is the thermal to dynamical time scale ratio. All the model coefficients are collected in Table 4.1, [31], and Table 4.2, [30]. Note that no additional re-calibration of such model coefficients is being performed in the present study. The standard wall functions were used for the turbulence quantities along the no-slip walls.

Table 4.1: Model coefficients of the $k-\varepsilon$ turbulence model.

C_μ	C_{ε_1}	C_{ε_2}	σ_k	σ_ε
0.09	1.44	1.92	1	1.3

Table 4.2: Model coefficients of the $k_\theta - \varepsilon_\theta$ heat transfer model.

C_θ	C_{p_1}	C_{p_2}	C_{d_1}	C_{d_2}	σ_{k_θ}	$\sigma_{\varepsilon_\theta}$
0.1	0.925	0.9	1	0.9	1.4	1.4

4.2.4 Computational code

Both the LES/DNS and T-RANS simulations are performed by using the OpenFOAM CFD code (version 2.4.0). The dynamic Smagorinsky SGS model and ($k_\theta - \epsilon_\theta$) THT model were coded as additional libraries. To combine the velocity and pressure fields, the PISO algorithm was selected, [32].

For the LES/DNS, the gradient, Laplacian, and divergence terms were discretized by using second-order Central-Differencing Schemes (CDSs), while the second-order backward (implicit) scheme was used to integrate the time derivative term. The Courant number was kept below the value of 1.2, with an average value lower than the unity.

In the case of T-RANS simulations, the cell-limited CDSs were used for the gradient and Laplacian terms, while second-order upwind schemes were used to discretize the divergence terms.

4.3 Computational details

4.3.1 Computational domain

The PLAJEST triple-jet experimental setup (a) and details of the inlet nozzles (b), are shown in Fig.4.1, [13] [14] [33]. This triple-jet configuration consists of three parallel jets in a closed environment. The two side jets are characterized by the heated fluid at T_H = 620.7 K, while the central cold jet has an inlet temperature of T_C = 577.5 K. As mentioned, sodium is the working fluid (Pr = 0.006), with a constant molecular kinematic viscosity of ν = $3.73{\cdot}10^{-7}$ m^2/s. Each nozzle has the same height, h = 0.02 m, and this gives the Reynolds number of Re=27300. All other thermo-physical properties of the fluid are assumed as constants. Gravity effects are being neglected considering the forced convection regime, with a Richardson number of Ri = $8.72 \cdot 10^{-3}$.

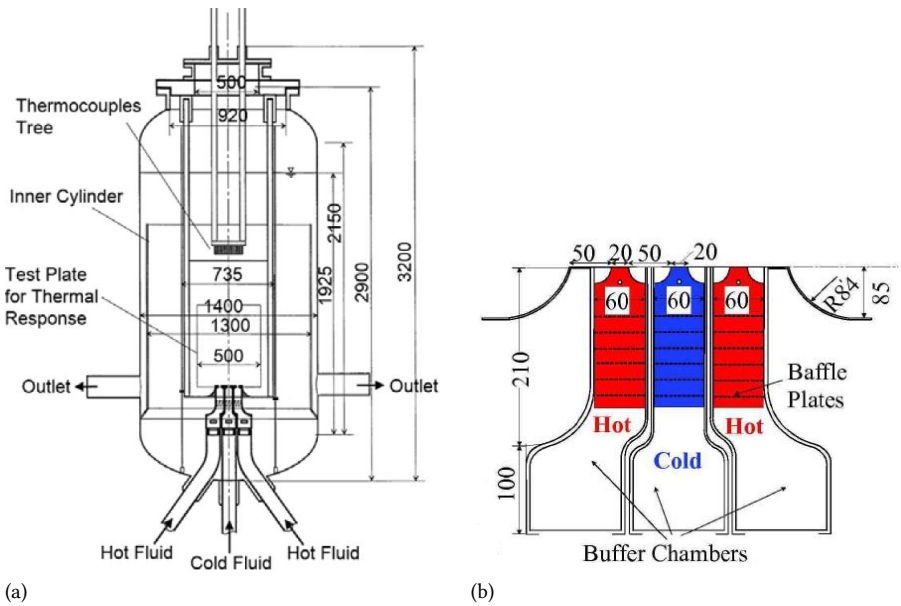

Figure 4.1: Sketch of the experimental setup (a) and details of the inlet plane and nozzles (b), [13] [14].

We developed two three-dimensional computational domains, Fig.4.2. The LES/DNS simulations were performed on a simplified computational domain (three 0.5h-long straight inlet channels), Fig.4.2-left (domain A), whereas the T-RANS simulation domain also included realistic inlet nozzles, Fig.4.2-right (domain B). The simplified domain (A) ensures a high mesh quality and affordable computational costs for the LES/DNS simulations. The numerical resolution in the spanwise direction (Δz^+) is important to achieve reliable performances when the periodic boundary conditions are projected at the simplified inlet planes for the LES/DNS simulations, [12]. Both domains are 5h-wide in the spanwise direction. In both cases, despite the vertical orientation of the experimental facility, the coordinate system in our simulations was oriented with U, V, and W representing the velocity components in streamwise (x), crosswise (y) and spanwise (z) directions, respec-

tively. The origin of the coordinate system (x = 0) is set at the interface between the central jet nozzle and mixing domain.

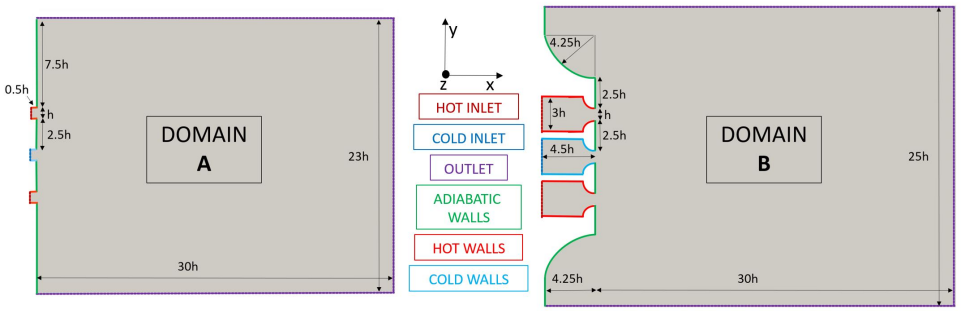

Figure 4.2: Sketch of the computational domain A for the LES/DNSs and domain B for the T-RANS simulation. Note that the various boundary conditions are indicated with different colors.

4.3.2 Domain A - LES/DNS

For the LES/DNS simulations, domain A was imposed and two numerical resolutions are generated. The coarse numerical mesh (denoted as 'c-LES') contains about 2 million control volumes in the mixing region, whereas the fine numerical mesh (denoted as 'f-LES') reaches 16 million control volumes. Details of both numerical meshes in the mixing region are given in Table 4.3.

Table 4.3: Mesh details of the mixing region (no inlet channels).

Case	Domain	Millions of cells	N_x x N_y x N_z	l_x x l_y x l_z [mm]
c-LES	A	2.0	240 x 166 x 50	2.5 x 2.8 x 2.0
f-LES	A	15.9	480 x 332 x 100	1.3 x 1.4 x 1.0
T-RANS	B	1.2	306 x 362 x 11	2.0 x 1.4 x 9.1

The mesh for the inlet channels is optimized to ensure $y^+ < 1$. The maximum aspect ratio of 5.1 was imposed for both meshes. The initial velocity was set to zero, while the initial temperature was specified as an average between hot and cold jet temperature weighted with the corresponding mass flows. At the inlet patches of the channels, a uniform velocity (U_J) was set to (0.51, 0, 0) m/s. The no-slip velocity boundary condition was set at all walls, whereas the T_H and T_C values were set along the hot and cold channel walls, respectively. The walls between the nozzles are adiabatic. The pressure zero-gradient condition is imposed at the inlet patches and at the walls. Three openings (top, bottom, and end) are set in the mixing domain as outlet patches, with modified zero-gradient[1] boundary condition for velocity. Here, the total pressure was calculated as $p_{out} = P_0 - \frac{1}{2}|U_{out}^2|$, where P_0 is the constant-value static pressure. Temperature was set to zero-gradient at the outlet instead. Regarding all the spanwise-normal surfaces, the cyclic boundary conditions were applied.

[1]It applies a zero-gradient condition to the flux out of the domain and calculates the inflow velocity based on a patch-normal flux.

4.3.3 Domain B - T-RANS

The domain B was developed for the T-RANS simulation and mainly differs from domain A by the inlet channel modeling. The inlet channels are about 4.5h-long and 3h-high (before narrowing). Consequently, an inlet velocity (U_{in}) of (0.17, 0, 0) m/s was set at the inlet patches, in order to reach the same Reynolds number at the nozzle section as for the case of domain A. The minimum wall unit-value along these channels is $y^+ = 12$. To represent the rounded sides of the experimental entrainment section, but to avoid the mesh singularities at the top and bottom corners of the mixing region, the domain B is slightly vertically extended (by 2h) in comparison to domain A. The final numerical mesh was characterized by a maximum cell aspect ratio of 24.3, maximum cell non-orthogonality of 51.1 (particularly in the rounded corner regions), and maximum skewness of 0.61. The total (including inlet and mixing regions) number of control volumes is about 1.4 million, where additional details of the numerical mesh are given in Table 4.3. The initial and boundary conditions for velocity and temperature are analogous to those of domain A. Additional initial and boundary conditions need to be specified for turbulence quantities of the four-equation ($k-\varepsilon-k_\theta-\varepsilon_\theta$) model. For all turbulence variables, a zero-gradient boundary condition is imposed at the outlets, whereas the symmetry boundary condition is imposed for the front and back of the simulation domain (i.e. in the z-coordinate direction). At the inlet, the turbulence intensity (I_t) of 10% was identified after a parametric study (on a two-dimensional configuration) to achieve the optimal value and get a good agreement with the experimental data. Then, the inlet turbulence kinetic energy and its dissipation rate were calculated as: $k = \frac{3}{2}(U_{in}I_t)^2$ and $\varepsilon = C_\mu{}^{3/4}\frac{k^{3/2}}{0.07H}$, with $H = 3h$. The inlet thermal variance and its dissipation rate were both specified as $k_\theta = \epsilon_\theta = 0$. Along the walls, the wall functions were imposed for the turbulence kinetic energy and its dissipation rate. For the thermal field turbulence, the following conditions were imposed: $k_\theta^{wall} = 0$ and $\varepsilon_\theta^{wall} = 2\alpha\left(\frac{k_\theta}{\Delta y_n^2}\right)_{(wall-1)}$, where Δy_n is the distance between the wall and the nearest cell center.

Characteristic length scales for LES/DNS

To ensure the appropriate resolution of the computational mesh, the characteristic Kolmogorov and Corrsin length scales are estimated, [34], as:

$$\eta = \left(\frac{\nu^3}{\epsilon}\right)^{\frac{1}{4}}, \quad \eta_\theta = \eta\,\mathrm{Pr}^{-\frac{3}{4}} \tag{4.23}$$

The dissipation rate was calculated and averaged ($\langle ... \rangle$) in runtime as:

$$\epsilon = \nu\left\langle\left(\frac{\partial u_i'}{\partial x_j}\right)^2\right\rangle \tag{4.24}$$

with $u_i' = \hat{U}_i - \langle U_i \rangle$.

In analogy to [12], a qualitative assessment of the mesh resolution can be performed by plotting the ratios between the characteristic cell length ($l_c = \left(\Delta_{\mathrm{CV}}\right)^{1/3} = \left(\Delta x \cdot \Delta y \cdot \Delta z\right)^{1/3}$) over η and η_θ, as shown by Fig.4.3 concerning the coarser LES/DNS.

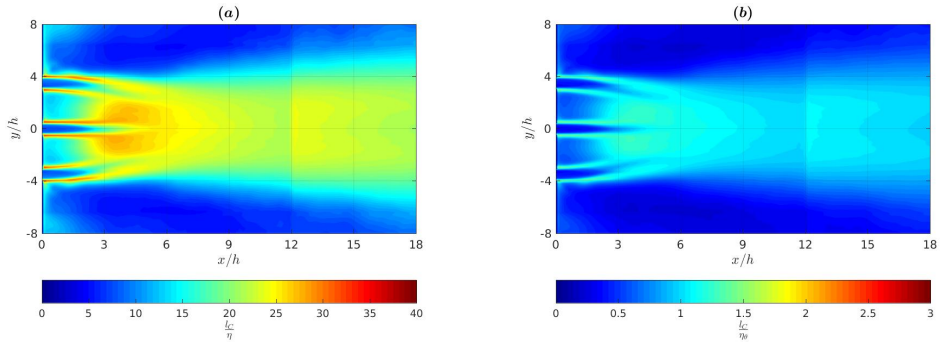

Figure 4.3: Contours of characteristic computational cell length to smallest velocity (Kolmogorov) (a) and thermal (Corrsin) (b) scales ratio evaluated from the coarse LES/DNS.

Fig.4.3(a) relates to the velocity field, and we can see that the coarse numerical mesh resulted in the ratio of 30 in the shear regions between the central and side jets, indicating that even finer mesh needs to be employed in order to have a well-resolved LES. We observed a reduced range of 5-10 in the case of the finer LES/DNS. In contrast, the ratio of thermal length scales is showing the well-resolved simulations for temperature (practically DNS) even on the coarser mesh level, Fig.4.3(b).

4.4 Results

4.4.1 Qualitative analysis of the flow and thermal fields

To provide insights into a three-dimensional structure of the parallel triple-jet of sodium, we plot isovolumes of the vorticity magnitude (15-45 Hz), colored by instantaneous velocity and temperature, respectively, Figs.4.4(a),(b). These structures are plotted for the fine numerical mesh.

The process of merging and mixing the central and side jets is nicely illustrated. The contours of the modulus of the instantaneous velocity in the central vertical plane for the coarse-mesh LES, fine-mesh LES, and T-RANS simulations are shown in Fig.4.5. Distinct imprints of the three jets can be clearly seen in the proximity of the inlet plane followed by a formation of the central mixing region. As expected, the fine mesh LES/DNS (Fig.4.5(b)), shows the flow in the greatest detail, where T-RANS provides a rather smooth distribution, Fig.4.5(c). The contours of the instantaneous temperature in the central vertical plane for various simulation techniques are shown in Fig.4.6. The imprints of the three jets are again visible in the proximity of the inlet. In contrast to the velocity structures, here the presented temperature structures in the entire cross-section show more diffusive structures, due to the considered low-Prandtl value.

The contours of the long-term time-averaged turbulent kinetic energy obtained with different simulation techniques in the central vertical plane are shown in Figs.4.7 (a),(b),(c). For all simulation techniques, two distinct peaks of the turbulent kinetic energy at the start of the triple-jet mixing region can be observed together with dominant shear regions

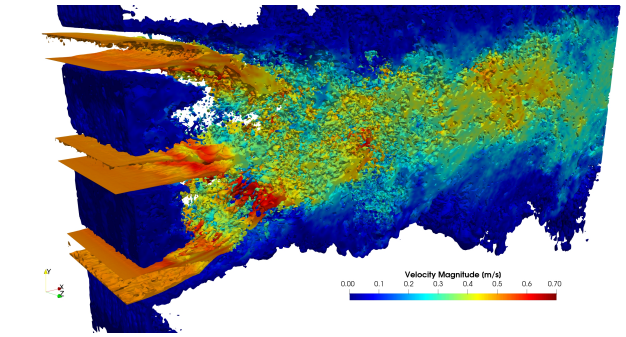

(a)

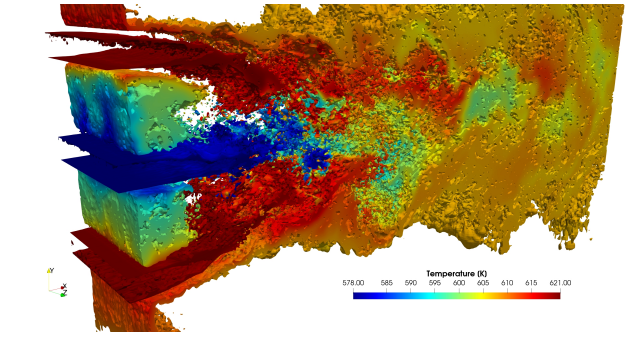

(b)

Figure 4.4: Isovolumes of the instantaneous vorticity magnitude (15-45 Hz) colored by instantaneous velocity magnitude (a) and temperature (b) - data extracted from a fine mesh LES/DNS.

between the jets. The characteristic peak values are similar for the coarse- (Fig.4.7(a)) and fine-LES (Figs.4.7(b)), whereas T-RANS values are slightly underpredicted, Fig.4.7(c). Furthermore, the horizontal extension (i.e. x/h=9) of the regions characterized by high values of the turbulent kinetic energy is similar for all the presented simulation techniques. For the T-RANS, the total turbulent kinetic energy was split into the numerically resolved (Fig.4.7(d)) and modeled (Fig.4.7(e)) contributions, i.e. $k_{tot} = k_{res} + k_{mod}$, $k_{res} = \frac{1}{2}\overline{(u_i' u_i')}$, $k_{mod} = \mathrm{PDE}(k)$, where PDE is the partial differential equation Eq.(4.17). It can be seen that for the T-RANS approach the modeled contribution is dominant and that numerically resolved contributions are confined to the central mixing region, i.e. up to x/h=15. The contours of the long-term time-averaged temperature variance in the central-vertical plane with various simulation techniques are shown in Fig.4.8. For both coarse- (Fig.4.8(a)) and fine-mesh (Fig.4.8(b)) LES/DNS approach contours show slightly asymmetrical distributions, which is a consequence of the shorter duration of the long-term time-averaging procedure (due to limited computational resources). In contrast, the T-RANS results exhibit a fully symmetrical distribution, Fig.4.8(c). For all simulation techniques, two characteristic peaks are observed, and in contrast to the turbulent kinetic energy, the

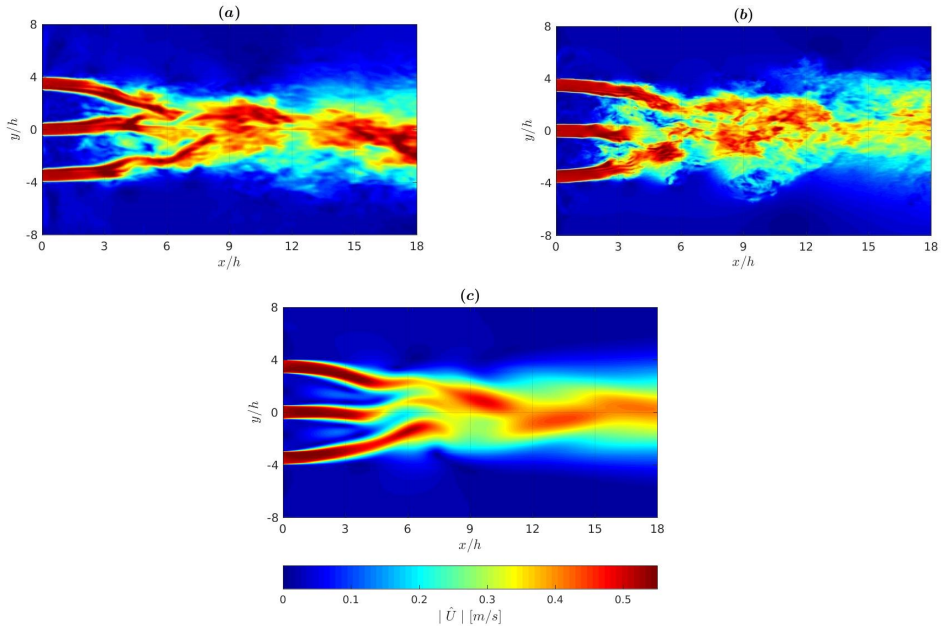

Figure 4.5: Contours of instantaneous velocity magnitude in the central vertical plane - data obtained from the coarse-mesh LES/DNS (a), fine-mesh LES/DNS (b) and T-RANS (c).

T-RANS simulation shows higher peaks in comparison to the LES/DNS. The total contribution of temperature variance is again split into the numerically resolved and modeled contributions, i.e. $(k_\theta)_{tot} = (k_\theta)_{res} + (k_\theta)_{mod}$, $(k_\theta)_{res} = \frac{1}{2}\overline{(\theta'\,\theta')}$, $k_{mod} = \mathrm{PDE}(k_\theta)$, Eq.(4.19). It can be seen that now the numerically resolved contribution is larger than its modeled counterpart, Figs.4.8(d) and (e). It is interesting to note that the resolved contribution shows small values up to x/h=3, where it is surpassed by the modeled contribution.

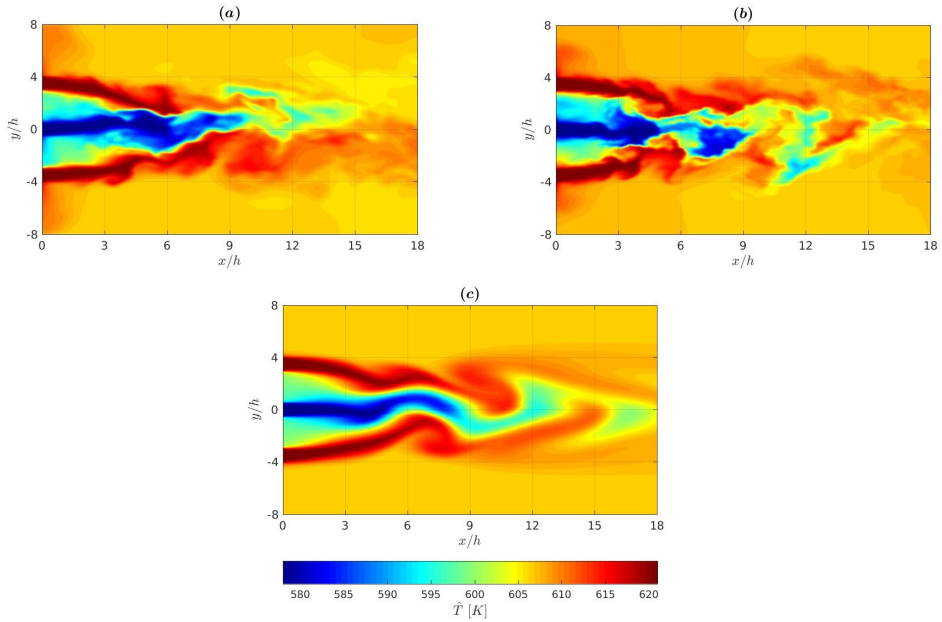

Figure 4.6: Contours of instantaneous temperature in the central vertical plane - data obtained from the coarse-mesh LES/DNS (a), fine-mesh LES/DNS (b) and T-RANS (c).

4.4.2 Quantitative analysis of the flow field

Next, we move to perform a comparative assessment of the simulated velocity field with available measurements and/or simulations from literature. The long-term time-averaging was performed for all simulation techniques and the statistically convergent results were obtained for 24 (T-RANS), 85 (coarse-mesh LES/DNS) and 128 (fine-mesh LES/DNS) Flow-Through-Times (FTTs), respectively. The FTT was defined as the time required by the massless fluid particle to move from the inlet to the outlet of the mixing domain at the constant jet velocity U_J, giving approximately FTT of 1.18 s for both simulated domains.

The non-dimensional profiles of the mean and fluctuating streamwise velocity component at x/h=5 are shown in Figs.4.9(a) and (b), respectively. The profiles of the mean streamwise velocity exhibit good agreement with experimental data of [13] (extracted from [17]), and LES results of [17] obtained with two different SGS closures: the standard Smagorinsky (denoted as LES-S) and the WALE (denoted as LES-W) models. The results shown for comparison with the present results are for the finest mesh of [17], which contained about $8.7 \cdot 10^6$ elements with an average ratio Δ/η_k = 21, which is similar to our numerical simulations with the coarse-LES approach. The peaks and outer regions are well captured with the fine-mesh LES/DNS, whereas a slight asymmetry is visible in the central region, Fig.4.9(a). The slight asymmetry is also visible in experimental data and LES-W of [17], although the present simulations indicate smaller values in the inner region. This asymmetry can be attributed to the very long-time persisting flipping behavior

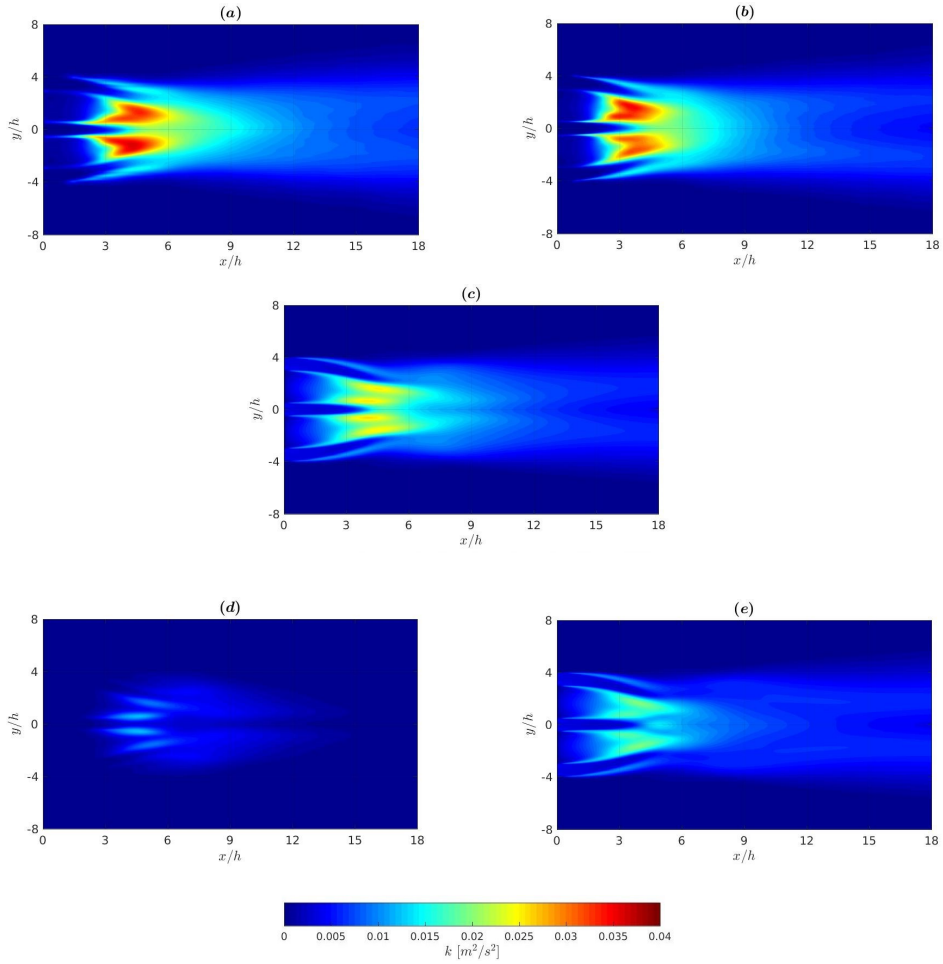

Figure 4.7: Contours of the long-term time-averaged turbulent kinetic energy from the coarse-mesh LES/DNS (a), fine-mesh LES/DNS (b) and T-RANS (c). In addition, contours of the numerically resolved (d) and modeled (e) contributions to the T-RANS results (c).

of the central jet that can require a much-longer time-averaging procedure, which was not computationally affordable. The profiles of the non-dimensional fluctuating streamwise component at the same location x/h=5 show particularly good agreement with the present fine-mesh LES, as shown in Fig.4.9(b).

Comparative assessment of the mean streamwise velocity profiles with here adopted simulation techniques at various locations x/h=1, 5, 9, and 13, is shown in Fig.4.10. Close to the inlet plane, i.e. x/h=1, the coarse- and fine-mesh LESs show a good agreement, while the T-RANS simulation produces slightly larger peak values of the jets and larger negative values between the central and side jets, indicating a stronger backflow here,

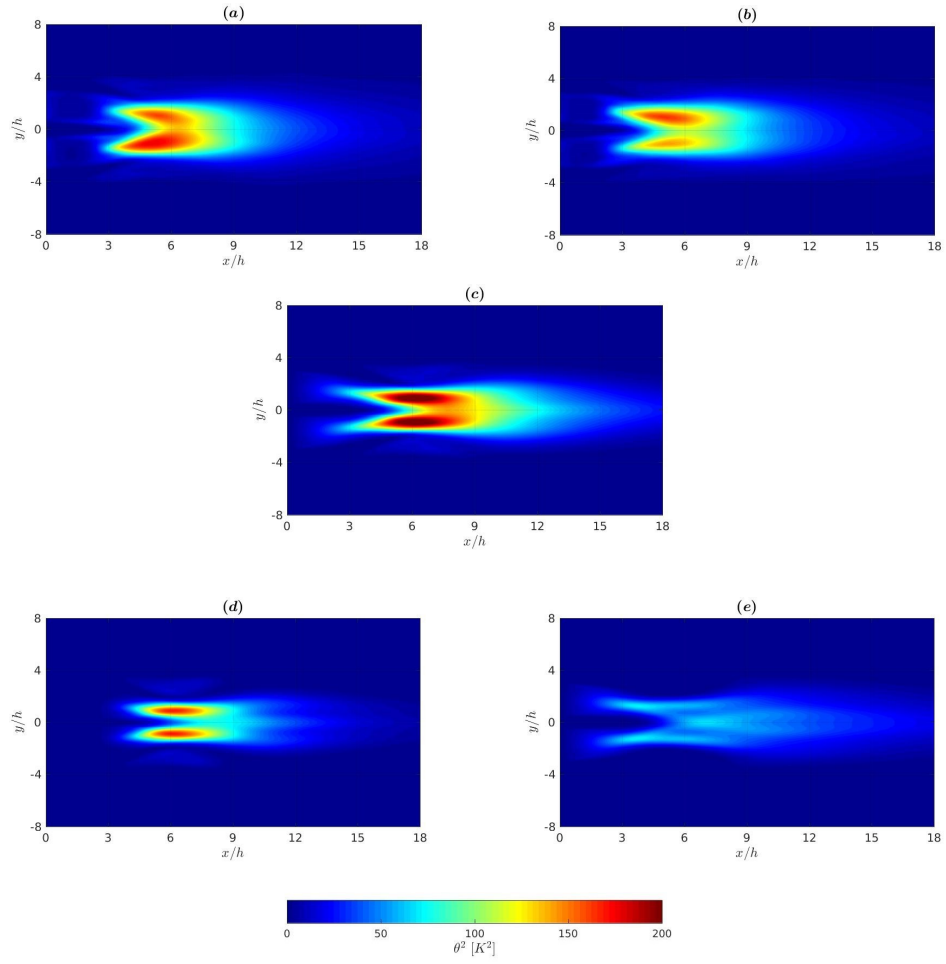

Figure 4.8: Contours of the long-term time-averaged temperature variance from the coarse-mesh LES/DNS (a), fine-mesh LES/DNS (b) and T-RANS (c). In addition, contours of the numerically resolved (d) and modeled (e) contributions to the T-RANS results (c).

Fig.4.10(a). At the x/h=5 location (already previously addressed regarding comparison with our LES and results from literature), a relatively good agreement between the present T-RANS and LES results is obtained, where the T-RANS profiles exhibit a fully symmetrical distribution and peaks are slightly overestimated. At farther downstream locations, x/h=9 and x/h=13, the distinct triple-jet imprint is not visible anymore confirming an efficient mixing of the side and central jets, Figs.4.10(c) and (d). For these locations, an overall very good agreement is observed between various simulation techniques.

The profiles of the non-dimensional turbulent kinetic energy (k/U_J^2) at identical locations are shown in Fig.4.11. Close to the inlet location, at x/h=1, the T-RANS simula-

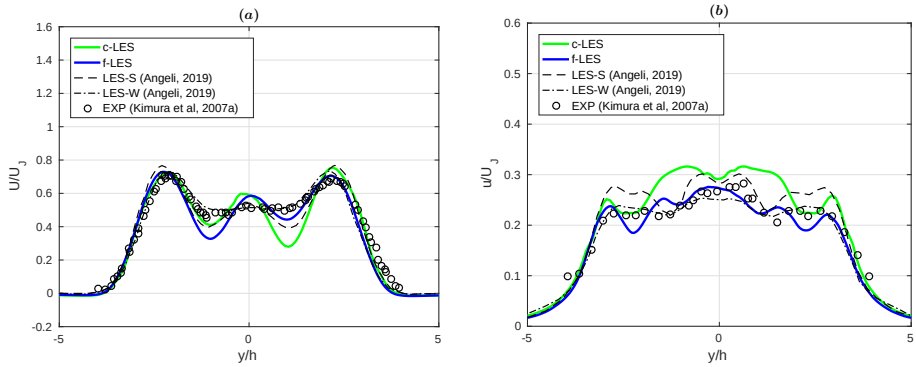

Figure 4.9: Profiles of the mean non-dimensional streamwise velocity (a) and fluctuating (b) contributions at x/h = 5.

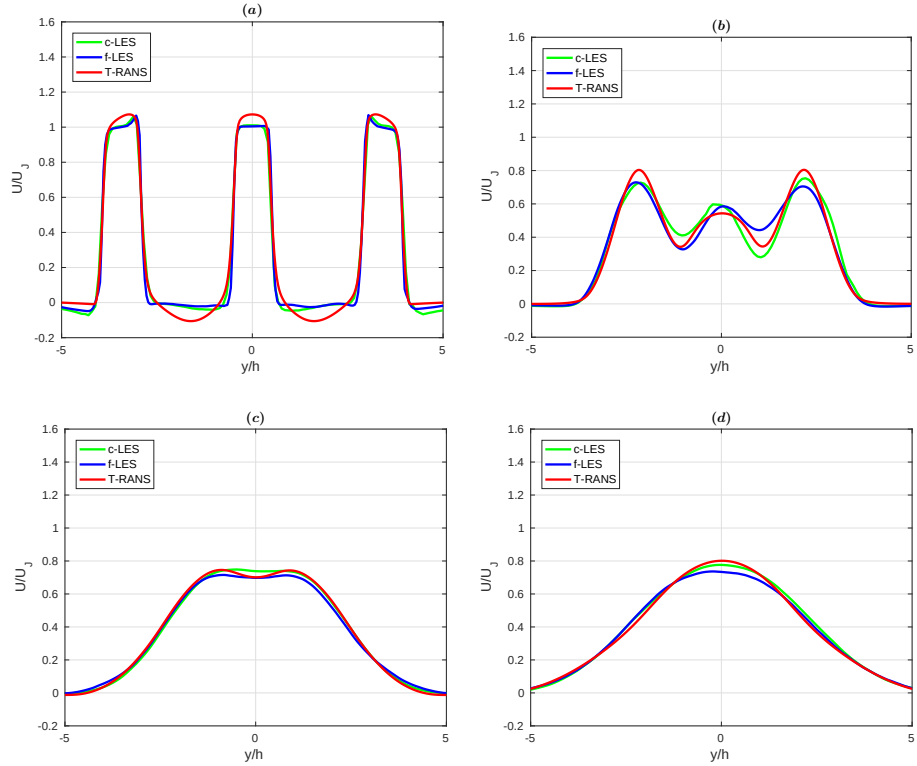

Figure 4.10: Profiles of the non-dimensional mean streamwise velocity at different locations: x/h=1, 5, 9 and 13.

tion shows higher levels of turbulence compared to the coarse-mesh and fine-mesh LESs, Fig.4.11(a). The latter have a good overlap except at the edge of the outer zone, where the peak shear location is underpredicted by the coarse-mesh LES. In contrast, all simulations are showing a good agreement in peak values of the turbulent kinetic energy at the central jet shear zones. At x/h=5 location, the coarse-mesh LES overpredicts the fine-mesh LES in the central region, Fig.4.11(b). The T-RANS profiles exhibit characteristic 6-peak behavior, indicating a slower merging of the side- and central jet. In the central region, the peak values of T-RANS are slightly underpredicted in comparison with the fine-mesh LES. Farther downstream, at x/h=9 location, the T-RANS peak values show a very good agreement with the fine-mesh LES, despite having a less established mixing (indicated by a presence of two little peaks around the center-line), Fig.4.11(c). At the same location, the coarse-mesh LES is showing a single peak behavior, but with its peak value overpredicting the fine-mesh LES. Finally, at the x/h=13 location, differences between simulations are smaller, and the coarse-mesh LES are again overpredicting the center-line value, Fig.4.11(d).

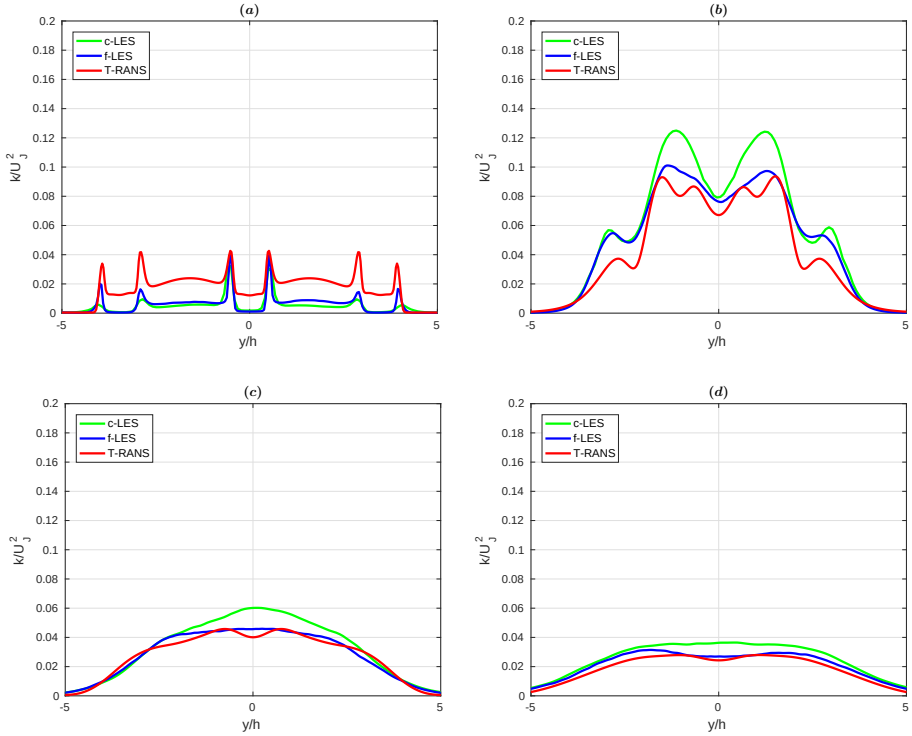

Figure 4.11: Profiles of the normalized turbulent kinetic energy at different locations: x/h = 1, 5, 9 and 13.

The profiles of the non-dimensional turbulent shear-stress component (uv/U_j^2) at the same locations are presented in Fig.4.12. The T-RANS simulation overpredicts the peak values in comparison with both the coarse-mesh and fine-mesh LESs at x/h=1 location,

Fig.4.12(a). At location x/h=5, the agreement between the coarse-mesh and fine-mesh LES is generally good, with an overprediction of the coarse-mesh LES in the central region, Fig.4.12(b). Here, the T-RANS profile overpredicts the peak values. This trend of T-RANS overprediction is also visible at the x/h=9 location, albeit with outer peaks now closer to the LES values, Fig.4.12(c). At the x/h=15 location, the coarse- and fine-mesh LES show good agreement, while the T-RANS profile is now underestimating the outer peak values, Fig.4.12(d).

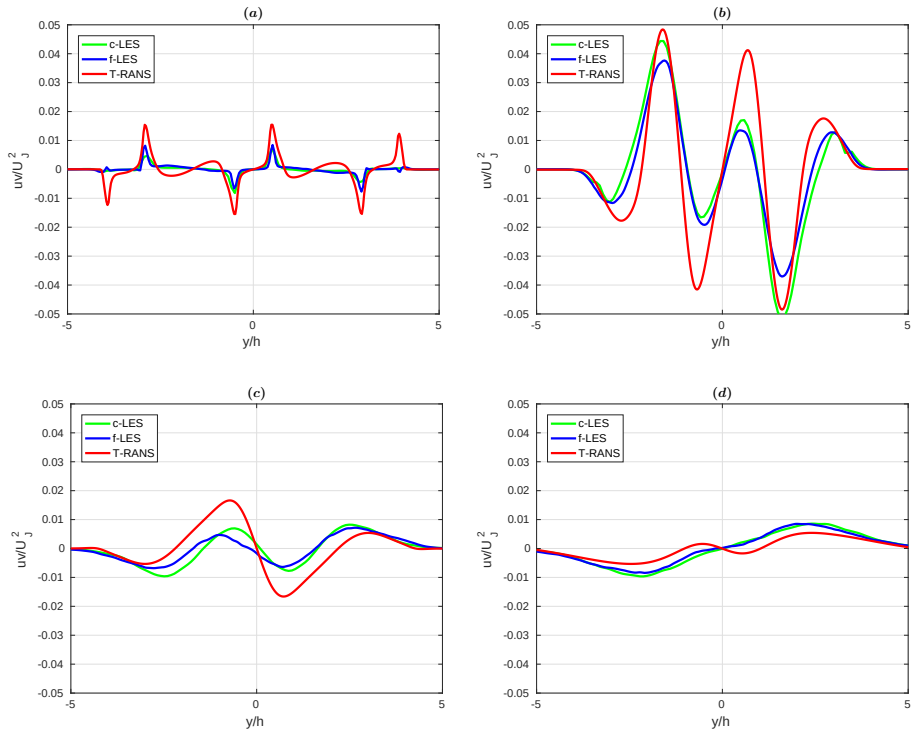

Figure 4.12: Profiles of normalized turbulent shear-stress component at different locations: x/h=1, 5, 9 and 13.

4.4.3 Quantitative analysis of the thermal field

The non-dimensional mean temperature profiles obtained with the presented simulations are compared with experiments of [13] [14] and LES of [15] at x/h =1 and 5, as shown in Figs.4.13(a) and (b). The current LES/DNS results are in very good agreement with experiments at both locations, and they are showing some improvements at the x/h=5 location in comparison with LES of [15]. The present T-RANS results also show an overall good agreement with experiments with some deviations in the central region at x/h=5 location, Fig.4.13(b). At x/h=9 location, the T-RANS simulation overpredicts side-jet peaks, whereas the central region is underpredicted, Fig.4.13(c). Finally, at x/h=13, a good overlap

is obtained among the various simulation techniques, Fig.4.13(d).

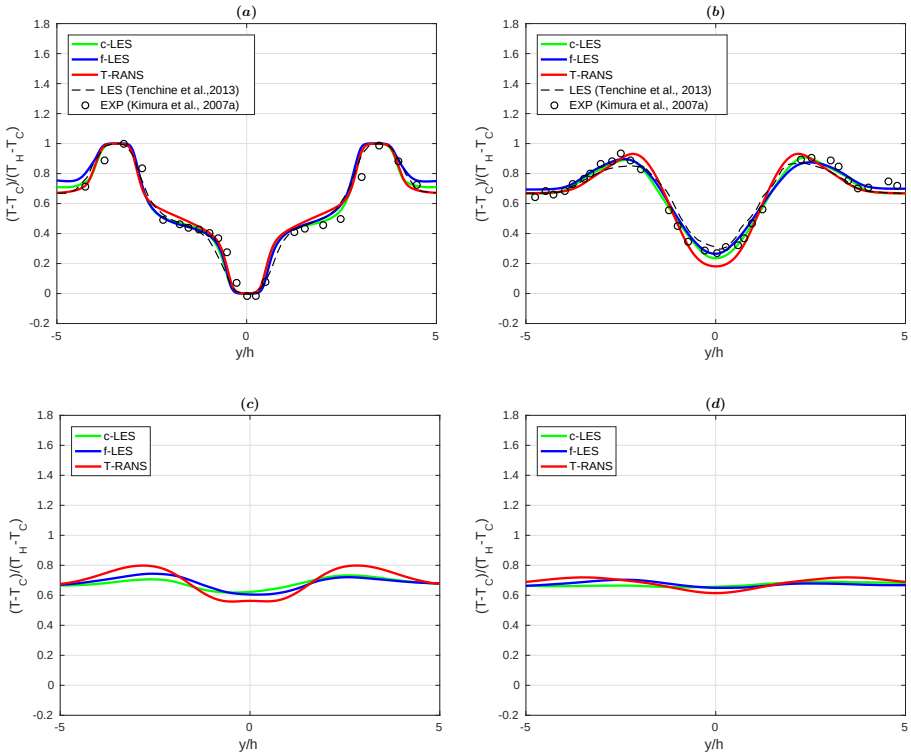

Figure 4.13: Profiles of the normalized long-term time-averaged temperature profiles at different locations: x/h = 1, 5, 9 and 13.

The normalized temperature fluctuations profiles are shown in Fig.4.14. Close to the inlet, current LES/DNSs are showing overprediction than the experimental data, Fig.4.14(a). The agreement is better at x/h=5, where the peak values are well predicted, while the centerline value is still overpredicted, Fig.4.14(b). Farther downstream, both coarse- and fine-mesh LES/DNSs are showing a good overlap, and a transition from the double- to single-peak behavior is observed, Figs.4.14(c),(d). In contrast to the present LES/DNS results, the agreement of thermal fluctuation profiles from T-RANS simulation with experiments is less satisfactory at x/h=1 and 5. A significant overprediction is obtained at these and remaining locations indicating that further refinements of the $k_\theta - \varepsilon_\theta$ model are necessary. The overestimation indicates a too-weak dissipation of the temperature fluctuations. The first step in improving T-RANS simulations could be in making a stronger contribution of the source terms in the transport equation of ε_θ, Eq.(4.20), but this further optimization and model recalibration are outside of the scope of the present work.

The profiles of the non-dimensional vertical component of the turbulent heat flux calculated with the coarse- and fine-mesh LES/DNSs are shown in Fig.4.15. A good agreement

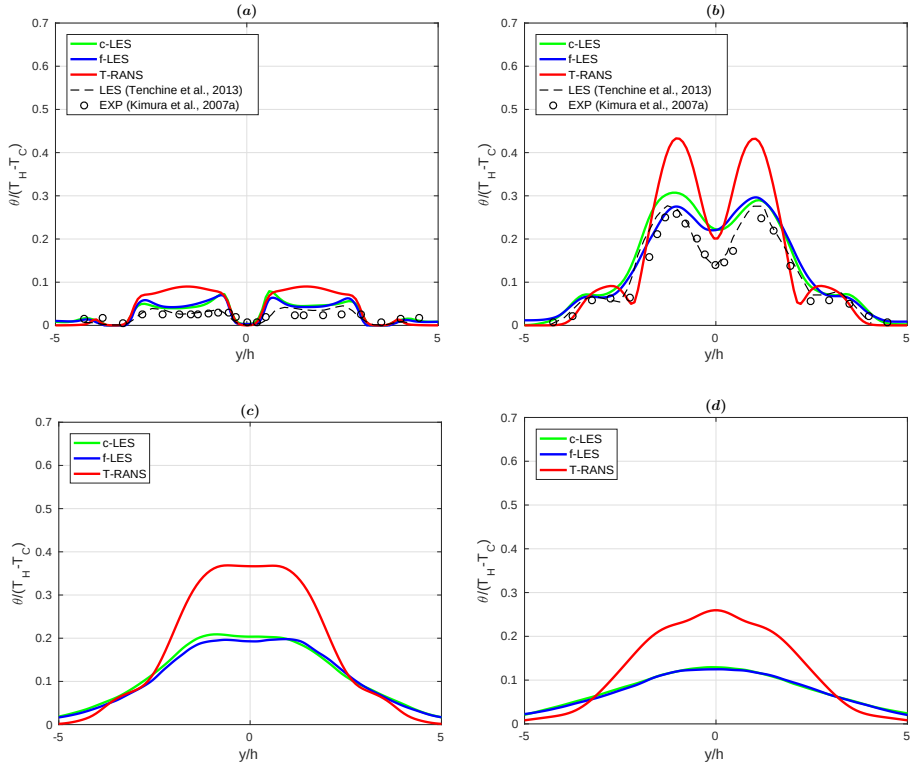

Figure 4.14: Profiles of the non-dimensional temperature fluctuations at different locations: x/h = 1, 5, 9 and 13.

is obtained for the larger distances from the inlet (at x/h = 9 and 13, Figs.4.15(c),(d)). Closer to the inlet, the coarse-mesh overestimates the fine-mesh LES results at both x/h=1 and 5, Figs.4.15(a),(b). This discrepancy can be due to already observed turbulent kinetic energy differences between the coarse- and fine-mesh LES results at these locations.

4.4.4 Frequency-based power spectra

In addition to the already discussed instantaneous and time-averaged flow and thermal features, we focus on the monitoring of the time-dependent evolution of the temperature at the following location in the central vertical plane (z/h=0): x/h=5, y/h=0.75. This location is selected in order to make a direct comparison with thermocouple measurements performed by [13] [14]. The experimental studies of [14] used thermocouples with an accuracy of 0.1°C and time constant of approximately 20 ms. The measured temperature signal contained 20 000 samples with an interval of Δt = 0.01 s. The characteristic time-series of the non-dimensional temperature signal at the given monitoring location ($T^* = (T - T_C)/(T_H - T_C)$) for various simulation techniques are shown in Fig.4.16. The oscillatory behavior with a periodic signal indicates the presence of the Kelvin-Helmholtz

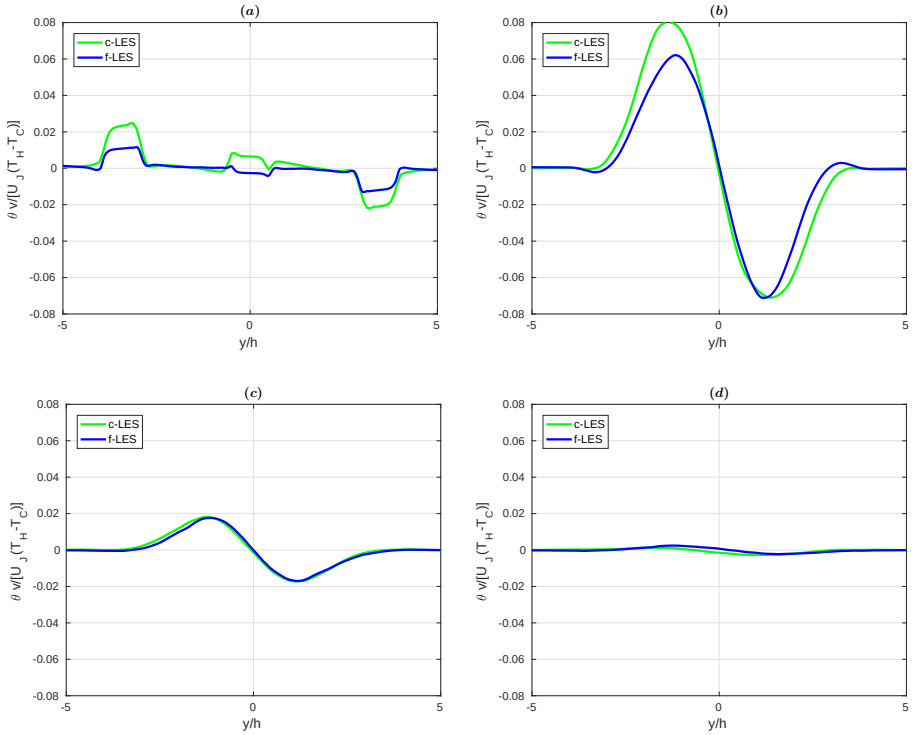

Figure 4.15: Profiles of the normalized vertical component of the turbulent heat flux at the different locations: x/h = 1, 5, 9 and 13.

instabilities triggered by the strong shear between the hot side jets and cold central jet. Note that due to purposes of the clarity of time-evolution of the temperature signal, a short time interval of 2 s was shown. It can be seen that the T-RANS signal exhibits a more regular behavior when compared to the coarse- and fine-mesh LES, portraying a distinct periodic signal. Furthermore, the amplitude of the T-RANS signal oscillations is fixed around $T^* = 0.75$ value. The PSD distributions for various simulation techniques are then analyzed. In experimental studies, a reduced temperature data set of 1024 samples and a time length of 10.24 s was extracted from the entire measured data of 200 s, and a Gaussian filter was applied. In total 200 data sets were generated by shifting the data array by one second in the total measured data. Then, the extracted data sets were converted by applying the Discrete Fourier Transform (DFT) and the final PSD was obtained by averaging all the 200 data sets. In conclusion, the authors mentioned that they have observed a prominent frequency component in their PSD distribution, but without any additional details. In the present study, we followed a simpler approach in calculating the PSD of the temperature time series for different simulation techniques, [12], [35], [36]. For each time signal, we performed analysis over three different time lengths, which were varying from 2 s to 25 s for T-RANS, and from 2 s to 100 s for coarse- and fine-mesh LES.

Note that a shorter time length of T-RANS (with a maximum of 25 s) was because of its significantly faster rate in obtaining the statistically convergent first- and second-order moments when compared to the LES approach. Then, the DFT was calculated for each time length, and the final PSD was plotted and compared with experiments (where experimental data were extracted from plots in Fig.5 in [14]). The final PSD distributions $E_\theta(f) = \frac{1}{2}\theta'\theta'$ (where $\theta' = \hat{T} - \langle\overline{T}\rangle$) are then systematically shifted vertically by factor 10^{-2} for a sake of readability. The PSD distributions obtained with T-RANS data for three different time length intervals are shown in Fig.4.16. Independently of the time length interval, the T-RANS predicts two peak frequencies, f_0 = 2.2 Hz and 4.5 Hz, respectively, which are in reasonable agreement with the experimental f_0 = 2.6 Hz and 3.3 Hz data. The T-RANS distributions are not showing inertial and dissipative parts of the spectra even for the longest time length, indicating that only vortex-shedding-like frequency is captured. Note that here we made an analogy with the spatial spectra since the highest frequencies are also associated with the largest wave numbers that correspond to the smallest length-scales present in the flow, and similarly, the lowest frequencies are associated with the largest flow length-scales, [37]. In contrast to the T-RANS, the coarse- and fine-mesh LES results capture both inertial and dissipative regions, as shown in the same Fig.4.16. In the case of the coarse-mesh LES, the short time length (0-2 s) predicts the single peak frequency around f_0 = 2 Hz. With a further increase of time length, a shifted leading frequency of f_0 = 3.5 Hz is captured for the longest time length (0-100 s), which is in close agreement with the second experimental peak (f_0 = 3.3 Hz). The fine-mesh LES shows a consistent tendency of capturing the peak frequency of f_0 = 3 Hz for all considered time length intervals. Both LES results are showing well-convergent predictions of the inertial and dissipative regions of the spectra for intermediate and long time length intervals. The dissipative range was absent for the shortest time length interval for LES techniques. The reported results are in good agreement with LES of [15] who applied WALE subgrid closure and a simplified computational domain A, and also captured the single critical frequency around 3 Hz.

It can be concluded that the T-RANS simulation well predicted the most dominant double frequencies, even for the rather short time length interval of just 2 s, but it was not able to capture the dissipation region of the PSD distribution. This double peak behavior can be a consequence of the more realistic representation of the experimental domain B, which included the actual shape of the incoming nozzles, as well as the upper and lower parts of the outer jet regions in the proximity of the inlet plane.

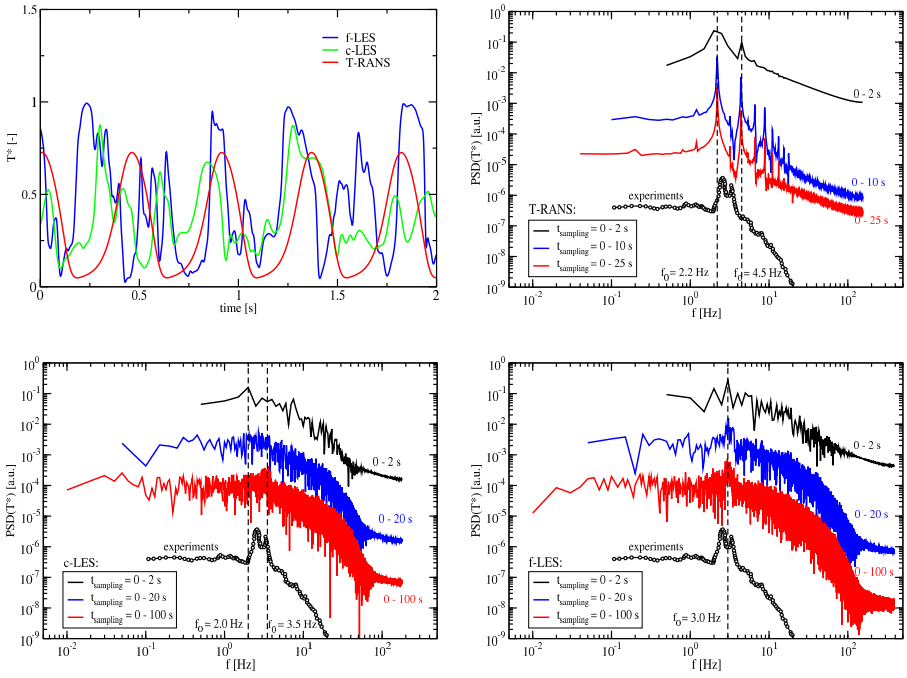

Figure 4.16: Time series and PSD distributions of non-dimensional temperature fluctuations ($T^* = (T - T_C)/(T_H - T_C)$) in the central vertical plane at x/h = 5 and y/h = 0.75 from T-RANS, coarse-mesh LES and fine-mesh LES - comparison with experimental data of [14].

4.5 Conclusions

In the present study, we performed combined dynamic wall-resolved LES/DNS of the forced convection low-Prandtl triple-jet configuration that represents the PLAJEST experiments of [13] [14]. The first- and second-moments of the velocity and temperature were extracted at characteristic locations in the central vertical plane at different distances from the inlet plane and were compared with available experimental data at particular locations. Furthermore, we also performed the T-RANS simulations with the high Reynolds variant (i.e. wall-functions approach) of the four-equation ($k - \varepsilon - k_\theta - \varepsilon_\theta$) model, which does not require a priori specification of Pr_t. The non-dimensional mean streamwise velocity profiles at different locations from the inlet obtained with coarse-, fine-mesh LES/DNS, and T-RANS simulation showed a good agreement. The profiles of non-dimensional turbulent kinetic energy at the same locations showed a good agreement between the fine-mesh LES/DNS and T-RANS simulation, whereas the coarse-mesh LES/DNS results were over-predicted in the central mixing region. The non-dimensional mean temperature profiles also showed a good agreement between all presented numerical simulation techniques and available experimental data. The profiles of the non-dimensional temperature variance demonstrated a good agreement between the coarse- and fine-mesh LES/DNS, while the

T-RANS simulation exhibited a significant overprediction. The PSD analysis of the temperature signal demonstrated the ability of the applied T-RANS approach to capture the leading frequency in good agreement with experiments even for a very short length of the time interval. The coarse-mesh LES/DNS was much more sensitive to a change of the length of the time interval. In contrast, the fine-mesh LES/DNS captured the leading frequency independently of the length of the time interval. Both coarse- and fine-mesh LES/DNS results demonstrated the existence of the inertial and dissipative regions of the spectra. The dissipation regime was not present in the spectra of the T-RANS approach, demonstrating its inability to capture the instabilities of the smaller flow structures. Despite this, especially from the perspective of industrial-scale applications, the T-RANS approach, with an improved version of the high-Reynolds variant of the four-equation ($k-\varepsilon-k_\theta-\varepsilon_\theta$) model, can be an interesting alternative to the computationally more demanding LES/DNS technique. Here presented results of the high-fidelity fine-mesh LES/DNS, especially regarding the temperature variance and turbulent heat flux profiles, can be used for further improvement and recalibration of T-RANS models for low-Prandtl fluids. Since accurate information on temperature fluctuations (its amplitude and frequency) are prerequisite for predictions of thermal fatigue that can occur in the mixing jet regions (and potentially cause thermal striping and cracks), the wall-resolving dynamic LES/DNS approach is recommended.

References

[1] B. S. Triplett, E. P. Loewen, B. J. Dooies, PRISM: A Competitive Small Modular Sodium-Cooled Reactor, Nuclear Technology 178 (2012) 186–200.

[2] S. L. Soloviev, D. G. Zaryugin, S. G. Kalyakin, S. T. Leskin, Identifying the key development areas for small nuclear power plants, Nuclear Energy and Technology 8 (2) (2022) 115–120.

[3] K. Van Tichelen, G. Kennedy, F. Mirelli, A. Marino, A. Toti, D. Rozzia, E. Cascioli, S. Keijers, P. Planquart, Advanced liquid-metal thermal-hydraulic research for MYRRHA, Nuclear Technology 206 (2020) 150–163.

[4] G. Grötzbach, Challenges in low-Prandtl number heat transfer simulation and modelling, Nuclear Engineering and Design 264 (2013) 41–55.

[5] A. Shams, F. Roelofs, E. Baglietto, S. Lardeau, S. Kenjeres, Assessment and calibration of an algebraic turbulent heat flux model for low-Prandtl fluids, Int. J. Heat and Mass Transfer 79, (2014) 589–601.

[6] F. Roelofs, A. Shams, I. Otic, M. Böttcher, M. Duponcheel, Y. Bartosiewicz, D. Lakehal, E. Baglietto, S. Lardeau, X. Cheng, Status and perspective of turbulence heat transfer modelling for the industrial application of liquid metal flows, Nuclear Engineering and Design 290 (2015) 99–106.

[7] W. M. Kays, Turbulent Prandtl number - Where are we?, Journal of Heat Transfer 116 (1994) 284–295.

[8] R. Da Viá, S. Manservisi, F. Menghini, A $k-\Omega-k_\theta-\Omega_\theta$ four parameter logarithmic turbulence model for liquid metals, Nuclear Engineering and Design 101 (2016) 1030–1041.

[9] A. De Santis, A. Shams, Application of an algebraic turbulent heat flux model to a backward facing step flow at low Prandtl number, Annuals of Nuclear Energy 117 (2018) 32–44.

[10] A. De Santis, A. Villa Ortiz, A. Shams, L. Koloszar, Modelling of a planar impinging jet at unity, moderate and low Prandtl number: Assessment of advanced RANS closures, Annuals of Nuclear Energy 129 (2019) 125–145.

[11] E. Cascioli, S. Buckingham, S. Keijers, K. Van Tichelen, S. Kenjereš, Numerical and experimental analysis of a planar jet with heated co-flow at medium and low Prandtl-number values, Nuclear Engineering and Design 361 (2020) 110570.

[12] E. Cascioli, S. Keijers, K. Van Tichelen, J. E. Vesper, S. Kenjereš, Combined Large-Eddy and Direct Numerical Simulations of a Planar Jet with Heated Co-Flow with Medium and Low Prandtl Fluids, International Journal of Heat and Mass Transfer 191 (2022) 122774.

[13] N. Kimura, H. Kamide, P. Emonot, K. Nagasawa, Study on Thermal Striping Phenomena in Triple-Parallel Jet – Investigation on Non-Stationary Heat Transfer Characteristics Based on Numerical Simulation, Proceedings of 12th International Topical Meeting on Nuclear Reactor Thermal Hydraulics (NURETH-12), Pittsburgh, USA (2007a).

[14] N. Kimura, H. Miyakoshi, H. Kamide, Experimental investigation on transfer characteristics of temperature fluctuation from liquid sodium to wall in parallel triple-jet, International Journal of Heat and Mass Transfer 50 (2007b) 2024–2036.

[15] D. Tenchine, S. Vandroux, V. Barthel, O. Cioni, Experimental and numerical studies on mixing jets for sodium cooled fast reactors, Nuclear Engineering and Design 263 (2013) 263–272.

[16] F. Nicoud, F. Ducros, Subgrid-scale stress modelling based on the square of the velocity gradient tensor, Flow, Turbulence and Combustion 62 (13), (1999) 183–200.

[17] P. E. Angeli, Verification and validation of LES of a triple parallel jet flow in the context of a thermal striping investigation, Nuclear Engineering and Design 353 (2019) 110210.

[18] S. Kenjereš, K. Hanjalić, Transient analysis of Rayleigh-Bénard convection with a RANS model, Int. J. Heat and Fluid Flow 20(3) (1999), 329–340.

[19] S. Kenjereš, K. Hanjalić, LES, T-RANS and hybrid simulations of thermal convection at high Ra numbers, Int. J. Heat and Fluid Flow 27(5) (2006), 800–810.

[20] S. Kenjereš, K. Hanjalić, Tackling complex turbulent flows with transient TRANS, Fluid Dynamics Research 41 (2009), 012201.

[21] M. Nishimura, A. Tokuhiro, N. Kimura, H. Kamide, Numerical study on mixing of oscillating quasi-planar jets with low Reynolds number turbulent stress and heat flux equation models, Nuclear Engineering and Design 202 (1) (2000) 77–95.

[22] S. B. Pope, Turbulent Flows, Cambridge University - Cambridge Univ. Press. (2000).

[23] M. Germano, U. Piomelli, P. Moin, W. H. Cabot, A dynamic subgrid-scale eddy viscosity model, Physics of Fluids A 3 (1991) 1760–1765.

[24] J. Smagorinsky, General circulation experiments with the primitive equations. I. The basic experiment, Monthly Weather Review 91 (1963) 99–164.

[25] D. K. Lilly, A proposed modification of the Germano subgrid-scale turbulence closure method, Physics of Fluids A 4 (1992) 633–635.

[26] B. W. Righolt, S. Kenjereš, R. Kalter, M. J. Tummers, C. R. Kleijn, Dynamics of an oscillating turbulent jet in a confined cavity, Physics of Fluids 27 (2015) 1–16.

[27] B. W. Righolt, S. Kenjereš, R. Kalter, M. J. Tummers, C. R. Kleijn, Electromagnetic control of an oscillating turbulent jet in a confined cavity, International Journal of Heat and Fluid Flow 62 (2016) 395–406.

[28] K. Abe, T. Kondoh, Y. Nagano, A new turbulence model for predicting fluid flow and heat transfer in separating and reattaching flows - II, Thermal calculations, International Journal of Heat and Mass Transfer 38 (8) (1995) 1467–1481.

[29] S. Manservisi, F. Menghini, A CFD four parameter heat transfer turbulence model for engineering applications in heavy liquid metals, International Journal of Heat and Mass Transfer 69 (2014) 312–326.

[30] S. Manservisi, F. Menghini, CFD simulations in heavy liquid metal flows for square lattice bare rod bundle geometries with a four parameter heat transfer turbulence model, Nuclear Engineering and Design 295 (2015) 251–260.

[31] B. E. Launder, D. B. Spalding, The numerical computation of turbulent flows, Computed Methods in Applied Mechanics and Engineering 3 (1973) 269–289.

[32] R. I. Issa, A. D. Gosman, A. P. Watkins, The computation of compressible and incompressible recirculating flows by a non-iterative implicit scheme, Journal of Computational Physics 62 (1986) 66–82.

[33] J. Kobayashi, M. Tanaka, S. Ohno, H. Ohshima, H. Kamide, Proposal of benchmark problem of thermal striping phenomena in planar triple parallel jets tests for fundamental code validation in sodium-cooled fast reactor development, Proceedings of 16th International Topical Meeting on Nuclear Reactor Thermal Hydraulics (NURETH-16), Chicago, IL, USA (2015).

[34] G. Ruiz-Chavarria, C. Baudet, S. Ciliberto, Scaling laws and dissipation scale of a passive scalar in fully developed turbulence, Physica D 99 (1996) 396–380.

[35] S. Kenjereš, Energy spectra and turbulence generation in the wake of magnetic obstacles, Physics of Fluids 24(11) (2012) 115111.

[36] H. Li. N. K. Anand, Y. A. Hassan, T. Nguyen, Large eddy simulations of the turbulent flows of twin parallel jets, Int. J. Heat and Mass Transfer 129 (2019) 1263–1273.

[37] V. S. Arpaci, P. S. Larsen, Convection Heat Transfer, Prentice-Hall, Inc. New Jersey, USA (1984).

5

Conclusion and outlook

5.1 Conclusions and outlook

Reviewing the research outcome, we can answer the identified research questions:

1. **How can a new universal forced jet-flow configuration be developed to study turbulent heat transfer phenomena of both standard and low-Pr fluids?**

   The first milestone of this research consisted in the Computational Fluid Dynamics (CFD) analysis of the single-jet flow experimentally studied at the von Karman Institute for Fluid Dynamics (VKI). Particularly, we were aiming to perform both industrial CFD, such as Reynolds Averaged Navier-Stokes (RANS) simulations, and high-fidelity CFD, such as Large-Eddy Simulations (LESs) and Direct Numerical Simulations (DNSs). Our simulation results have been presented in chapter 2 and chapter 3, respectively. We observed some asymmetrical behavior of the experimental jet flow, due to different co-flow velocities at the inlet section. This affected the jet flow evolution after the start of self-similar region, where we recognized a deviation of the jet axis and consequent wall-flow interaction. This resulted in a dilemma: adapting CFD modeling such that it mimics the observed asymmetry of the experimental setup, or proposing a more universal CFD configuration. Since our main objective was to contribute to testing and development of Turbulent Heat Transfer (THT) models for liquid metals, we decided for the second option. We generated a rectangular domain with periodic inlets to get fully-developed channel flow and turbulence parameters profiles for both the jet and the co-flow. There was no need for pre-cursor simulations of such channel flows, since we used the mapping function in the OpenFOAM libraries. We also applied cyclic boundary conditions to the front and back patches of the mixing domain. This solution allowed to achieve a fully symmetrical jet flow, which is not dependent on the nozzle geometry (and thus "universal") and is suitable for the production of a numerical reference database. It can be mentioned that one of the challenges consisted in triggering instabilities to achieve fully-developed turbulent flows within the inlet channels, in the case of

LES/DNSs. We achieved this by firstly imposing random fluctuations to the (uniform) velocity profile at the channel inlet with a very short periodicity length, and then increasing the mapping distance until reaching the same value that was set in the former RANS simulations. In conclusion, we developed a universal jet flow configuration, which was used to both produce a numerical reference database for low Prandtl number (Pr) fluids, test basic and advanced RANS low-Pr THT models, and can be used for validation of CFD models.

2. **What is the sensitivity of the forced convection turbulent heat transfer regime to increasing thermal conductivity (i.e. decreasing Prandtl number) of the fluid?**

   The sensitivity analysis of forced convection heat transfer to the Pr value, as presented in chapter 3, provides conclusive insights on the impact of the turbulent flow regime on low-Pr THT phenomena. As a general outcome, we found that forced convection dominates over molecular diffusion. This can be proven by referring to the temperature results, which collapsed on the same profile despite of the (about) three order of magnitude difference in Pr-values. On the other hand, major differences appeared when looking at the temperature fluctuations, where peaks within the potential core and mixing regions decreased by a factor three when going from Pr = 0.71 to Pr = 0.006 . Such peaks were centered in the shear layer regions, which represent the interface between the jet flow and surrounding domain (the heated co-flow in this case). The damping of thermal fluctuation peaks at lower Pr-value can be interpreted like the subtraction of tiny amounts of heat by the molecular conductivity, otherwise transmitted through THT, during the dissipation process at very small thermal scale. Due to the immediate conduction towards the physical walls, this process is crucial in the analysis of thermal striping. Overall, we noticed that the thermal fluctuation profiles tend to sooner lose their characteristic "double-dome" behavior in favor of a single-peak shape, centered around the jet axis. This was particularly evident in the case of Pr = 0.006. A more limited amplitude and shorter range of the thermal turbulent dissipation were also observed by comparing the Power Spectra Density (PSD) profiles. This supports the above analysis. Concluding, to estimate a qualitative temperature field, with limited computational cost, standard industrial CFD can rely on basic THT models in case of forced-jets, even with liquid metals. In contrast, if there is a need to perform fatigue analysis, RANS simulations need to rely on advanced THT models even in the case of forced jets. It is recommended to base future modeling efforts on natural convection flows, where differences among different Pr values can be larger and impact also the first-order statistics.

3. **What is the recommended CFD approach for industrial applications on multiple forced jets with liquid metals?**

   The above answer to the second research question can be integrated with the answer to the third research question, and partially corrected, by referring to the outcome of chapter 4, where we studied the forced sodium triple-jet configuration of [1] [2].

Among the CFD techniques and low-Pr models we tested, we can recommend the Transient-RANS (T-RANS) simulation with a model from the four-equation THT modeling class as a good compromise to get reliable prediction of both thermal fields and dominant peaks of turbulent thermal production. We also observed some over-prediction of the temperature fluctuations, but this can be considered as a calibration issue, which requires some additional tuning of the turbulent thermal production and dissipation of the used THT model. What cannot be achieved is the correct prediction of the dissipation range in the PSD analysis, due to the absence of resolution of smaller thermal scales. Additional testing and refining of the model coefficients, especially for the dissipation rate of the temperature variance, is recommended for future research.

5.2 Future opportunities

In this section, we present future research opportunities, building upon the present work.

5.2.1 Natural convection regime

Liquid metals are characterized by a high thermal conductivity and are therefore being considered as primary coolant option in advanced nuclear reactors, to enhance the heat transfer from the reactor core. Other advantages related to the use of liquid metals, are (i) high boiling point and consequent lower pressurization of the primary circuit; (ii) the fact that large temperature gradients may occur, triggering natural convection within the reactor coolant. The latter can be seen as an intrinsic safety factor, since in the case of loss of power supply, natural circulation and cooling of the core would be established. Therefore, the natural convection regime is recommended for future studies, still with reference to jet flows, i.e. buoyant jets, in order to complement the present research. We also expect for a stronger impact of the THT modeling within (T-)RANS simulations, whereas temperature was just a passive scalar in our forced jet flows. In this case, some experimental and numerical references are available in the literature, which can be used to test higher-order turbulence models, but also to improve and possibly develop the available low-Pr THT models. At first, we recommend the buoyant triple-jet with Pr=0.031 investigated by [3]. The three jets showed a strong interaction, leading to large-scales vortices and accompanied by low-frequency undulations. Due to the high-conductivity of the fluid, an irregular behavior of the turbulent diffusivity of momentum and heat was observed, as well as unexpected relations between the temperature gradient and turbulent heat flux. Another relevant test case is the turbulent buoyant sodium jet investigated by [4], which discharges into a slowly moving pipe flow. The temperature fields were observed to be quite different from those in conventional fluids, with dominance of molecular diffusion rather than turbulent diffusion. This test case is also recommended because of the different experimental conditions, which covered forced-, mixed- and buoyant-convection flow regimes. Finally, still considering the PLAJEST experiment, we know that additional results, possibly covering other flow regimes too, can be accessed through internal reports. It might be worth to ask JAEA for the access and integrate the current availability of experimental data in literature for this test case.

5.2.2 Full-scale applications

Departing from fundamental test cases, it is recommended to test the available and/or improved low-Pr THT models in (T-)RANS simulations on full-scale nuclear reactor models. At SCK CEN, E-SCAPE is suitable for the scope, because it provides information on the flow patterns and heat transport in the Lead-Bismuth Eutectic (LBE) within the plena of pool-type reactors, such as MYRRHA. In fact, first modeling approaches and preliminary results have already been presented in [5], where CFD analyses were performed by using different codes, i.e. STAR-CCM+, ANSYS CFX and OpenFOAM. Where possible, the experimental data from E-SCAPE were used to compare and validate the computational results. In terms of RANS modeling, the standard or realizable $k-\epsilon$ turbulent model and Pr_t=2 were used, leaving some margin to move towards more advanced low-Pr THT models. Considering the global size of the CFD domain, it is not expected that LES/DNS techniques can be applied with an affordable computational cost. It could on the other hand be interesting to employ some "hybrid" RANS-LES CFD techniques, such as the Detached Eddy Simulation (DES), which allow to lower the computational cost by RANS modeling in the near-wall regions and achieve full resolution of large-scale turbulent structures in the bulk regions [6]. Particularly, the use of Delayed DES (DDES) might be considered, since its use of a blending function that varies in the flow domain and smooth transitions between RANS and LES regions [7]. We recommend to test such (D)DES approaches within the upper and lower plena of the E-SCAPE model, in order to properly catch the full spectrum of turbulent and heat fluctuations in the bulk, and correctly predict thermal striping to physical structures.

References

[1] N. Kimura, H. Kamide, P. Emonot, K. Nagasawa, Study on Thermal Striping Phenomena in Triple-Parallel Jet – Investigation on Non-Stationary Heat Transfer Characteristics Based on Numerical Simulation, Proceedings of 12th International Topical Meeting on Nuclear Reactor Thermal Hydraulics (NURETH-12), Pittsburgh, USA (2007a).

[2] N. Kimura, H. Miyakoshi, H. Kamide, Experimental investigation on transfer characteristics of temperature fluctuation from liquid sodium to wall in parallel triple-jet, International Journal of Heat and Mass Transfer 50 (2007b) 2024–2036.

[3] A. Fregni, D. Angeli, A. Cimarelli and E. Stalio, Direct numerical simulation of a buoyant triple jet at low-Prandtl number, International Journal of Heat and Mass Transfer 143 (2019) 118466.

[4] J. U. Knebel, L. Krebs, U. Müller and B. P. Axcell, Experimental investigation of a confined heated sodium jet flow in a co-flow, Journal of Fluid Mechanics 368 (1998) 51–79.

[5] D. C. Visser, S. Keijers, S. Lopes, F. Roelofs, K. Van Tichelen and L. Koloszar, CFD analyses of the European scaled pool experiment E-SCAPE, Nuclear Engineering and Design 358 (2020) 110436.

[6] P. R. Spalart, Detached-eddy simulation, Annual Review of Fluid Mechanics 41(1) (2009) 181-202.

[7] M. Shur, P. R. Spalart, M. Strelets and A. Travin, A hybrid RANS-LES approach with delayed-DES and wall-modelled LES capabilities, International Journal of Heat and Fluid Flow 29(6) (2008) 1638-1649.

Scientific output

Publications

4. **E. Cascioli**, B. Kaaks, S. Keijers, K. Van Tichelen and S. Kenjereš, Numerical analysis of a parallel triple-jet of liquid-sodium in a turbulent forced convection regime, *Submitted to International Communications in Heat and Mass Transfer (2023).*

3. **E. Cascioli**, S. Keijers, K. Van Tichelen, J. E. Vesper, S. Kenjereš, Combined large-eddy and direct numerical simulations of a planar jet with heated co-flow with medium and low Prandtl fluids, International Journal of Heat and Mass Transfer 191 (2022) 122774.

2. **E. Cascioli**, S. Buckingham, S. Keijers, K. Van Tichelen, S. Kenjereš, Numerical and experimental analysis of a planar jet with heated co-flow at medium and low Prandtl-number values, Nuclear Engineering and Design 361 (2020) 1–11.

1. K. Van Tichelen, G. Kennedy, F. Mirelli, A. Marino, A. Toti, D. Rozzia, **E. Cascioli**, S. Keijers and P. Planquart, Advanced liquid-metal thermal-hydraulic research for MYRRHA, Nuclear Technology 206 (2020) 150-163.

Project deliverables

1. **E. Cascioli**, D3.16 - Turbulent heat transfer modeling applied to a jet flow test case, MYRTE project (2019), Work Package: 3, Contact number: 662186.

Conference papers

1. Numerical and experimental analysis on a planar jet with heated co-flow at medium- and low-Prandtl number values, SESAME International Workshop (2019), NRG, Petten (NL).

Poster presentations

3. Physics@Veldhoven (2019), NWO, Veldhoven (NL).

2. Day of the PhD's (2018), SCK CEN, Mol (BE).

1. Heavy Metal Summer School (2016), SCK CEN, Mol (BE).

Oral presentations

8. SESAME International Workshop (2019), NRG, Petten (NL).
7. HiFiLeD Symposium (2018), NUMECA, Brussels (BE).
6. 7^{th} SESAME/MYRTE Progress Meeting (2018), TUD, Delft (NL).
5. 6^{th} SESAME/MYRTE Progress Meeting (2018), JSI, Ljubljana (SL).
4. 5^{th} SESAME/MYRTE Progress Meeting (2017), ENEA, Camugnano (IT).
3. Day of the PhD's (2017), SCK CEN, Mol (BE).
2. DEMOCRITOS 2 - Technical meetings (2016-2019), SCK CEN, Mol (BE) - VKI, Sint-Genesius-Rode (BE).
1. Day of the PhD's (2016), SCK CEN, Mol (BE).

Curriculum vitæ

Edoardo Cascioli

25-10-1988
Born in Rome (Italy)

EDUCATION AND WORK EXPERIENCE

2020-present
Design Engineer
Nuclear Decommissioning Design Group
Métier of Radiation Protection, Radwaste and Decommissioning
Global Nuclear Business Area
Tractebel Engineering S.A.
Brussels (Belgium)

2019-2020
Design Engineer
Thermal Hydraulics and CFD Group
Métier Nuclear Safety and Engineering
Global Nuclear Business Area
Tractebel Engineering S.A.
Brussels (Belgium)

2015-2019
Ph.D. Student
Transport Phenomena Group
Department of Chemical Engineering
Faculty of Applied Sciences
Delft University of Technology
Delft (Netherlands)

2013-2014
Internship
Nuclear Safety and Thermal Hydraulics Group
MYRRHA project
SCK CEN
Mol (Belgium)

2011-2015
Master Degree
Nuclear Specialty
Department of Astronautics, Electrics and Energy Engineering
Faculty of Civil and Industrial Engineering
La Sapienza University
Rome (Italy)

2011
Technical Assistant
Laboratory of Mechanical Engineering
La Sapienza University
Rome (Italy)

2007-2011
Bachelor Degree
Department of Astronautics, Electrics and Energy Engineering
Faculty of Civil and Industrial Engineering
La Sapienza University
Rome (Italy)

2002-2007
Scientific Diploma
Antonio Labriola High School
Rome (Italy)

1999-2002
Caio Duilio Secondary School
Rome (Italy)

1998-1999
Suore della Presentazione Primary School
Rome (Italy)

1994-1998
Suore Mariane Francescane Primary School
Rome (Italy)

Acknowledgments

2015-2019
My doctoral four-year contract started on October 1, 2015. I only spent the first four months at TU Delft (TUD), while I had been office-based at the Belgian Nuclear Research Center (SCK CEN) for the rest of the contractual period. I used to visit TUD and the von Karman Institute for Fluid Dynamics (VKI) once per month, or in any case it was needed to discuss with my promotors and colleagues. I started from scratches with Computational Fluid Dynamics (CFD), but I succeeded in managing different CFD techniques in the first two years, mostly performing benchmark simulations on test cases from literature. Then, I focused on CFD simulations of jet flows: the (new) MYRTE single-jet experiment by VKI and PLAJEST triple-jet experiment by JAEA (2007). This numerical study was carried out in the frame of the European Commission (EC) Horizon 2020 program within the SESAME and MYRTE projects, in which I contributed both presenting during periodic workshops and final conference, and writing one deliverable for the MYRTE project. I also collected all the TUD Graduate School (GS) credits, participated to the Heavy Metal Summer School and other events organized by the SCK CEN Academy, attended OpeFOAM-coding courses provided by VKI, and attended as presenter at two international conferences (HiFiLeD in 2018 and Physics@Veldhoven in 2019).

Concerning this contractual period, I want to first thank my TUD promotor and mentor, Prof. Sasa Kenjereš, who demonstrated a unique mixture of academic knowledge, technical experience, willingness and empathy. I was so excited in the first months under his daily supervision, trying to learn as much as possible, but also enjoying the unique environment of TUD. It is incredible that Sasa is always available for his students and colleagues, even beyond his own duties and priorities. These qualities motivated me even from distance, and let me felt integrated whenever I had the chance to return to TUD for a daily visit. Sasa demonstrated flexibility, great communication and listening attitudes, and this cancelled the geographical distance between us. I really appreciated this, thanks Sasa.

I also thank my second promotor, Prof. Chris Kleijn, for his background support and active follow-up on my research development, as well as the

department management, and the whole TUD organization, for the organization of the doctoral program. I particularly enjoyed the GS courses, which let me further discover and enhance personal skills, such as communication, leadership and problem-solving attitudes.

Concerning my TUD colleagues, I spent a very limited time with them. Nevertheless, I would thank Sid, Manu, Elin, Kevin, Romana and Artem, who helped me in solving some coding issues. They also welcomed me when I was visiting TUD, spending coffee breaks and lunches together, and let me feel "part of the family". I thank Bouke, my (only) master student from TUD, who spent his six-month internship at SCK CEN (2018-2019), performing T-RANS simulations on the PLAJEST triple-jet configuration. His results have been recently included in my last scientific publication (under review) and, more important, his contribution was essential to boost my research before the end of my doctoral contract. We worked in a very effective and friendly way, having fun after the working hours too. Concluding with TUD, I would also thank two great assistants, Anita and Sandra, who played a fundamental role in setting hospitality, authorizations and accounts, which let me smoothly work from Belgium.

As mentioned, I spent the majority of my contractual period at SCK CEN, under the supervision of Katrien Van Tichelen and Steven Keijers. I appreciated their regular and fair advises, and the possibility to be fully integrated in the team dynamics. It is thanks to them if I could contribute to the SESAME and MYRTE EC projects, where I really developed my interpersonal and presentation skills. We spent several missions together, visiting other research centers and universities in Europe. This gave me the chance to network and get a global view on the latest developments on advanced liquid metal-cooled nuclear technologies. I thank the SCK CEN Academy for having arranged the agreement with TUD. I also thank SCK CEN and ENGIE for having funded my doctoral research. Among my SCK CEN colleagues, I would thank Alessandro, who was a reference for me on CFD topics, thanks to his competences and academic background. I would also thank Fabio for his support in the post-processing phase, and Davide for having shared some of his endless knowledge on thermal-hydraulics with me. They are still friends of mine, together with other colleagues at SCK CEN, like Francesco, Riccardo, Dario, Clarita, Matteo (and more...). The latter have not directly contributed, but rather supported me with loyal friendship, together with their partners and families. At SCK CEN, I found not only research opportunities and organizational challenges, but also a second family for my life in Belgium. Particularly, Francesco and Davide

are like brothers for me.

Finally, I would thank my points of contact at VKI, Philippe, Lilla, Sophia and Agustín, for their collaboration in sharing the MYRTE-experiment results, and willingness to review my CFD analysis. Among them, a special acknowledgment is for Agustín, who helped me in implementing and debugging several libraries in OpenFOAM. I wish him best of success for his new career as professor.

2019-2023

The post-contractual period started on October 1, 2019, when I joined Tractebel Engineering (TE) as design engineer. I had not enough requirements to conclude my doctoral project, particularly lacking scientific publications, also needing to finalize my last simulations on the PLAJEST triple-jet configuration.

This means that I have continued my doctoral research during my spare time, besides my private priorities. I needed to find concentration and motivation during the bad times, like the COVID-19 confinement and, especially, disease and loss of my beloved mom, but also the good times, like moving in a new apartment and organizing my two weddings (legal in Belgium and religious in Italy). I was practically alone, without computational power and connections with my TE role. This doctoral journey seemed endless and impossible at one point, but I discovered an extraordinary perseverance in me. I first succeeded in completing the computational works in 2020. Then, I published as first author almost one paper per year until 2023, when I have finally drafted this dissertation. This is my best individual achievement and, once in my life, I have to say that the most important person to thank is me, for my commitment and consistency.

Only Sasa has continued to regularly support me, and his contribution has been even more important than before. We kept monthly meetings through videocalls and, step-by-step, we reached the defined milestones. I am sure that he had a lot of pressure to justify the slow progress to his hierarchy, but he defended me, always. This consolidated the great opinion that I have on him. Once more, thanks Sasa!

I would again thank Chris, as well as the department management and the whole TUD organization, for having ”waited” for me and trusted on this project.

I finally thank the members of the board, for their participation and review of this thesis.

Dedication

I dedicate this work to my parents, Angelo and Marina, and my wife, Paola.

Angelo has been a great father, an example of hard worker, with strong analytical attitudes. He inspired me for his precision and commitment, which are fundamental in my career. He gave me all the tools to succeed both at work and in life and, even today, I know I can always count on him. He has been always available, no matter what is the challenge he has to face in life.
Grazie Babbo, ti voglio bene.

Marina was my strongest pillar, my deep motivation and the most important person in the first part of my life. As mother, she gave everything to me, at the maximum of her ability, and her love has guided me until this moment. She was so strong. She taught me to always strive for the best, and I am who I am thanks to her. She cannot see me today, but I hope that she would have been proud of me.
Grazie Mamma, sei sempre nel mio cuore.

Paola is my new life. She has not seen the beginning of this journey, but she took this train at the right time. She is my true love, my wife, my best friend, even my colleague at work. She is all for me. I could finalize this doctoral research only thanks to her support and motivation. Paola has been so thoughtful, sacrificing most of her spare time too, just to stay by my side. There are no words to describe how grateful I am. I could never have wished for a better doctoral paranymph.
Grazie Tatina, ti amo.

Vittoria!

Edoardo Cascioli
Turnhout, January 2024